

Development and Characterization of
3D Printable Diffusion Controlled
Drug Formulations With UV-Curable
Photopolymer Resins

by
Mi Steinbach
from Witten

Accepted Dissertation Thesis for
the Partial Fulfilment of the Requirements for a
Doctor of Natural Sciences

Faculty 3: Mathematics/Natural Sciences
University of Koblenz

Reviewer:
Prof. Dr. rer. nat. Björn Wolle
Prof. Dr. rer. nat. Richard Hirsch

Examiner:
Prof. Dr. rer. nat. Björn Wolle
Prof. Dr. rer. nat. Richard Hirsch
Prof. Dr. rer. nat. Wolfgang Imhof

Date of the oral examination: 14.11.2025

Acknowledgements

At first, I would like to thank my supervisors and mentors Prof. Dr. Björn Wolle, Prof. Dr. Richard Hirsch and Prof. Dr. Michael Gartz for supporting and guiding me through my dissertation. I am thankful for the opportunity to conduct research as a visiting scientist at the University of Koblenz and would like to thank Prof. Dr. Silke Rathgeber at the Institute of Integrated Natural Sciences for her supervision. Furthermore, I would like to thank the research groups at the Institute of Integrated Natural Sciences at University Koblenz, the Faculty of Applied Natural Sciences, and the Faculty of Information, Media and Electrical Engineering at TH Köln. Particularly, I would like to thank Anton Kraus, Thomas Knieper, Lothar Müller, Stefan Peters, Sara Kopilas, Prof. Dr. Sherif El Sheikh, Mareike Fröhling, and to the students who assisted me in this research project: Inha Knaub, Jens Rödder, Ahin Sleman, Christian Schax, Nicole Szweda and Leonard Klein. For the funding, I would like to thank the Ministry of Culture and Science of the German State of North Rhine-Westphalia, the TH Köln InnovAGe Research Institute and the Faculty of Information, Media and Electrical Engineering.

Abstract

In recent decades, there has been a growing awareness in our society of the importance of medicines that are personalized to the needs of patients. This dissertation contributes to the research on personalized dosage forms with controlled drug release. The basis of our investigations is the simulation of the expected diffusion properties of these personalized dosage forms using computer-aided statistical methods and the subsequent adaptation of suitable models to experimentally obtained data. This novel approach makes it possible to verify the parameters determined from experimental data, such as the diffusion coefficient. A key finding is that, for instance, the homogeneity of the sample, the precision of the measurement data collection and the consideration of the measurement environment have a greater influence on the validity of the diffusion coefficient than the choice of the diffusion model. The experimental part of this thesis comprises the development and characterization of drug-loaded polymer resins, the implant fabrication, and the pharmaceutical and physical investigation of the polymer-drug implants. The formulation of polymer resins and their suitability for 3D printing (3DP), as well as their use in pharmaceutical applications, are extensively addressed. The release properties and, in particular, the polymer network's mesh size influence on the active ingredient's diffusion rate in aqueous solution are studied. In addition, the production of polymer samples by means of UV photopolymerization in a molding process developed for this purpose, as well as by using stereolithographic 3DP, are examined comparatively.

The polymerization process and the polymer properties resulting from the different production methods are presented. The major findings from these studies include the successful development of a polymer resin formulation whose release and swelling properties are comprehensively demonstrated using a model drug. Furthermore, the optimization of this resin for the use of the active pharmaceutical ingredient (API) testosterone was achieved. A comparison of the two developed resin formulations clearly shows the limitations and the possibilities of transferability of both systems. In addition, the results concerning the release of API from the polymer, as well as the diffusion of the solvent into the polymer and the resulting increase in the volume, provide insight into the changed interfacial diffusion resistance in 3D printed polymers compared to molded polymers. This work thus contributes to the development of personalized drug forms and paves the way for the production of release-controlled polymer resin implants for future follow-up work.

Zusammenfassung

Seit einigen Jahrzehnten gibt es ein immer stärker werdendes Bedürfnis unserer älter werdenden Gesellschaft nach Arzneimitteln, welche individuell an die Bedürfnisse von Patient:innen angepasst sind. Die hier vorliegende Dissertation leistet einen Beitrag hinsichtlich der Entwicklung personalisierter Arzneiformen mit kontrollierter Wirkstofffreisetzung. Grundlage der Untersuchungen ist die Simulation der zu erwartenden Diffusionseigenschaften dieser personalisierten Arzneiformen mit Hilfe computergestützter statistischer Methoden und die anschließende Anpassung geeigneter Modelle an experimentell gewonnene Daten. Dieser neuartige Ansatz ermöglicht die Verifizierung der aus experimentellen Daten ermittelten Parameter, wie dem Diffusionskoeffizienten. Eine wesentliche Erkenntnis ist dabei, dass unter anderem die Homogenität der Probe, die Sorgfalt bei der Erhebung der Messdaten sowie die Berücksichtigung der Messumgebung einen größeren Einfluss auf die Validität des Diffusionskoeffizienten haben als die Wahl des Diffusionsmodells. Der experimentelle Teil dieser Arbeit umfasst die Entwicklung und Charakterisierung von wirkstoffbeladenen Polymerharzen, die Implantatherstellung sowie die pharmazeutische und physikalische Untersuchung der Polymer-Wirkstoff-Implantate. Die Formulierung von Polymerharzen und deren Eignung für den 3D Druck sowie die Verwendung in pharmazeutischen Anwendungen, wird umfassend behandelt. Die Freisetzungseigenschaften und insbesondere der Einfluss der Maschenweite des Polymernetzes auf die Diffusionsgeschwindigkeit des Wirkstoffes in wässriger Lösung werden untersucht. Zudem wird die Herstel-

lung von Polymerproben mittels UV-Photopolymerisation in einem hierfür entwickelten Formgussverfahren sowie mittels stereolithographischem 3D Druck vergleichend gegenübergestellt. Der Prozess der Aushärtung und die durch die unterschiedliche Herstellung resultierenden Polymereigenschaften werden dargestellt. Die wichtigsten Ergebnisse bei diesen Studien sind unter anderem die erfolgreiche Entwicklung einer Polymerharzmischung, deren Freisetzungs- und Quelleigenschaften mittels Modellwirkstoff umfassend dargestellt werden können. Darüberhinaus wurde eine angepasste Version dieses Harzes für die Verwendung des Testosteron-Wirkstoffes erreicht und eine Gegenüberstellung der beiden entwickelten Formulierungen zeigt deutlich die Limitierungen sowie Möglichkeiten der Übertragbarkeit beider Systeme. Zudem geben die Ergebnisse bezüglich der Diffusion von Wirkstoff aus dem Polymer sowie die Diffusion von Lösemittel in das Polymer und die dabei entstehende Volumenzunahme Aufschluss über den veränderten Grenzflächen-Diffusionswiderstand in 3D gedruckten Polymeren im Gegensatz zu gegossenen Polymeren. Diese Arbeit trägt somit zur Entwicklung personalisierter Arzneimittelformen bei und ebnet den Weg für die Herstellung von freisetzungskontrollierten Polymerharzimplantaten für zukünftige Folgearbeiten.

Contents

1	Introduction	1
1.1	Motivation	1
1.2	Research Objective	4
1.3	Outline and Contributions	5
1.3.1	Development of a 3D Printable Polymer Resin	5
1.3.2	Polymer Network Characterization	7
1.3.3	Implants for Controlled Drug Release	9
2	Related Work	13
2.1	Pharmaceutical Polymer Resins	13
2.2	Particle Movement in Stationary Systems	15
2.3	Diffusion Measurement and Polymer Mesh Size Calculation	16
2.4	Additive Manufacturing	18
2.4.1	Stereolithography	18
2.4.2	Limitations of Additive Manufacturing	21
2.4.3	Multi Laser Volume Stereolithography	23
3	Theory Framework	31
3.1	From Fokker-Planck to Fick's Law	31

3.2	Terms and Concepts of Diffusion	34
3.3	Mathematical Description of Diffusion	36
4	Diffusion Simulation	43
4.1	Simulating Special Cases of Diffusion	44
4.2	Regression Analysis of Diffusion Data	49
4.3	Conclusion	52
5	Development of a 3D Printable Polymer Resin	55
5.1	Motivation	56
5.2	Materials and Methods	57
5.2.1	Materials	57
5.2.2	Sample Preparation	58
5.2.3	Microscopy	60
5.2.4	Fourier-Transform Infrared Spectroscopy	60
5.2.5	Drug Release Testing	60
5.3	Mathematical Modeling of Drug Release	61
5.3.1	Empirical Approach	61
5.3.2	Theoretical Approach	62
5.4	Results and Discussion	63
5.4.1	Microscopy	64
5.4.2	Fourier-Transform Infrared Spectroscopy	64
5.4.3	Drug Release	65
5.4.4	Mathematical Data Analysis	67
5.5	Conclusion	69
6	Polymer Network Characterization	73
6.1	Motivation	74
6.2	Materials and Methods	76
6.2.1	Real-Time Polymerization Analysis	77
6.2.2	Water Diffusion During Mass Uptake	79
6.2.3	Average Polymer Mesh Size	83
6.3	Results and Discussion	85
6.3.1	Analyzing the Polymerization Process	85

6.3.2	Mass Uptake During Swelling	90
6.3.3	Diffusion Resistance	93
6.3.4	Polymer Mesh Size	94
6.4	Contextual Discussion	96
6.5	Conclusion	97
7	Implants for Controlled Drug Release	99
7.1	Motivation	100
7.2	Material and Methods	101
7.2.1	Resin Preparation	102
7.2.2	Sample Preparation	103
7.2.3	Polymer Mesh Size Calculation	103
7.2.4	Mass Uptake	104
7.2.5	Drug Release Measurements	104
7.2.6	Diffusion Coefficients	105
7.3	Results and Discussion	107
7.3.1	Polymer Mesh Size	107
7.3.2	Mass Uptake	108
7.3.3	Drug Release	109
7.4	Conclusion	112
8	Discussion and Conclusion	115
8.1	Discussion	115
8.2	Future Work	118
8.3	Conclusion	119
	Bibliography	121

CHAPTER 1

Introduction

This chapter introduces the doctoral thesis, providing the foundational concepts and initial findings related to the covered topics. First, the research topic is motivated (cf. Section 1.1) and the objectives of the thesis (cf. Section 1.2) are explained. Following this, there is a detailed outline (cf. Section 1.3) of the contributions to the thesis (cf. Subsections 1.3.1, 1.3.2 and 1.3.3).

1.1 Motivation

This dissertation project combines two research areas: pharmaceutical technology and material physics. The interdisciplinary approach leads to a multifaceted view on a challenge that has increasingly moved researchers for several decades: the development of personalized dosage forms with controlled drug release. In the following, the motivation is outlined from two perspectives – at first, from a pharmaceutical perspective, and afterward, from a perspective of material physics.

Nowadays, the pharmaceutical industry is facing major challenges with particular regard to an increasingly aging society [1]. When produced in large quantities, drugs are developed for the average patient. However, in the treatment of an elderly person

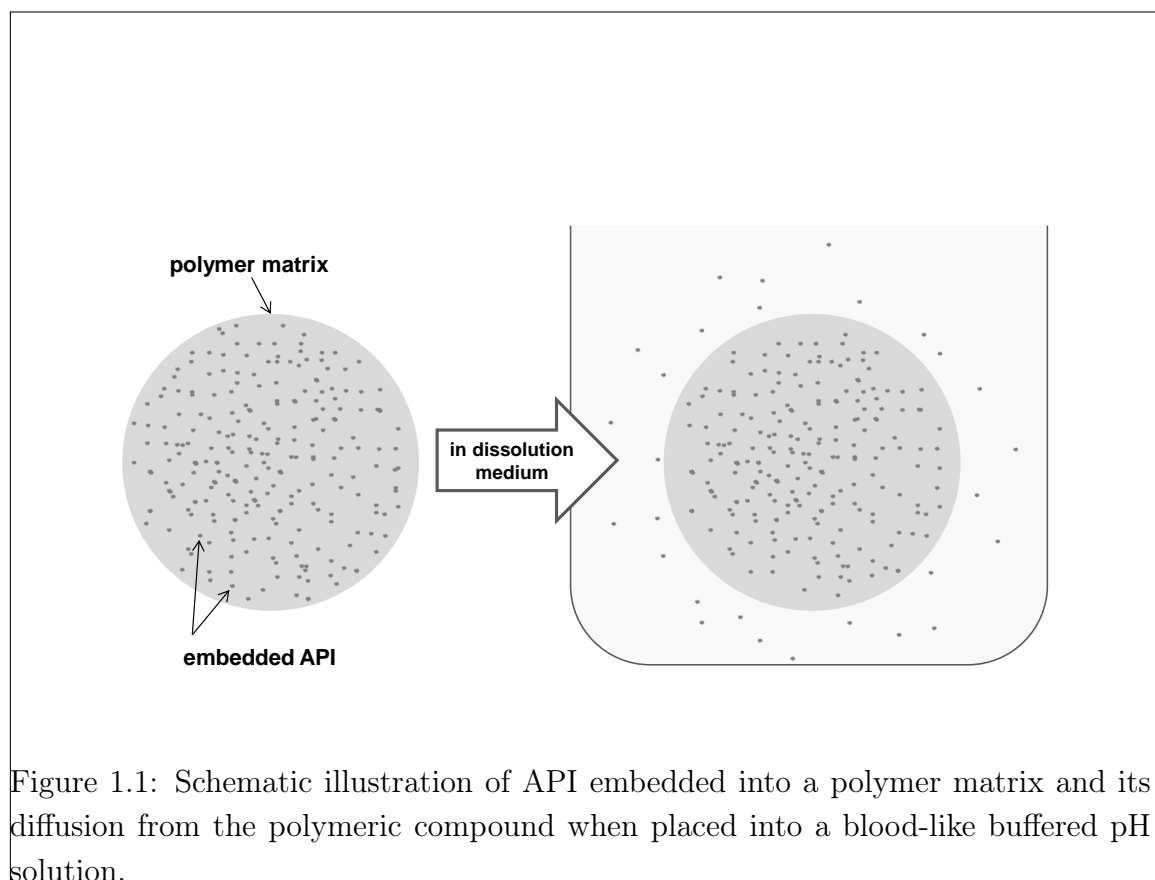
whose pharmacokinetics ¹ have moved away from the average over the years, this may lead to an overdose or strong side effects. This also applies to children or severely diseased people who require higher precautions regarding the dosage of a drug. Moreover, especially elderly patients often take a variety of medications, and the interactions between individual active pharmaceutical ingredients (APIs) can lead to serious adverse effects.

For this reason, a lot of effort has been put into the development of personalized dosage forms over the past decades [2]. In all cases, the precondition is a detailed prior examination of the patient's needs to find an optimal therapy. The term *personalized medicine* encompasses a wide range of approaches for individual treatments [3], from individual dosing of tablets by splitting, prescribing of an alternative API or the same API in an alternative dosage form, up to the fabrication of individualized dosage forms with adjusted dose or release properties. However, incorrect intake due to missing or poor patient training could easily lead to under- or overdosage. In this regard, so-called patient compliance plays a major role. Taking the medication should be as uncomplicated and unambiguous as possible. For instance, it is highly important for the treatment of elderly or mentally disordered patients.

Alternatives to the oral application are usually easier to customize: intravenous application by syringe or infusion can be adapted precisely to the patient's needs. However, this requires support and administration by medical professionals and, in many cases, inpatient treatment. Therefore, it is necessary to provide long-term, individualized care for people in the high-risk group. A completely different and less costly approach is realized with the help of implants for subcutaneous application. The contributions of this work can be categorized into this field of research. A major advantage is that a forgotten dose or an accidental overdosage is no longer possible. Furthermore, side effects due to the rapid increase of the drug concentration in the patient's bloodstream, which is unavoidable with the oral application, are irrelevant [4].

Polymers are versatile, combinable, and modifiable materials whose benefits have already found their way into all areas of material engineering. The times in which only a few very short-lived rubber types existed are long gone. Instead, industries have access to an increasingly growing number of different monomers and polymers.

¹Pharmacokinetics describe the way how a patients body interacts with a taken drug substance.



New or optimized plastics created by better synthesis processes or by new combinations of chemical components with ever-increasing quality lead to a great variety of usability. Depending on the intended application, the physical properties, such as hardness, elasticity, fracture strength, etc., are varied. In materials research, there is a growing interest in materials for medical or pharmaceutical use. After clinical investigations ensuring that there is mutual compatibility between the polymers used and the biological tissues, cells, and body fluids, those materials can be used in medical treatment [5]. At the forefront of these potentials, the description and modification of polymer structures down to the molecular level are reaching ever-new dimensions. Through the combination of different monomers, their properties also combine, which leads to a very application-specific material. For instance, the properties of contact lenses can be adjusted in terms of hardness and air permeability through the use of

different monomers like methacrylates, hydrogels, or silicones [6]. By influencing the amount and size of pores in a polymer, not only the degree of permeability but also the specific permeability of certain substances can be achieved. Figure 1.1 illustrates the release of an active ingredient to a medium from a solid polymer in which it is homogeneously distributed. However, the properties of the final product are only partly dependent on the material composition. Equally decisive is the production process, in which a more or less cross-linked network is created during the polymerization process. The development of drug-containing implants, as investigated in this work, benefits more than any other topic from the interdisciplinary consideration by the research fields of pharmaceutical technology and material physics. However, the control of drug release over a long period of time is a major challenge for the development of drug-loaded implants. The implant's material must be designed to continuously release the embedded API into the patient's tissue or bloodstream, as depicted in Figure 1.1. The analysis of collected data is of great importance in an experimental investigation. Since Crank's detailed description [7], the mathematical representation of diffusion processes has been developed continuously. Today, in the age of fast computers, experimental data are fitted using statistical methods to describe them quantitatively. More fundamental to any experimental study, however, is the validation of the results obtained and the assessment of possible sources of error. This can be achieved by a prior simulation, as this work shows.

1.2 Research Objective

The aim of this dissertation is to develop 3D printed polymer dosage forms with controlled drug release. In order to achieve this, a major step is to develop and study a polymer resin made from pharmaceutically usable materials. Subsequently, the polymer implants produced from this resins will be investigated. Decisive for the successful development of the dosage forms are their diffusion properties. Consequently, the theoretical part of this thesis will focus comprehensively on the theory and analysis of diffusion in polymers. In addition, criteria are to be defined for a photopolymer resin to enable the production of polymer dosage forms using 3D printing (3DP) on the one hand, and lead to stable polymer objects that will release the API within the human body, on the other hand.

1.3 Outline and Contributions

The following section motivates and outlines the research contributions of this dissertation.

In earlier work, the principle of an optimized Stereolithographic 3DP Method called Multi Laser Volume Stereolithography (MLVS) was introduced [8]. As part of Chapter 2 it is recaptured as it motivates the research questions underlying this thesis.

Chapter 3 then provides the theoretical basis for the experimental question of diffusion control of drug-loaded polymer implants.

A basis for the interpretation of the measurement data and related findings is provided in Chapter 4, where simulations are used to give a fundamental understanding of the diffusion properties.

The development of a resin formulation for use as a pharmaceutical implant is the first objective and is described in Chapter 5. In order to characterize the resin formulation, variants with different compositions are compared and a model API is integrated for release studies. A procedure for the production of homogenous samples with high reproducibility is being developed.

Further consideration is given to the production of 3DP samples in Chapter 6. Pending questions on how the laser intensity or irradiation time influences the curing process of the resin are covered. In this regard, an in-depth analysis of the polymerization process is provided. In addition, it is analyzed how the layer-wise printed objects compare to the homogeneous (non-layer) objects.

In both Chapters 5 and 6, a dye is used as a model drug to facilitate the experiments. However, the question remains whether and how it is possible to incorporate a genuine drug. In this regard, Chapter 7 presents a revised resin formulation with a genuine API. Finally, Chapter 8 discusses the results, puts them into context, and provides an outlook for future work.

1.3.1 Development of a 3D Printable Polymer Resin

The resin of the feasibility study made for the MLVS testing, described in Section 2.4.3, is toxic to the human organism, which is an obstacle to pharmaceutical applications. To this end, a suitable alternative non-toxic resin formulation should be based on pharmaceutically approved substances, including monomers, polymers,

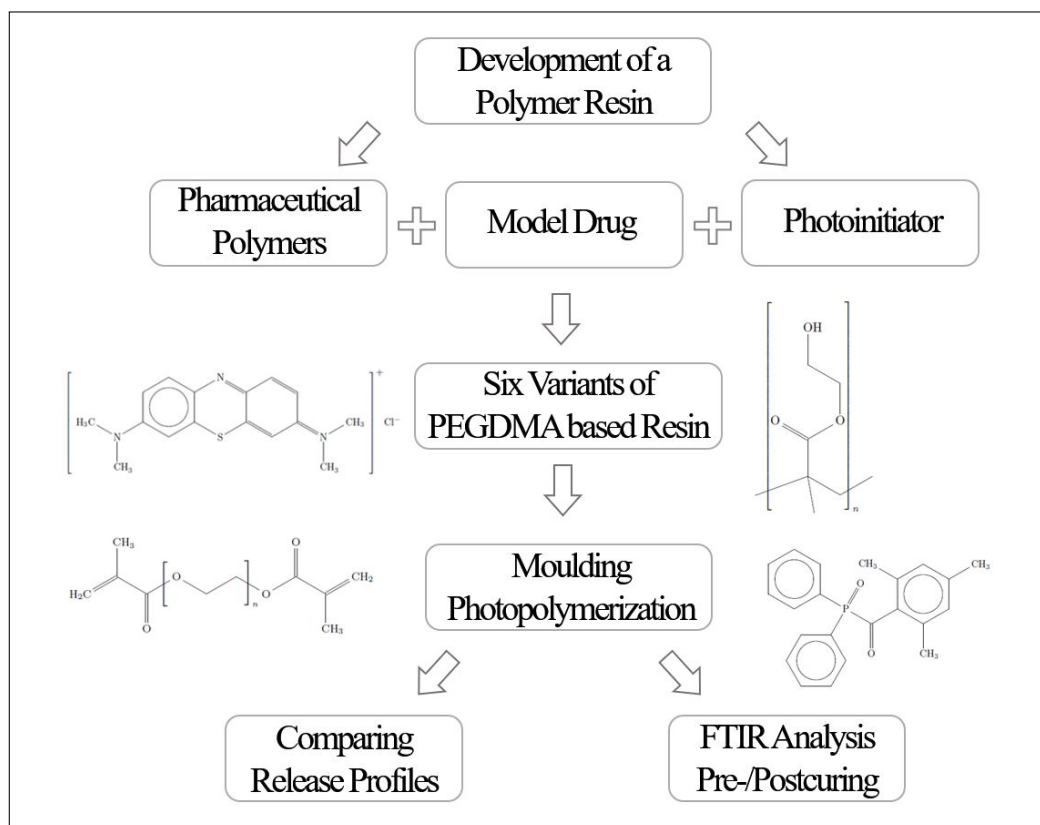


Figure 1.2: Overview of the 3D printable photopolymer resin development.

APIs, solvents, etc. After polymerization, unreacted monomers could lead to undesirable reactions in the body and thus have a cytotoxic effect. For this reason, the polymerized material has to be analyzed for remaining reactants, i.e., unreacted monomers. Furthermore, it needs to be assessed if it is possible to incorporate an API into the polymer matrix that can be enclosed during polymerization. Finally, it is highly desirable to control the API's release profile with the help of the material composition.

As depicted in Figure 1.2 Chapter 5 proposes a non-toxic resin avoiding monomers by the use of cross-linking polymers. These polymer chains, which are reactive at both ends, lead to net-like structures (matrices) when polymerized and reduce the number of reactants. In total, six variants of resins are presented, differing by the amount of solvent or hydrogel Poly(2-hydroxyethyl methacrylate) (pHEMA).

The fundamental component of each resin is the cross-linker Poly(ethylene glycol) dimethacrylate (PEGDMA) with either a short or long chain length. The photopolymerization of the resin is enabled by adding Diphenyl (2,4,6- trimethylbenzoyl) phosphine oxide (TPO), which is a suitable UV-sensitive photoinitiator (PI).

For the analysis, each resin variant is poured into a mold and polymerized under ultraviolet (UV) light exposure. In order to verify that no reactive groups remain after polymerization, fourier-transform infrared (FTIR) measurements of the resin before and after polymerization are compared. To simplify the release analysis, a dye (methylene blue (MB)) is used as a model drug and substitutes the API. The dye is dissolved in the resin and embedded during polymerization. Afterward, release experiments in a blood-like buffer solution (pH medium corresponding to arterial blood) are performed to see how much and how fast the dye is released from each of the six different resin formulations.

Overall, it is possible to develop a non-toxic and monomer-free resin formulation as an alternative to conventional 3DP resins. All of the six resin variants developed are stable and can be polymerized by UV light exposure. Moreover, the six resin variants lead to different release profiles, which empirically confirms that the material composition can be used to control the API release. In particular, the polymer chain length has a more substantial influence on the release rate than the hydrogel. Finally, the release profiles are analyzed via a mathematical model in order to compare the differences in more detail.

The influence of the cross-linker chain length and the pHEMA content on the release profiles is shown and paves the way to personalized PEGDMA resin mixtures. Based on these outcomes, it can be analyzed in the next step if it is possible to replace the model drug with a reasonable API.

1.3.2 Polymer Network Characterization

While the previous Chapter 5 analyses the pharmaceutical applicability, Chapter 6 focuses on the 3DP process, as outlined in Figure 1.3. How the layers of 3D printed objects influence the release properties is widely unknown. However, if they were known, then they could be considered besides the material composition as parameters for controlling the release profile. More precisely, in Chapter 6 it is clarified how

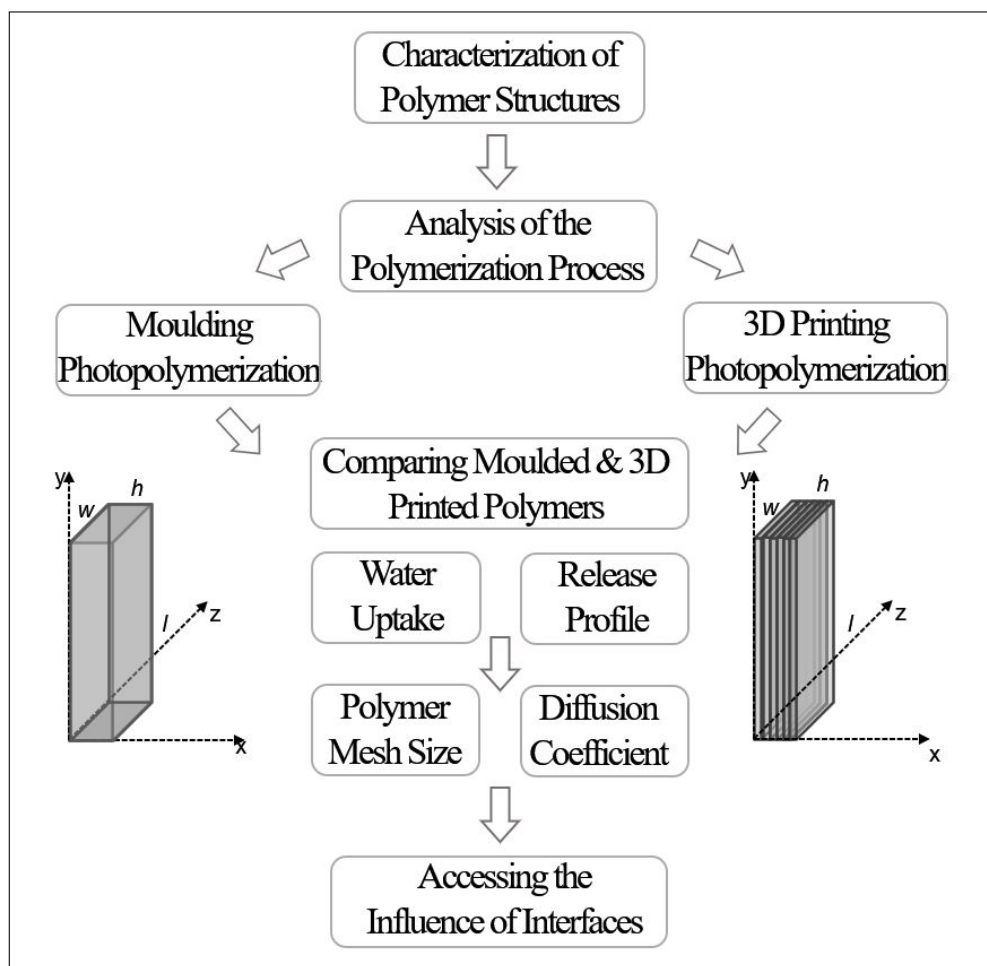


Figure 1.3: Overview of the main steps in the polymer network characterization.

homogeneous bulk material properties compare to the properties of layered structures.

Chapter 6 discusses the differences in the polymer network properties resulting from 3D printing or molding. By expanding the results of Chapter 5, the photopolymer resins are analyzed concerning the photopolymerization process, the temporal mass uptake, the diffusion coefficient of water, and the polymer mesh size. For each of the six resin variants introduced in Chapter 5, the optimal laser intensity and irradiation time for curing are determined. The corresponding analysis is based on rheological measurements of the resin's viscosity. During UV irradiation, the change in viscosity

describes the temporal progression of solidification, and thus, the influence of the irradiation intensity and the exposure time on this solidification progress can be determined.

3D printed samples are compared to molded samples of equal shape and size to better understand how layer-wise printed objects compare to homogeneous materials. Both sample types are compared by the diffusion resistance and polymer swelling over time. The measured data are approximated by a modified fitting function that takes the geometry into account in order to quantify the differences between layer-wise printed and molded resins. Based on the molecular weight between cross-links, the average mesh size can be determined with the help of the maximum mass uptake.

The experimental results show that the layers in printed objects have a measurable influence on the release profile. The corresponding release properties cannot be controlled independently of the printed object's resolution, namely the number of layers and the layer thickness. Based on the experiments, lower and upper bounds of the laser intensity can be determined. Likewise, it is possible to identify an ideal intensity range for curing the resin. When comparing the layer-wise printed resin to the molded resin, there are apparent differences between the polymer swelling and the diffusion resistance. The drug release is decelerated by the layers. Likewise, the layers impact on and decelerate the polymer swelling, especially that of polymers with short lengths. In addition, the average mesh size is reduced by the layers. The mathematical analysis brings quantifiable inside into the amount of reduction that occurs from the interfaces within a layer-wise printed object.

Finally, there is still the open question if the model drug can be replaced by another API, which is analyzed in the further experiments.

1.3.3 Implants for Controlled Drug Release

In addition to the model drug MB used previously, it is most sensible to introduce another active ingredient in order to investigate the general applicability of the presented resin formulation for pharmaceutical applications. Most active ingredients are not well soluble in water in contrast to the previously used model drug. Resins used in the previous studies, therefore, contain a considerable amount of water. In Chapter 7, the focus is the API exchange in 3D printable polymer resins, as depicted in Figure 1.4. It is analyzed if it is feasible to integrate different APIs into a basic resin

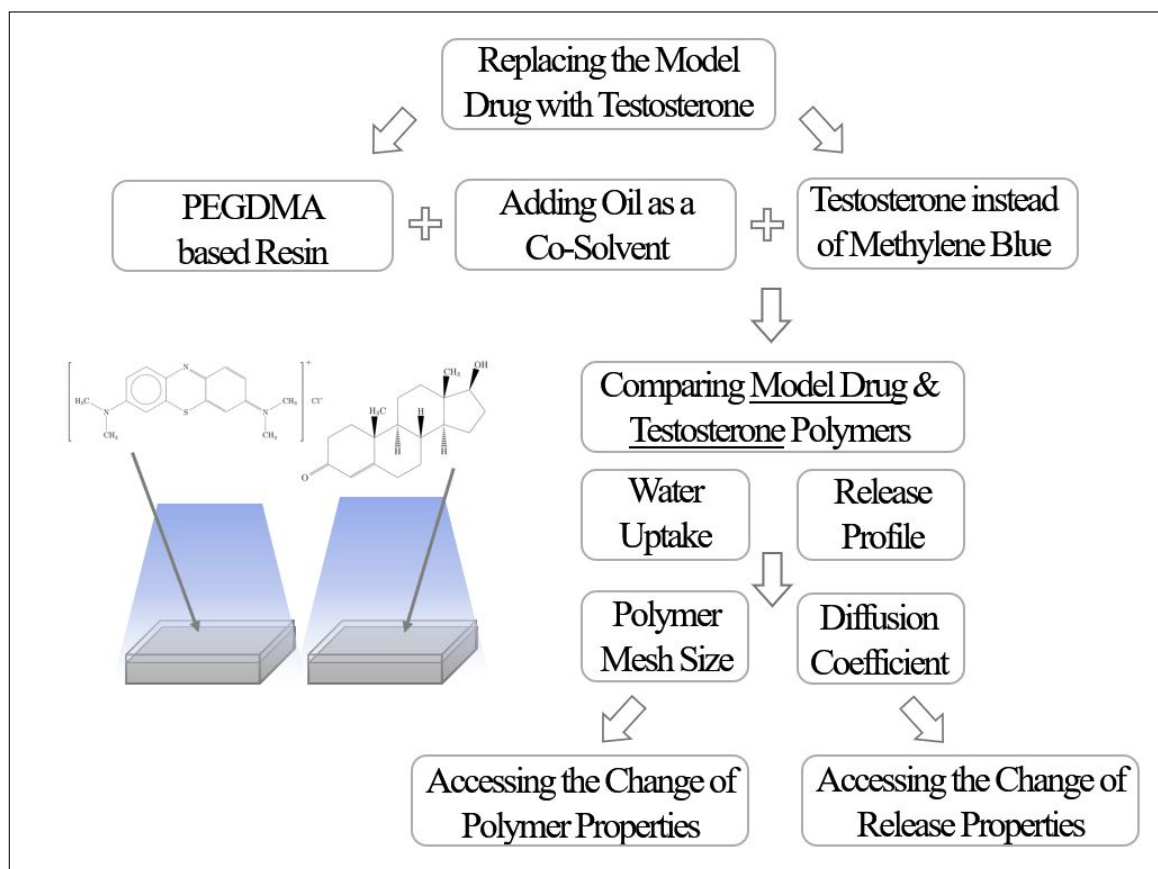


Figure 1.4: Overview of the formulation and characterization of a testosterone containing polymer resin.

formulation and to predict the release behavior from the resulting polymer samples. Therefore, the previously discussed resin formulation is adjusted for replacing the model drug (MB) with testosterone (TE).

As it is more reasonable to use a printed implant for long-term therapy, testosterone offers an interesting use-case study. For instance, testosterone implants could be used to balance the testosterone levels of patients suffering from hypogonadism. Currently, testosterone implants are not yet approved in Germany as there are many concerns regarding existing solutions in this area, but there is generally a high demand for such an application.

In order to replace methylene blue with testosterone, the original solvent water is

replaced by an emulsion of water and castor oil, using an emulgator. The overall goal is to develop a stable and 3D printable resin formulation with the highest possible amount of testosterone. By using polarization microscopy, it is verified if the solution is stable and the testosterone does not crystallize any further. Both the TE-based resin and the MB-based resin are UV-polymerized in a mold and characterized to identify differences in the release and swelling properties. Consequently, the diffusion coefficients of the API during drug release, as well as the diffusion coefficients of water during mass uptake, are studied. As testosterone cannot be analyzed in the visible spectrum, the release profile has to be identified with the help of high-performance liquid chromatography (HPLC). Similar to the method in Chapter 6, the molecular weight between cross-links is used to determine the average mesh size with the help of the maximum mass uptake.

The experimental results show that the solution is stable, and the testosterone can be successfully integrated into the polymer network during polymerization. Even more, the testosterone is almost fully released from the polymer when it is placed into a blood-like buffered pH solution. The mesh size of both resins is identical, whereas the mass uptake of the TE-based resin is faster. Likewise, the release rate of TE is higher, which can be explained by the smaller molecule size of TE. In conclusion, the molecule size is identified to have a major influence on the drug release in the case of low swelling polymer systems with equal mesh size. As the mesh size of both systems in our study is identical, the relevance of the molecule size on the prediction of release profile when the API is exchanged has to be highlighted. The chapter leaves a further analysis of toxicity for future work. Similarly, a use-case study that brings together the TE-based resin with the principle of MLVS should be conducted.

CHAPTER 2

Related Work

The following chapter contains the literature on the scientific background to this work and the experiments based on it. First, Section 2.1 presents the materials for the production of pharmaceutical resins. Subsequently, Section 2.2 describes basic concepts on the movement of particles, followed by the basics of diffusion measurement and mesh size determination in Section 2.3. In the last Section 2.4, the principles of additive manufacturing and in particular stereolithography (SLA) are outlined, limitations are described and an optimized SLA process proposed in preliminary work is explained.

2.1 Pharmaceutical Polymer Resins

Over the past decade, SLA technology has been increasingly used in the field of biomedical and pharmaceutical research. For human application, special attention is paid to the materials used. Since photopolymer resins for prototyping are optimized for speed of production and mechanical stability, new resin compositions are currently being considered for low toxicity or drug compatibility.

Foremost is the selection or synthesis of the polymers, which could be widely clas-

sified into natural and synthetic polymers. Natural polymers provide good biocompatibility and degradability. For example, hydrogels based on proteins like gelatin or collagen are used for tissue engineering as they provide an adequate environment for living cells [9]. Polysaccharides represent the other major group for the synthesis of natural polymers. Among them, chitosan is of particular interest since it is frequently used in both biomedical and pharmaceutical research [10–13] It has already been demonstrated that chitosan derivatives are suitable for 3DP as described by Bardakova et al. [14] who implanted SLA printed allylchitosan implants to mice. Natural polymers also promise advantages in terms of 3D printed solid dosage forms. The structure of the polymerized hydrogel network can influence on the gelation properties, porosity, permeability and mechanical properties. A huge impact here relates to the proportion of water in the resin mixture prior to polymerization as it influences the resin viscosity [9,15]. The negative aspects of natural polymers include poor mechanical strength and poor shape stability.

On the other hand, synthetic polymers are generally poorly degradable and less biocompatible ¹ than natural polymers but provide high mechanical strength and are very versatile [9]. The best known representatives are poly (ethylene glycol) (PEG), poly (vinyl alcohol) (PVA), poly(methyl acrylate) (PMA), or polyurethane (PU). In fact, combinations of those are far more common, like poly(ethylene glycol) diacrylate (PEGDA) or poly (ethylene glycol) dimethacrylate (PEGDMA), urethane dimethacrylate (UDMA), triethylene glycol dimethacrylate (TEGDMA), poly (ethylene glycol) methyl ether thiol (PEG-Thiol), Poly-(2-hydroxyethyl-methacrylate) (PHEMA) or bisphenol A-glycidyl methacrylate (Bis-GMA) [16–24]. These oligomers show improved chemical and mechanical properties resulting from the combination of the monomer characteristics. Moreover, the resulting network modifies by these monomer properties and the degree of functionalization ². A single-linked polymer chain can be substituted with reactive groups at one side or at each side to serve as a cross-linker. However, multiple or hetero functionalization is also possible. Typically, resins consist of a combination of monomers and cross-linking oligomers to achieve a stable polymer network. Since reactive groups remaining in the finished product

¹Biocompatibility describes the ability to be in contact with a living system without producing an adverse effect

²Functionalization means the number of reactive groups

could possibly lead to undesirable reactions in the human body, it is crucial to maximize the conversion rate during polymerization. In terms of stereolithography (SLA) 3D printing (3DP), the choice of a photoinitiator (PI) plays an important role, apart from the choice of the monomers or oligomers. Depending on the wavelength of the printer's light source, an initiator with suitable spectral sensitivity is used. Since most SLA apparatuses operate in the ultraviolet (UV) spectrum, photoinitiators with absorption peaks in the UV-A and UV-B range, around 250 nm to 400 nm, are commercially available [16]. Examples are Bis (2,4,6-trimethylbenzoyl) phenylphosphine oxide (BAPO), Diphenyl (2,4,6-trimethylbenzoyl) phosphine oxide (TPO), 2-hydroxy-4-(2-hydroxyethoxy)-2-methylpropiophenone (Irgacure 2959), 2-hydroxy-2-methyl-1-phenyl-propan-1-one (Irgacure 1173) or 2,2-Dimethoxy-2-phenylacetophenone (DMPA). Nevertheless, cytotoxicity is a significant concern regarding highly efficient PIs [25–27]. Alternatives with low or no cytotoxicity, like riboflavin, are also investigated [28–31].

A clear advantage of SLA for the production of dosage forms is a high printing resolution along with a high dimensional accuracy when compared to other 3DP technologies [32, 33]. Multiphoton Polymerization (MPP) has an even higher resolution up to less than 100 nm. However, the fabrication time is rather long [19, 29]. Since SLA 3DP is devoid of heat and mechanical forces, it has a low potential for damaging the drug substances during production, excluding those that are sensitive to UV light. The high reactivity of monomers, oligomers, and photoinitiators in the resin formulation involves a potential risk for the chemical stability of pharmaceutical products and, hence, the human body. Therefore it is crucial to ensure the absence of unbounded monomers and photoinitiators in the dosage form [25, 34]. Nevertheless, current research indicates a major step towards the production of personalized dosage forms using SLA 3D printers.

2.2 Particle Movement in Stationary Systems

Anomalous diffusion, marked by a nonlinear scaling of mean square displacement over time, can arise from various stochastic processes. These processes include the continuous-time random walk, fractional Brownian motion, and Lévy flights and walks, each capturing different aspects of the anomalous transport phenomena ob-

served in complex systems [35]. Understanding these processes is crucial for explaining diffusion in systems where classical models, such as normal Brownian motion, do not adequately describe the observed dynamics.

The Continuous-Time Random Walk is one of the fundamental models for anomalous diffusion in which the particle does not move continuously but jumps at random intervals [36]. It is a stochastic jump process in which the particles undergo a series of jumps with random delays between each jump. These delay times are usually drawn from an arbitrary probability distribution, which can range from exponential to power law distributions.

The fractional Brownian motion (fBm) extends the classical Brownian motion by a Hurst exponent, which controls the correlation in the motion [37]. If the exponent is 0.5, fBm becomes a standard Brownian motion with independent increments and normal diffusion. For exponents above 0.5, the process exhibits persistent correlations over long distances, while for values below 0.5 it exhibits antipersistent correlations over short distances. This leads to a range of diffusive behaviors, from subdiffusion to superdiffusion³.

Lévy flights and Lévy walks are stochastic processes characterized by step lengths that follow a strongly fluctuating probability distribution [38, 39]. In contrast to conventional random walks, where the step sizes are usually finite, Lévy walks involve steps of potentially infinite length, resulting in “flights” over long distances interspersed with short steps. This behavior leads to anomalous diffusion, where the mean-square displacement grows faster than in normal random walks. In a Lévy flight, the direction of each step is independent of the previous one. In contrast, in a Lévy walk, the direction can also depend on time, resulting in a combination of long-distance jumps and periodic direction changes.

2.3 Diffusion Measurement and Polymer Mesh Size Calculation

Diffusion is the fundamental process that describes particles’ movement from high to low-concentration regions. The most common framework for diffusion is based on

³This means an anomalous, decelerated or accelerated diffusion.

Fick's laws, which describe the relationship between the concentration gradient and the diffusion flux. The diffusion coefficient is a key parameter that quantifies the rate of dispersion of particles in a medium. It depends on factors such as the medium's temperature, particle size, and viscosity.

During the polymerization of individual polymers or polymer chains, cross-links are formed between the chains, creating a network similar to a net. In this three-dimensional network, free spaces are formed, which are bounded by the chains and their linking points. These free spaces can be described as meshes.

The theory of free volume plays an important role in polymer research [40]. The theory divides the polymer volume into a bulk volume, which is occupied by the polymer chains, and a free volume in the form of voids (the meshes), which is not occupied by the polymer chains. The water diffusion process depends on the free volume around the diffusion molecule, and diffusion can only occur when the local free volume reaches or exceeds the critical value that allows the movement of the water molecule. The same applies, obviously, to the diffusion of drug molecules that diffuse through or out of the polymer network.

This idea leads to the determination of two important parameters for this study. The diffusion coefficient, which derives from the measurement of the diffusion profile, and the mesh size, which derives from the change in polymer volume during swelling.

The theory of estimating the diffusion coefficient from the experimental data is covered in detail in Chapter 3. The determination of the mesh size is considered in more detail below, whereby this considerations are concentrated on the equilibrium swelling theory. This theory will be applied in the experimental part of the thesis.

The relationship between the mesh size of polymer networks and their degree of swelling at equilibrium is central to understanding the physical properties and applications of polymer-based materials, in particular hydrogels. Mesh size refers to the average distance between cross-links within a polymer network. This size determines the free volume available for solvent molecules. Equilibrium swelling describes the point at which the polymer network has absorbed as much solvent as possible without further structural changes. At this stage, the swelling is balanced by the elastic retraction forces of the polymer chains and the osmotic pressure that causes the solvent to be absorbed. The mesh size influences the degree of swelling. Larger mesh sizes allow more solvent molecules to penetrate, which increases the swelling

capacity, while smaller mesh sizes limit solvent absorption. This relationship is quantitatively described by theories such as the Flory-Rehner equation, which integrates the interactions between polymer and solvent and the elasticity of the network to predict swelling behavior. Factors such as cross-link density, interaction between polymer and solvent, and conditions like temperature and pH play a crucial role. A lower cross-linking density leads to larger mesh sizes and enables higher degrees of swelling. Conversely, highly cross-linked networks have smaller mesh sizes, which leads to lower swelling. This experimental setup and the analysis of the swelling data are described in detail in 6.

2.4 Additive Manufacturing

In the following details about the 3DP technology SLA including the principle of photopolymerization (cf. Section 2.4.1), the limitations of conventional approaches of additive manufacturing (cf. Section 2.4.2), and details about the fabrication principle that was introduced as Multi Laser Volume Stereolithography (MLVS) by the author of this thesis [41] (cf. Section 2.4.3) are given.

The author declares that the following Sections 2.4.1, 2.4.2, and 2.4.3 include verbatim quotes from [41].

2.4.1 Stereolithography

In 1980, a new apparatus for three-dimensional (3D) fabrication with UV curable polymers was described by Hideo Kodama [42]. Later on, in 1998, Charles W. Hull patented the first stereolithographic 3D printer [43]. Acrylate-based resins consisting of monomers or oligomers and a photosensitive initiator were polymerized by irradiation with UV light. The apparatus allowed layer-wise polymerization of sequential layers up to the final three-dimensional object. One layer could be hardened at once by just covering irrelevant parts of the resin with a variable mask or by an x-y-controlled focused light spot that moves across the surface of the resin. This principle still forms the basis for today's stereolithography (SLA) 3D printers.

Over the past 20 years, more and more printing systems have been developed along these lines. Among them are the Laser Induced Bottom-Up SLA process (LSLA),

Digital Light Processing (DLP), Multiphoton Polymerization (MPP), or Continuous Liquid Interface Production (CLIP). These liquid-to-solid 3D printing techniques are also referred to as vat-polymerization [25,44,45]. LSLA is closest to the original SLA technique described by Hull and is discussed in more detail later on. DLP is based on the principle of full-layer curing. A binary image is projected onto the resin surface with the help of a digital micromirror device [44]. The projection of an entire layer makes DLP a very fast printing technique. However, the pixel size of the digital mirror mainly limits the lateral resolution of DLP objects. By contrast, MPP operates on a very different scale, namely on the nanometer scale [19]. As the name suggests, the process is based on polymerization by the fusion of multiple photons. The fusion of two or more photons to one high-energy photon is achieved by non-linear optical processes provoked by high light intensities [46]. The laser is focused sharply to achieve high radiant flux at a certain depth within the resin vat, which can be achieved by a microscopic lens. The most common MPP process is the two-photon polymerization (2PP) [29,44].

An approach that takes advantage of an apparent weakness of the resin is CLIP [47]. It uses the fact that radical photopolymerization is inhibited by oxygen. From below the resin tank, light patterns are projected through a light and oxygen-permeable window. A small layer of oxygen above the window (dead zone) prevents the resin in this zone from polymerizing. This enables good controllability of the curing process and accelerates the printing process. Besides these four most common techniques, numerous variants of SLA 3D printer systems are developed for specific applications. Examples are the development of apparatuses for the production of optical components, such as lenses [48,49].

The most common SLA 3D printers use the laser induced bottom-up SLA technique. Photopolymerization is the basis for the 3DP process and is induced by a laser light source in the UV spectrum which is focused at the surface of a photosensitive polymer resin [50]. In the focal area of the laser, polymerization is started by a photosensitive radical initiator. Sequentially, reactive monomers and oligomers combine into a chain or branch to eventually build a stable network.

The main component in common laser stereolithography (LSLA) setups is a short wavelength laser irradiating perpendicular to the surface of a resin reservoir. The laser beam traces the surface in the lateral direction to cure each layer of the 3D

object. The 3D object is digitally generated in a computer-aided design (CAD) file beforehand. Then, a digital code for each layer is generated from the CAD and is transferred to the 3D printer. In addition to the contours of each layer, information on the layer thickness and the width of the laser track are included in the digital code. The track width restricts the lateral resolution of the final 3D object, whereas the vertical resolution is defined by the layer thickness.

A metal grid serving as a ground plate of the object is placed under the resin's surface, such that the grid is wetted by the resin. Tracing the contour of the first layer with the focused laser beam, the object is fixed to the ground plate. Moving the ground plate downwards causes the just cured layer to be moistened by resin. These steps are repeated until all layers of the 3D object are finished. Craning structures⁴ are in need of additional supporting pillars. These supporting structures have to be integrated into the CAD design and are made of the same material as the object. They must be removed from the finished object in the second production stage. A post-curing process of the resin is recommended to reach full mechanical strength. Limiting factors for the lateral and vertical resolution are the minimal size of the laser focus spot and the penetration depth of the laser beam, respectively. Bottom-up technology means that the laser beam reaches the resin through a transparent window on the bottom of the vat. At the beginning of the printing process, a metal plate, which serves as the base plate for the resulting object, is lowered into the resin from above until it is positioned within a few micrometers (depending on the layer thickness) over the bottom window. Accordingly, the first layer is cured onto the base plate. After completion of the first layer, the plate is lifted so that liquid resin can flow beneath the cured layer, and the second layer is formed. These steps are repeated until the 3D object has emerged and is hanging upside down above the resin vat.

Polymerization

Commonly, photopolymer resins are acrylate-based and consist of tough, low-cross-linked monomers compounded with photo-initiators. The laser generates the critical energy at the resin's surface to start polymerization [51, 52]. At the beginning of

⁴Craning structures are parts of the object, that protrude sideways.

polymerization, the initiators decompose into their radicals with a single electron in its outer shell. In the growth reaction phase, the highly responsive radicals react with carbon atoms bounded in monomers. This reaction leaves another single electron in the outer shell of the monomer and leads to a further reaction. The reaction terminates if no reactive particles are in the range of the radicals, either due to the lack of further bonding abilities or due to the fusion of two polymer chains.

Furthermore, the increase in the resin's temperature terminates chain building when exceeding a specific limit. The ceiling temperature [53] is defined to be the temperature where polymerization and depolymerization (decomposing polymer chains back into monomers) are in counterbalance. Each specific initiator is sensitive to photons of a specific wavelength and ionizes by irradiation with an adequate light source. The resulting radicals are responsible for chain building guaranteeing the curing of restricted areas in order to create structures at the surface of the resin. The resolution of 3D objects created by LSLA is dependent on the diameter of the focal point. Focusing the critical surface energy at a small area increases the resolution.

As 3DP has spread into many industrial sectors, the use of additive manufacturing for the production of personalized pharmaceutical products is increasingly investigated in pharmaceutical technologies. Stereolithography (SLA) offers great advantages when processing pharmaceutical polymers due to its heat- and contact-free process. However, there are still challenges to overcome in terms of toxicity and stability on the way to the customized medication from polymer resin.

2.4.2 Limitations of Additive Manufacturing

Additive Manufacturing, often called 3DP, is one of the most successful inventions in the field of rapid fabrication and prototyping. Originating from the incentive of hobbyists and tinkerers in the 1980s [53], 3DP is established nowadays in commercial production. The opportunity to generate customized objects in a fraction of common manufacturing times attracts nearly every industry segment. The most common application is the production of prototypes, but increasingly customized ready-for-sale products are being produced [50]. Including dental implants, human skin, and oral drugs, to name a few [54–57]. Generally, 3DP is based on additive manufacturing methods whose basic principle is to assemble layers with equal thickness [50]. The contouring of each layer is given by a two-dimensional plane. These planes are created

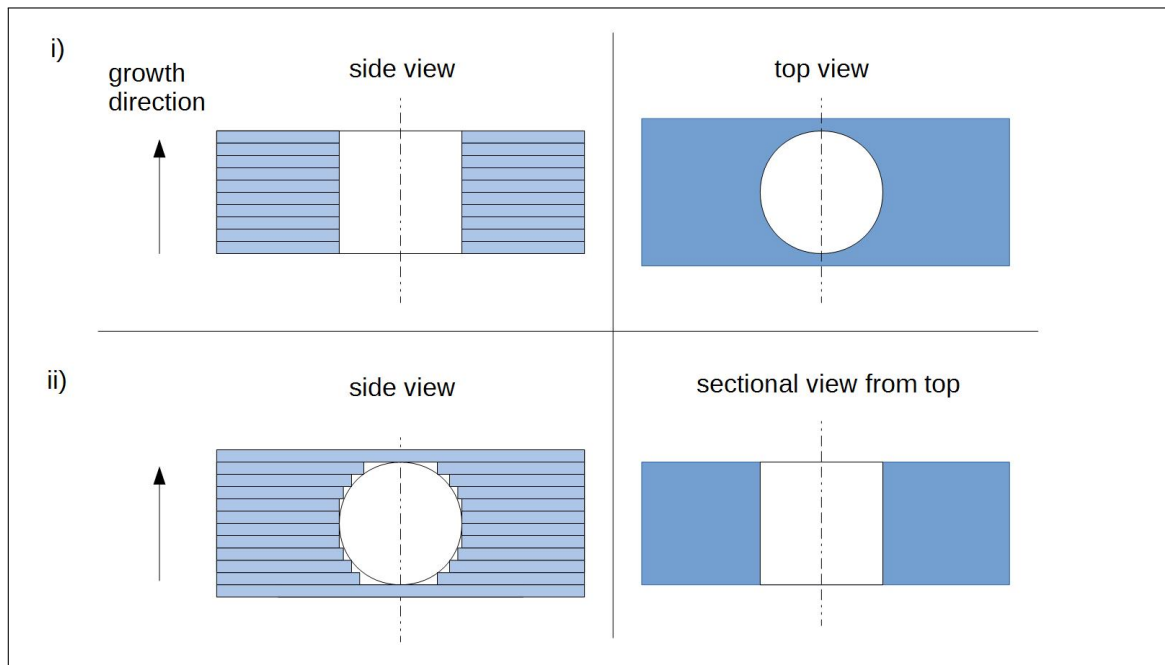


Figure 2.1: Schematic drawing of a hole i) in growth direction; ii) perpendicular to growth direction to illustrate the staircase effect. The effect is explained more in detail in [50]. Figure reproduced from [41].

by slicing the 3D geometry model, which provides the object's data. Then, layers will be stacked and bonded together, which finally results in the formation of the desired workpiece. Producing the 3D object directly from the CAD file without the need for adaptation to the manufacturing process is a unique selling point of additive manufacturing. Depending on the field of application, an appropriate printer system can be chosen out of a multitude of commercially available printer variations with fixed specialized properties. Depending on the printing process, a vast variety of surface, robustness, and material qualities exist. Techniques and printing qualities vary from fast but less stable to more complex and costly.

Conventional 3DP is based on a layer-by-layer construction process, i.e., piling up layers with equal thickness. The layers will be stacked and bonded together and finally result in the formation of the desired object. As each layer is added and the printed object grows, staircase effects can be observed depending on the thickness of

the layer [58]. This limitation is illustrated in Figure 2.1. In this example, the printed object has a circular conduit. If the circular profile is printed layer-by-layer and along the conduit's length, as in the first example (i), there will not be any artifacts, as it can be seen in the top view. If the conduit is perpendicular to the growth direction, the final printing result is affected by the staircase effects, as shown in the second example (ii). Eventually, vertical printed structures are less precise compared to structures in horizontal line. Usually, a tradeoff between smaller and larger layer heights has to be made. The smaller the layer size, the less pronounced the staircase effect. On the other hand, larger layer sizes result in faster production with decreasing accuracy and overall printing quality. The staircase effects may become even more apparent if the layers solidify before the next one is added, leading to uneven layer surfaces. In general, this issue cannot be avoided entirely and needs to be considered in the CAD and printing speed. As a way out, a laser-based SLA variant, which is explained in Section 2.4.3, can address this shortcoming. The SLA 3DP process is introduced in detail in Section 2.4.1.

2.4.3 Multi Laser Volume Stereolithography

This section introduces the fundamental principles of MLVS. In the following, the principle of MLVS is reviewed, and the design and functionality of the prototype are reintroduced to highlight its key features and implications for the overall motivation of this dissertation project.

To better understand the practical applications of MLVS, a first prototype was developed by the author of this work [41] in 2018. Later, further improved variants of the MLVS prototype followed. Figure 2.3 depicts the newest prototype, which will be described in more detail later on.

As a new approach in freeform fabrication, the basic principle of MLVS builds up on laser-induced polymerization, and the method can be seen as a subtype of LSLA. Consequently, drawbacks like the staircase effect, the corresponding resolution loss, and shrinkage can be avoided. MLVS superimposes several laser beams focused on one point within the volume of the resin, which is illustrated in Figure 2.4.

Therefore, it is crucial to consider the number of laser beams, the intensity, and the corresponding wavelength. It is essential to have several low-intensity laser beams to stay below the critical energy for polymerization. Moreover, the resin must have low

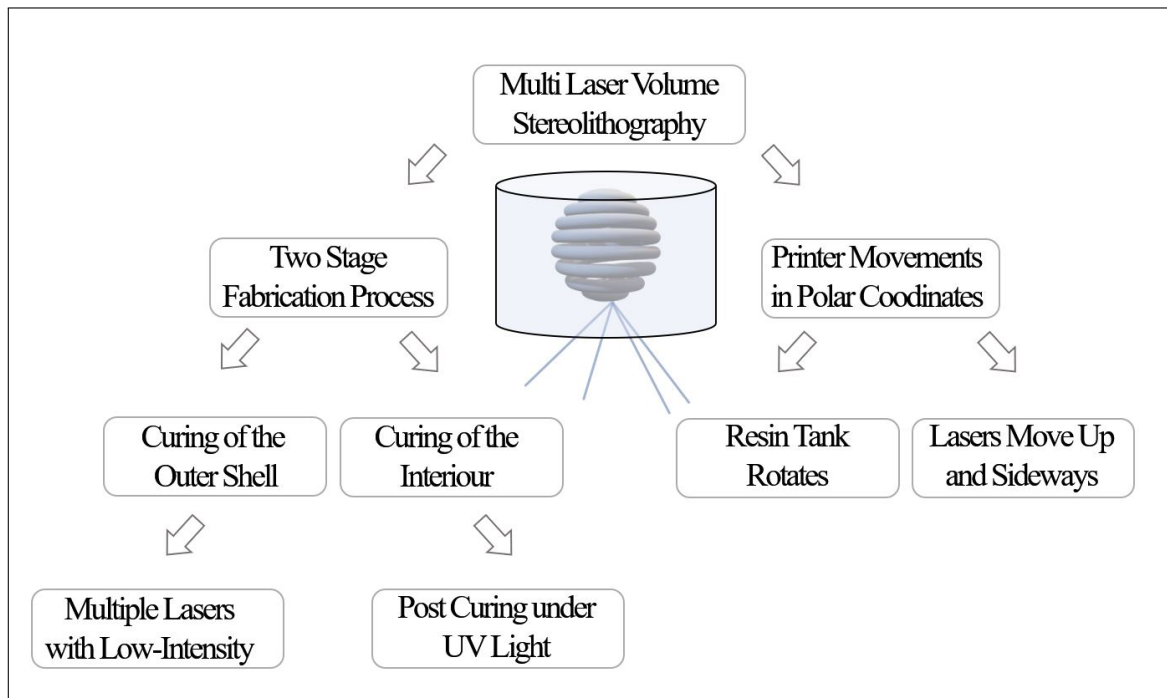


Figure 2.2: Overview of the main features of the Multi Laser Volume Stereolithography process.

absorption at the laser’s wavelength to allow a considerable penetration depth. As the critical energy is exceeded at the superposition point, the polymerization starts. Opposed to conventional LSLA methods, the curing process is done in the liquid bulk resin material instead of hardening the surface of the resin. Hence, the volumetric objects materialize from within the resin. The superimposed laser beams have to stay focused and are directed as a whole to trace the outer shell of the desired object. This enables the hardening of the object’s shell. The bulk material inside of the printed object stays liquid and can be cured posteriorly under an UV light source. Structural inequalities inside the cured volume, caused by the conventional layered process, can be avoided. The advantages of a well-defined number of interfaces are described in Chapter 6.

The laser beams are adjusted to overlap in the center of the resin volume. In this small area of overlap, the intensity of each laser is accumulated. In case each individual energy remains below the polymerization threshold, the resin is cured only in

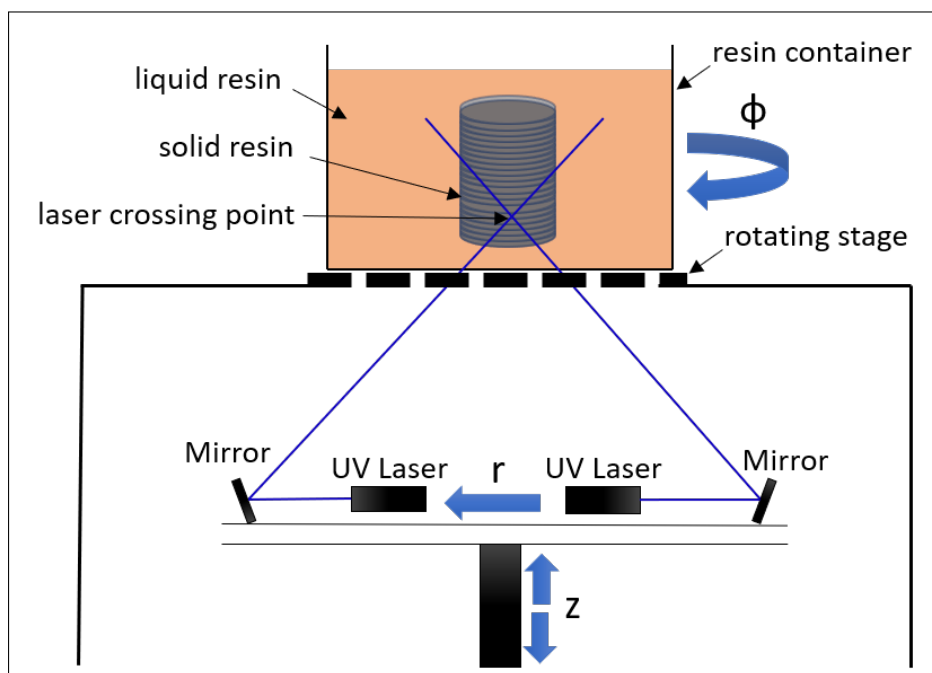


Figure 2.3: Schematic illustration of the MLVS prototype.

the overlapping area. Afterwards, the liquid interior is completely hardened by UV light, forming an utterly homogeneous polymer. On the one hand, this allows faster production of polymer dosage forms; on the other hand, it is intended to control the influence of layers on the release, as studied extensively in Chapter 6.

It is necessary to know precisely the properties that cause the polymerization reaction of the specific resin in order to realize curing within the resin reservoir instead of curing on the surface of the resin. Therefore, commercial resins are unsuitable, requiring a custom formulation that meets the printer's requirements and consists only of pharmaceutically usable materials. The primary condition for the use of MLVS is to create a polymer resin that has its maximum absorption distinctly adjacent to the laser wavelength. The PI used as part of the prototypical experiments has an absorption maximum at 381 nm [59], whereas the used laser wavelength is 405 nm.

In addition to changing the printing routine away from Cartesian coordinates to a cylindrical printing mode, the major difference of MLVS compared to SLA is using multiple laser beams. In the latest version of the MLVS prototype (cf. Figure 2.3),

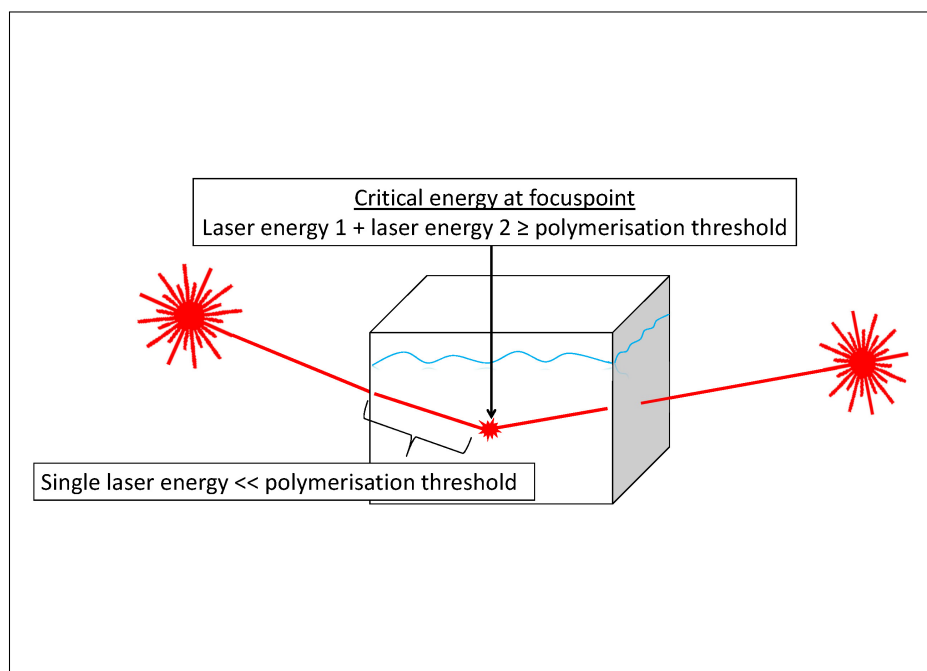


Figure 2.4: Schematic illustration of two laser beams focused into a photopolymer reservoir to one target point; Figure reproduced from [41].

multiple lasers are arranged in a circle on the printer head. The initial point of the object is cured at an arbitrary position within the resin reservoir and can grow from here to all sides. Whereas the laser beam in LSLA approaches is restricted to the surface of the resin, i.e., to the interface between air and resin, each laser beam has to pass the volume of the resin to reach the target interaction point in the case of MLVS.

Suppose a laser beam crossing the resin reservoir towards the target point has an energy level equal to or higher than the critical energy. This beam would cure a needle along its beam path, which is undesirable. Thus, single beams' laser intensity must be much lower than the critical energy level as illustrated in Figure 2.4. The energy of a single laser beam should be as low as possible to prevent initiators from building radicals outside the interaction point. Investigations on the polymerization threshold are described in Section 6.2.1.

Nonetheless, it is likely that initiators outside the focus point occasionally absorb

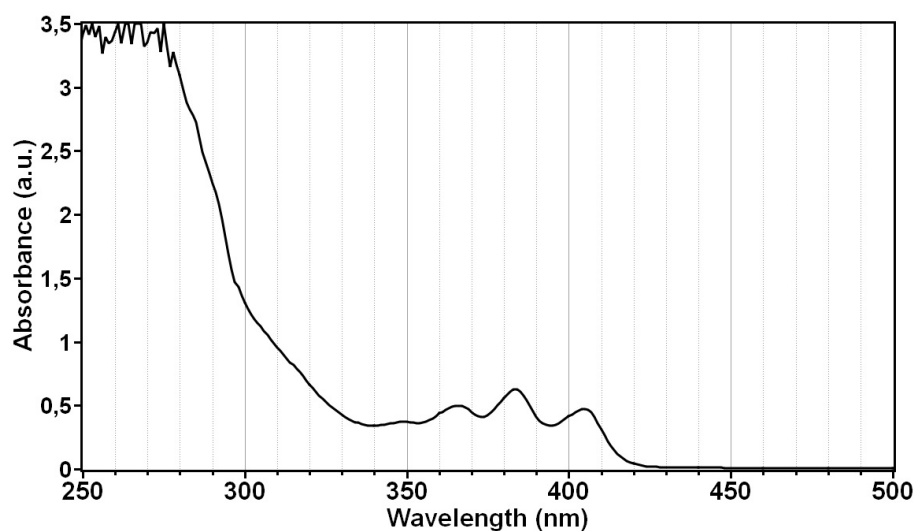


Figure 2.5: Spectral absorbance of Formlabs CLEAR resin diluted with Tetrahydrofuran. Measured with a Spectrostar Nano (sensitivity: OD range 0 to 4 OD); Figure reproduced from [41].

photons and form radicals. Especially for longer production times, this circumstance should be considered as the bulk material changes for a continuance. Once the shell is fully printed, the whole object's final curing process follows. This can take place outside of the bulk resin, which in turn, speeds up the production process. The critical energy depends on the resin composition, mainly the PI used. When using a commercial resin the polymerization threshold can be determined by measuring the progress of polymerization via a spectral analysis (optical spectroscopy). Most photopolymer resins show a high absorption of radiation with short wavelength (UV spectrum). Figure 2.5 shows the absorption spectrum of Formlabs CLEAR used in the feasibility study. Another method for the analysis of the polymerization process during irradiation via rheology is described in Chapter 6.

For the measurements, a cuvette holding the resin is placed in an open spectrometer setup with a wide spectral range (Spectrostar Nano). A laser beam with a wavelength of 445 nm is widened to constantly illuminate the entire width of the cuvette with an intensity of 50 mW⁵. The resin is irradiated in ten one second intervals with a fixed

⁵Refers to the intensity per area of the laser focal point

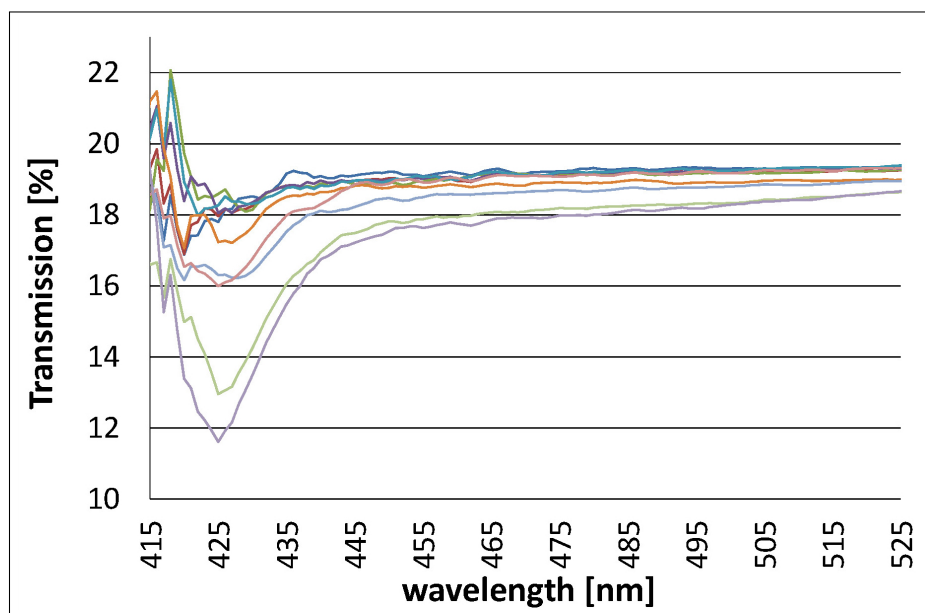


Figure 2.6: The graphs show the spectral measurements at exposure time intervals from 1 to 10 seconds. Uncured resin was used as reference; Figure modified from [41].

laser intensity. The spectral transmission is measured between the intervals, and the next irradiation interval is started instantly. Figure 2.6 shows the corresponding transmission in the range from 415 nm to 525 nm. As these measurements show, an increase in the exposure time results in decreased resin transmission. This is most evident at 425 nm. The change in absorbance over the exposure time was measured to determine the degree of conversion of the resin. Figure 2.7 shows exemplary for one measurement, the deviation at 425 nm to the reference value measured at the beginning (exp. time: 0 s). As shown in Figure 2.7, polymerization starts after five seconds, indicated by the steep increase. The liquid photopolymer resin converts into a stable polymer structure. For MLVS, the behavior of resin under laser irradiation can be classified into four phases. In the first phase, the induced power is too low to evoke any reaction within the resin. Scattered chains emerge or link up at a specific power, but the induced energy is too low to end up in long chains. This determines phase two. The third phase is relevant in the field of 3DP. Complete polymer chains arise to build stable structures. Finally, polymerization reaches the fourth phase, and no radicals are left to build chains. The resin is now thoroughly

hardened. The considerations in this chapter motivate the thesis presented here and will be continued or extended in more detail below.

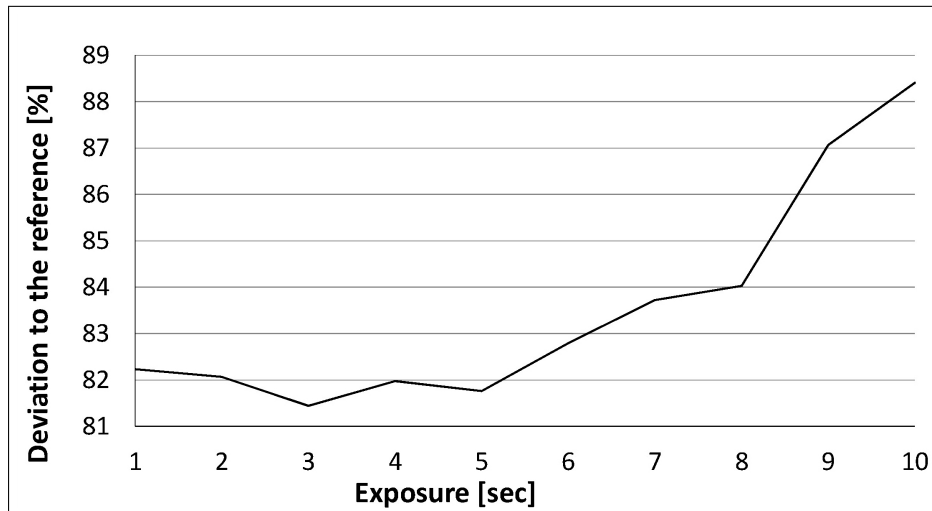


Figure 2.7: Graph showing exemplarily the deviation of the transmission at 425 nm to the reference value for the exposure intervals from 1 to 10 seconds; Figure reproduced from [41].

CHAPTER 3

Theory Framework

The following chapter addresses diffusion theory in general and in the specific case of highly cross-linked polymers. The chapter starts with general considerations of diffusion as a stochastic process, as described by the Fokker-Planck equation in Section 3.1. Then, this equation is reduced to Fick's diffusion equation with a different rationale. Special cases of solutions of Fick's diffusion are discussed. Further on, two cases of diffusion description are distinguished, one regarding the diffusion processes on a small time scale and one regarding a long time scale in Section 3.2. Finally, mathematical solutions for the modeling of diffusion profiles are described and the concrete concept of computational adjustment of these models is given in Section 3.3.

3.1 From Fokker-Planck to Fick's Law

In the following, the basic theories for diffusion analysis are presented to provide a basis for later considerations. Every experimental study ought to be preceded by consideration of which model is suitable for describing the data obtained. This serves to prevent the common mistake of using a model that is too complex for the data basis or the problem to be discussed. If the model is too complex for the data being

analyzed, this can easily lead to misinterpretation.

Fokker-Planck Equation

The Fokker-Planck equation [60–63] describes the evolution of a probability function of uncorrelated events over time and can be applied to stochastic processes. Stochastic processes for instance range from Brownian motion to passenger traffic in airports to cosmological structure formation [64–67]. The Fokker-Planck equation is also the basic approach to diffusion of molecules as a stochastic process, as investigated in this thesis. In the context of this work, the "event" is the occurrence of a molecule (water or drug particle) at a particular location in a polymer. This means that the particle can either have entered from the adjacent volume or be formed by a reaction. The 'location' in a continuum theory, such as Fokker-Planck theory, is a reference volume where multiple molecules can be described (to a good approximation) by an actual number, usually called the 'concentration' c . It is typically normalized between $0 < c < 1$, where the limits 0 and 1 are excluded by the laws of thermodynamics. In this thesis the standard expression is used, that $p(x, t)$ describes the probability of finding a given number of molecules within a reference volume at position $x \pm \Delta x$ and time $t \pm \Delta t$. Δx and Δt are the expansion of the reference volume and the averaging time over fluctuations. The Fokker-Planck equation in its standard form reads:

$$\frac{\partial p(x, t)}{\partial t} = -\frac{\partial}{\partial x}[\mu(x)p(x, t)] + \frac{\partial}{\partial x} \left[D(x) \frac{\partial p(x, t)}{\partial x} \right] \quad (3.1)$$

where $p(x, t)$ is the probability density function, $\mu(x)$ represents the drift velocity, and $D(x)$ is the space-dependent diffusion coefficient. In general, and in particular in the case of diffusion in polymers, the diffusion coefficient can also be a function of the concentration of molecules $D(x)$ is $D(p(x, t), x)$. The diffusion coefficient as a function of space is, therefore, better represented as a diffusion coefficient as a function of space and concentration. Due to this function's non-linearity, solutions with time oscillations are permitted [61]. However, this aspect is just touched upon in this paper.

A special case of the Fokker-Planck equation 3.1 is given by the drift velocity being related to the diffusion coefficient: $\mu(x) = \frac{\partial}{\partial x} D(x)$. Equation (3.1) then becomes:

$$\begin{aligned}\frac{\partial p(x, t)}{\partial t} &= -\frac{\partial}{\partial x} \left[\frac{\partial}{\partial x} D(x) p(x, t) \right] + \frac{\partial}{\partial x} \left[D(x) \frac{\partial p(x, t)}{\partial x} \right] \\ &= -\left(\frac{\partial^2}{\partial x^2} D(x) \right) p(x, t) + D(x) \frac{\partial^2}{\partial x^2} p(x, t)\end{aligned}\quad (3.2)$$

The last term in equations 3.1 to 3.2 is also called Fick's diffusion; see below. Compared to this diffusion law, the middle term in 3.2 emphasizes the effect of non-linearity in the diffusion coefficient. The first term, linearly proportional to the probability function $p(x, t)$, acts as a sink or source term, dependent on the sign of the second derivative $\frac{\partial^2}{\partial x^2} D(x)$. If the probability function is related to the density of molecules in a reference volume, such as sinks or sources must be excluded or related to chemical reactions where molecules are created or consumed.

Fick's Diffusion

Fick's law of diffusion focuses on concentration gradients in a diffusional system, while the Fokker-Planck equation can handle more complex probabilistic scenarios, including variable diffusion coefficients and external forces. By ignoring any drift or external forces the Fokker-Planck equation becomes similar to the Fick's Law. Assuming there is no drift ($\mu(x) = 0$), the equation reduces to:

$$\frac{\partial p(x, t)}{\partial t} = D \frac{\partial^2 p(x, t)}{\partial x^2}\quad (3.3)$$

Whereas the directly analogous form of second Fick's law of diffusion is 3.4:

$$\frac{\partial c}{\partial t} = D \frac{\partial^2 c}{\partial x^2}\quad (3.4)$$

Where $c(x, t)$ corresponds to the concentration of particles, and $p(x, t)$ is the probability density function in the Fokker-Planck context. Concluding, Fick's law assumes that the velocity of each movement step depends on the conditions at its endpoint, while Fokker-Planck's law assumes that the velocity of movement depends on the conditions at its starting point [61].

Bringuier argues that Fick's law is particularly suitable if the diffusion has a physical origin, for example, through turbulent flows in the medium that are spatially

inhomogeneous due to geometric boundary conditions [68]. This type of diffusion is referred to as physical diffusion. In contrast, the Fokker-Planck law describes diffusion when the inhomogeneity is caused by temperature or density gradients of the medium, such as the accumulation of molecules in colder areas.

Fick's First Law

As described in Equation 3.5, the flux of a diffusing substance is proportional to the negative gradient of its concentration.

$$J = -D \frac{\partial C}{\partial x} \quad (3.5)$$

where J is the flux, D is the diffusion coefficient, and $\frac{\partial C}{\partial x}$ is the concentration gradient.

Fick's Second Law

The second law describes how the concentration of a substance changes over time, considering the rate of change in concentration and the diffusion in space, as it is given by Equation 3.6:

$$\frac{\partial C}{\partial t} = \frac{\partial}{\partial x} J = \frac{\partial}{\partial x} \left[D \frac{\partial C}{\partial x} \right] \quad (3.6)$$

In the following, different approaches for the applications in this work are discussed following a description of important terms and concepts.

3.2 Terms and Concepts of Diffusion

In this section, basic terms and concepts relating to the highly cross-linked and little swelling polymers used in this work and the release of active pharmaceutical ingredient (API) from these polymers are described below.

High Cross-linked Little Swelling Polymers

This thesis focuses on polymers primarily composed of the cross-linking polymer Poly(ethylene glycol) dimethacrylate (PEGDMA). These materials are categorized

as highly cross-linked polymers, characterized by a water uptake of less than 25% in the fully swollen state [69]. Upon placing the sample in a tempered medium, a thermal equilibrium begins to establish. In the context of this thesis, this process occurs very rapidly, given the small size of the sample, and is therefore not considered further, as it is deemed to have no significant effect on the diffusion mechanisms investigated. Concurrently, the aqueous medium starts to permeate the sample, leading to the dissolution of the API contained within it.

A distinction is made between these two diffusion processes: one involves the medium diffusing into the sample, while the other refers to the diffusion of the API from the sample into the medium. It is important to note that these two processes are inherently interrelated, influencing one another. However, for the purposes of this discussion, we will treat them as separate processes to better assess their individual impacts on the overall process.

Diffusion in the Short Term

In this context, we refer to the diffusion process in the short term as the initial two hours of immersion. During this period, the penetration of an aqueous medium into the sample, along with the outflow of air from it, is anticipated to be a short term process due to the small size of the sample. The medium infiltrates the sample simultaneously from all sides, and once it has fully permeated, it continues to pass through. The polymer, which is hydrophilic and insoluble, begins to expand within the warm aqueous medium. The individual bonds within the polymer network, which consists of cross-linked polymers, become more flexible and allow the overall structure to be stretched. This phenomenon is known as swelling. To summarize, the weight of the sample and its volume increase as the medium penetrates the polymer. Despite the fact that penetrating water is the cause of both increases, it is reasonable to assume that the two processes take different courses. The volume increase resulting from swelling is expected to be inert, as the volume of the polymer network adjusts due to the relaxation of its polymer bonds. However, the resulting degree of freedom from this process is relatively low, owing to the use of cross-linked polymers with reactive ends on both sides. A detailed description of the actual network properties can be found in Chapter 6.

The increase in sample mass due to water absorption serves as a measure of the polymer network's capacity to absorb water. This process can be assumed to start immediately upon immersion in the medium and concludes once the network has reached saturation with water. Obviously, the partial temporal overlap of both processes, the swelling, and the mass increase, suggests that there is a mutual influence between them.

For completeness, the spontaneous release of drug substance from the outside of the sample is mentioned here. This phenomenon, known as the burst effect, occurs within the first few seconds and can be easily corrected by adjusting the offset of the measurement curve. This is concerned in greater detail in Chapter 5.

Diffusion in the Long Term

In this thesis, diffusion on a long time scale refers to processes that occur over several hours to a few days. During this period, it is assumed that shorter processes, such as mass uptake and swelling, have concluded, leading to a steady release of the API. This release primarily results from particle diffusion driven by a concentration gradient created by the absence of the API in the surrounding medium. If the saturation limit of API in the medium is considered sufficiently distant, the release of API is expected to follow a linear course controlled by pure Fickian diffusion. However, it is to be expected that deviations from this linearity will appear when analyzing the actual measurement data, potentially due to steric hindrances and interactions between the materials. The possible modeling of a specific release profile is even advantageous. These processes are of particular interest for pharmaceutical applications. Due to the absence of non-anomalous effects, these processes can be described by Fickian diffusion.

3.3 Mathematical Description of Diffusion

A wide range of methods is available for the mathematical description of diffusion data. One possible solution is to describe a release curve using a fifth- or sixth-order polynomial function. The concentration C is then described as follows:

$$C(x, t) = A_0(t) + A_1(t)x + A_2(t)x^2 + A_3(t)x^3 + A_4(t)x^4 + A_5(t)x^5 \quad (3.7)$$

However, it is important to understand that the parameters A_0 to A_5 determined this way must be interpreted first in order to provide an insight into the samples diffusion properties. Things get more complex when it comes to identifying a simulation function that only uses those fit parameters, providing insights into the release profile.

Variable Separation

Consideration of the diffusion of a substance in a one-dimensional finite medium with the length L and the concentration c . $c(x, t)$ fulfils the following conditions:

$$c(x, 0) = c_0 \quad (3.8)$$

$$c(0, t) = 0 \quad (3.9)$$

and

$$c(L, t) = 0 \quad (3.10)$$

A solution of Fick's Second Law by separating the variables into a product of functions of x and t is given as described below [7]. Equation 3.11 is substituted into Fick's diffusion equation, resulting in Equation 3.12:

$$c(x, t) = X(x)T(t) \quad (3.11)$$

$$X(x) \frac{dT(t)}{dt} = DT(t) \frac{d^2X(x)}{dx^2} \quad (3.12)$$

Both sides are divided by $X(x)T(t)$, and in order to separate in a temporal and a spatial part, the separation constant λ is introduced:

$$\frac{1}{DT(t)} \frac{dT(t)}{dt} = \frac{1}{X(x)} \frac{d^2X(x)}{dx^2} = -\lambda \quad (3.13)$$

First, the temporal part is solved:

$$\frac{dT(t)}{dt} = -D\lambda T(t) \quad (3.14)$$

Resulting in:

$$T(t) = T_0 e^{-D\lambda t} \quad (3.15)$$

Here, the spatial part is solved:

$$\frac{d^2 X(x)}{dx^2} + \lambda X(x) = 0 \quad (3.16)$$

The solution is given in:

$$X(x) = A \sin(\sqrt{\lambda}x) + B \cos(\sqrt{\lambda}x) \quad (3.17)$$

The following conditions are applied:

$$x = 0 : X(0) = 0 \text{ so } B = 0 \text{ so } X(x) = A \sin(\sqrt{\lambda}x) \quad (3.18)$$

$$x = L : X(L) = 0 \text{ so } \sin(\sqrt{\lambda}L) = 0 \quad (3.19)$$

With $\sqrt{\lambda}L = n\pi$, it follows:

$$\lambda = \left(\frac{n\pi}{L}\right)^2 \quad (3.20)$$

The substitution of λ and the combination of the temporal and spatial parts finally results in Equation 3.21.

$$c(x, t) = \sum_{n=1}^{\infty} A_n \sin\left(\frac{n\pi x}{L}\right) e^{-D\left(\frac{n\pi}{L}\right)^2 t} \quad (3.21)$$

The coefficients A_n are the Fourier sinusoidal coefficients that determine the amplitudes of the different sinusoids in the solution. They are determined by the initial conditions of the diffusion process as given in 3.8,3.9,3.10,3.18,3.19. Resulting in:

$$A_n = 4c_0/m\pi, \quad m = 1, 3, 5, \dots \quad (3.22)$$

In conclusion, the solution given in Formula 3.21 can describe a diffusion process that takes place in a one-dimensional sample of finite size. This applies, for example, to polymer films or flat samples in relation to their horizontal expansion. This formula seems inappropriate at first glance when using three-dimensional samples with a specific height, width, and length. To evaluate this, however, we should first

consider how the actual measurement data is obtained and what can be extracted from it.

The samples used in this thesis are non-soluble polymers of cubic dimensions that contain a homogeneously distributed drug substance. When immersed in an aqueous medium, this substance penetrates through the polymer. The concentration of this active ingredient in the aqueous liquid is then analyzed. It is therefore not possible to determine from which side of the sample the active substance has diffused on the basis of the measurement data. Due to the continuous stirring of the solution, the measurement is averaged over time and space.

When using samples of the same shape and size, the actual dimensions are relevant as they influence the magnitude of the diffusion coefficient. If the mathematical description of the measurement curves is primarily intended to compare the curves with each other, the actual magnitude of the diffusion coefficient is of minor importance.

Spatial Diffusion Coefficients

Nevertheless, there may be valid reasons to consider the actual sample dimensions and/or to analyze the diffusion separately in three spatial directions. In this thesis, a directional analysis of diffusion is employed, particularly in Chapter 6. Two approaches are considered in this section, namely the Laplacian approach and the Fourier series approach.

Three-dimensional Laplacian Solution

In order to focus on the mathematical modeling of diffusion in polymers, a solution is given using the three-dimensional Laplace operator. The diffusion of molecules within a polymer matrix is described by the diffusion equation, which in its general form is given by:

$$\frac{\partial c(r, t)}{\partial t} = D \nabla^2 c(r, t) \quad (3.23)$$

Where $c(r, t)$ is the concentration of the diffusing species at position r and time t , and D is the diffusion coefficient. The term ∇^2 represents the Laplace operator, which in three dimensions is expressed as:

$$\nabla^2 = \frac{\partial^2}{\partial x^2} + \frac{\partial^2}{\partial y^2} + \frac{\partial^2}{\partial z^2} \quad (3.24)$$

This equation describes the temporal evolution of the concentration field, where the Laplace operator accounts for the spatial distribution of the diffusing molecules. In the context of polymers, the diffusion coefficient D may vary spatially due to the heterogeneity of the material, leading to more complex forms of the equation, such as:

$$\frac{\partial c(r, t)}{\partial t} = \nabla \cdot (D(r)\nabla c(r, t)) \quad (3.25)$$

where $D(r)$ is the spatially dependent diffusion coefficient.

Boundary and initial conditions are crucial for solving this equation in specific polymer systems. We define the Dirichlet boundary conditions to be:

$$c(r, 0) = c_0 \quad \text{for all } r \in \Omega \quad (3.26)$$

Where c_0 is the initial concentration and Ω represents the body of the polymer where the diffusion process is considered.

Three-dimensional Fourier Series Solution

To extend the solution of the diffusion equation from a one-dimensional to a three-dimensional solution, we consider Fick's second law of diffusion in the three-dimensional form:

$$\frac{\partial c(x, y, z, t)}{\partial t} = D \left(\frac{\partial^2 c}{\partial x^2} + \frac{\partial^2 c}{\partial y^2} + \frac{\partial^2 c}{\partial z^2} \right) \quad (3.27)$$

or in case of spatial diffusion coefficients:

$$\frac{\partial c(x, y, z, t)}{\partial t} = D_x \frac{\partial^2 c}{\partial x^2} + D_y \frac{\partial^2 c}{\partial y^2} + D_z \frac{\partial^2 c}{\partial z^2} \quad (3.28)$$

As previously, the variables are separated:

$$c(x, y, z, t) = X(x)Y(y)Z(z)T(t) \quad (3.29)$$

Solving the separate parts results in the following form:

$$c(x, y, z, t) = \sum_{n=1}^{\infty} \sum_{m=1}^{\infty} \sum_{p=1}^{\infty} A_n \sin\left(\frac{n\pi x}{L_x}\right) \sin\left(\frac{m\pi y}{L_y}\right) \sin\left(\frac{p\pi z}{L_z}\right) e^{-D\left(\left(\frac{n\pi}{L_x}\right)^2 + \left(\frac{m\pi}{L_y}\right)^2 + \left(\frac{p\pi}{L_z}\right)^2\right)t} \quad (3.30)$$

and in case of spatial diffusion coefficients:

$$c(x, y, z, t) = \sum_{n=1}^{\infty} \sum_{m=1}^{\infty} \sum_{p=1}^{\infty} A_n \sin\left(\frac{n\pi x}{L_x}\right) \sin\left(\frac{m\pi y}{L_y}\right) \sin\left(\frac{p\pi z}{L_z}\right) e^{-\left(\frac{n^2\pi^2 D_x}{L_x^2} + \frac{m^2\pi^2 D_y}{L_y^2} + \frac{p^2\pi^2 D_z}{L_z^2}\right)t} \quad (3.31)$$

It is questionable whether a curve fitting with three different diffusion coefficients is reasonable due to the experimental data collection method described in Section 5.2. The fact that the diffusion coefficients are weighted by the respective sample dimension, as can be seen from Equation 3.31, makes a realistic determination of three separate coefficients by curve fitting implausible. A sensible implementation of Equation 3.31, on the other hand, is described in detail in Chapter 6.

Fickian and Non-Fickian Diffusion

Up to this point, only Fickian diffusion has been mentioned. However, it is reasonable to expect non-Fickian diffusion to be involved in the process. Further considerations on this topic are given in Chapter 4. Therefore, a concrete solution of the diffusion Equation 3.21 in the one-dimensional case will be considered first in Equation 3.32:

$$\frac{M_t}{M_{\infty}} = 1 - \sum_{n=0}^{\infty} \frac{8}{(2 \cdot n + 1)^2 \cdot \pi^2} e^{\left\{ \frac{-D(2 \cdot n + 1)^2 \pi^2 t}{4l^2} \right\}} \quad (3.32)$$

where M_t and M_{∞} are the mass of the drug substance at a certain time and the total amount of substance in the sample, respectively, and $l = L/2$.

By adding a second term for the non-Fickian diffusion part and using ϕ_F and ϕ_R as weights for both parts, we get the following expression:

$$\frac{M_t}{M_\infty} = \phi_F \left[1 - \sum_{n=0}^{\infty} \frac{8}{(2 \cdot n + 1)^2 \cdot \pi^2} e^{-\frac{D \cdot (2 \cdot n + 1)^2 \cdot \pi^2 \cdot t}{4 \cdot l^2}} \right] + \phi_R [1 - e^{-k_R \cdot t}] \quad (3.33)$$

where k_R is defined as the relaxation constant, which refers to the time in which the material is entirely relaxed. If the weighting ϕ_F and ϕ_R of both parts is unknown, they could be estimated by curve fitting, just like the diffusion coefficient and the relaxation constant. This is applied in Chapter 5.

A solid basis of measurement data is crucial when using a curve fitting algorithm. The simulated curve should be interpreted considering any errors that might have occurred during the measurement. This is discussed in more detail in the following chapter.

CHAPTER 4

Diffusion Simulation

The following chapter serves to gain general insight into the diffusion processes in the sample, to identify the factors influencing the analysis of the experimental data for diffusion measurements, and to compare the mathematical diffusion models. Two sources of potential bias on the experimental data were identified in advance and are analysed in Section 4.1. The first relates to the strength of the concentration gradient - when using a dissolution apparatus in accordance with the guidelines of the Pharmaceutical Pharmacopoeia [70], the dissolution medium in which the sample is placed is constantly stirred (which is explained in more detail in the experimental part). This leads to a permanently maximized concentration gradient at the interface between polymer and water. However, the common diffusion descriptions are based on undisturbed systems in which the release is only driven by the diffusion coefficient of the individual media. Consequently, a stirred and a non-stirred system are simulated below using finite differences and compared with each other. The second potential source of error is the homogeneity or inhomogeneity of the sample. The homogeneity of the active pharmaceutical ingredient (API) distribution is of particular interest due to the unique approach of this study, in which the API is already added to the polymer resin mixture and incorporated into the samples during manufactur-

ing (see Chapter 5). In the second part of this chapter in Section 4.2 mathematical descriptions, described in Section 3.3, are compared using experimental data. This step serves to approach the question of which model is reasonable and useful. True to the motto: The simplest possible model delivers the most reliable results.

4.1 Simulating Special Cases of Diffusion

The concentration profiles that describe the diffusion process within a polymeric material can be described by the Laplace operator in all the spatial dimensions. For the simulation of the diffusion process, a three-dimensional matrix was used in Python, which represents the dimensions of the sample plus a water area. As initial values, each cell in the polymer is assigned the initial concentration (e.g. 100 %) and the cells in the water area is assigned 0%. Then, the concentration in each cell is recalculated iteratively by solving the Laplace operator in all the spatial dimensions. Each iteration describes a time step and thus the course of the diffusion profile.

The simulations presented below aim, on the one hand, to contribute to the understanding of the processes in the three-dimensional polymer sample and, on the other hand, to estimate the sources of error arising from the boundary conditions imposed by the experimental setup. Diffusion is primarily dependent on the gradient of the concentration. It can, therefore, be assumed that a change in the concentration gradient strongly influences the diffusion gradient. In order to investigate the assumptions underlying the experiment in this respect, two cases are simulated and considered in the following.

The first case refers to the concentration gradient that forms directly on the outer shell of the sample. In an undisturbed system, the API released into the water will remain close to the outer shell for a while before dispersing throughout the water. However, if the water is constantly stirred by a paddle, the API is dispersed instantaneously, leading to a permanent maximum concentration gradient on the interface between polymer and dissolution medium.

The diffusion in an undisturbed system is depicted in Figure 4.1. The plot shows a cross-section of the drug concentration in the sample over time. The horizontal axis represents the spatial axis, while the vertical axis represents the percentage concentration. With increasing iterations (500 in total), the lines of the graph becomes

lighter (gradient from black to white). The vertical dashed line at the zero position indicates the interface between the sample and water.

It can be observed that the amount of API diffused in each spatial direction differs due to the varying thicknesses of the sample in each spatial direction. Looking at the last iteration (bottom white line), the ratio of API outside the polymer in water to API inside the polymer is 1 : 1.9 on the y-axis, 1 : 1.3 on the x-axis and only 1 : 0.18 on the thinnest side of the polymer, which is shown on the z-axis. It becomes clear that the majority of the API leaves the polymer via its thinnest side.

Figure 4.2, on the other hand, shows the simulation of a system in which the water is continuously stirred. Since the volume of the solution is very large compared to the polymer sample and the amount of diffused substance is very small, the value of the concentration in solution can be set to zero as a very good approximation. This considerably simplifies the simulation under stirring. It is assumed that the amount of water is large enough so that the active ingredient saturation is never reached. The resulting steep gradient between the API concentration inside and outside the sample clearly leads to an accelerated release compared to the undisturbed system.

After the same amount of time, on average, only $7.3 \cdot 10^{-9}$ % of the API remains in the polymer in the stirred system. In the unstirred system, it is still 8.6 % on average. It is important to remember that the diffusion coefficient in the polymer is the same in both systems. The simulation at low times does not take water absorption into account. This is why different curve profiles can be expected here.

In the further course of this work, all experiments are implemented according to the specifications of the European Pharmacopoeia under section 2.9 on drug release [70]. These specifications require measurement in a continuously stirred system. A certified apparatus as described in Section 5.2 is used for release testings in this thesis. As can be seen from the considerations presented above, the measurements obtained this way are not comparable with those in an undisturbed system. Although this does not accurately represent the real scenario of a polymer implant in the human body, it is a worthwhile tradeoff as the experiments in a stirred system lead to an improved reproducibility. Therefore, it is advisable to consider longer release times of more than eight hours.

The second case, which is considered with the aid of simulation, examines the homogeneity or inhomogeneity of the API distribution in the polymer. The effect of a

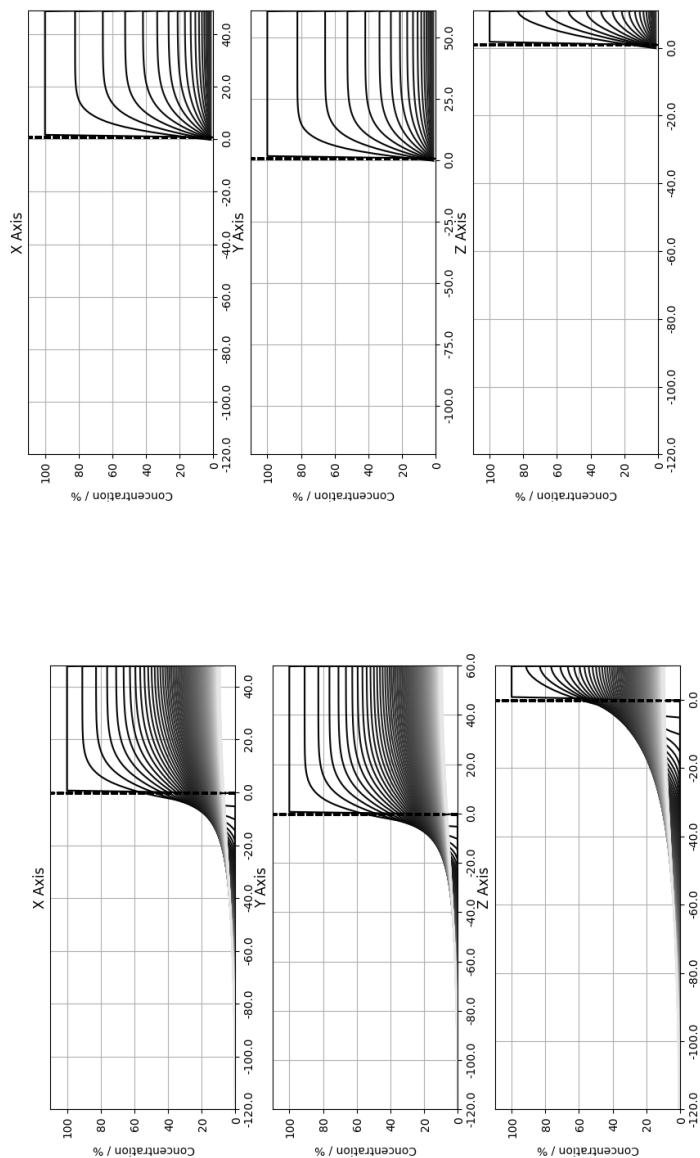


Figure 4.1: Simulation of the API release from the sample into the water over time without stirring. From top to bottom, the release profile is shown on the x, y, and z-axis over 500 iterations. The dashed line represents the interface between polymer (right side) and water (left side).

Figure 4.2: Simulation of the API release from the sample into the water over time while constant stirring. From top to bottom, the release profile is shown on the x, y, and z-axis over 500 iterations. The dashed line represents the interface between polymer (right side) and water (left side).

possible inhomogeneous distribution of API on the results of the release experiment is estimated. Figure 4.3 shows an example of a distribution that alternates locally between 90 % and 100 % API concentration.

Concentration Pattern %	Average Concentration %		Average Variance	
	Start	End	Start	End
100/100	100.00	0.82	0.00	0.09
100/90	94.79	0.78	26.06	0.08
100/50	74.94	0.61	651.61	0.05
100/10	53.08	0.45	2111.20	0.03

Table 4.1: Release profiles from samples with four different concentration pattern are simulated. These pattern are, a homogeneous concentration at top row, followed by an alternating concentration of 100 % and 90 %; 100 % and 50 % and 100 % and 10 %. The average concentration and variance in each sample is given before and after release simulation. The simulation was conducted under constant stirring with 100 iterations.

Over time, there is a clear smoothing of the curves until the concentration fluctuations disappear completely. In the last iteration step, the variance has decreased from initially 26.06 to 0.08. In comparison, in the homogeneous system the variance increases from 0.0 to 0.09 %. In Table 4.1 an overview of four different concentration pattern and their average concentration and variance before and after release simulation is given. The average API concentration in the sample is reduced to larger inhomogeneities before and after the release simulation. At the beginning, the variance naturally increases strongly with greater inhomogeneity. At the end of the simulation, however, the variance is reduced more strongly with increasing inhomogeneity. This can also be attributed to the lower concentration values.

In conclusion, it becomes clear that an increased inhomogeneity, which results in a reduction of the total API concentration in the sample, has a significant effect on the release behavior. Accordingly, it is essential to ensure the chemical stability of the resins and the samples. This matter is addressed in particular in the experimental section in Chapters 5 and 7.

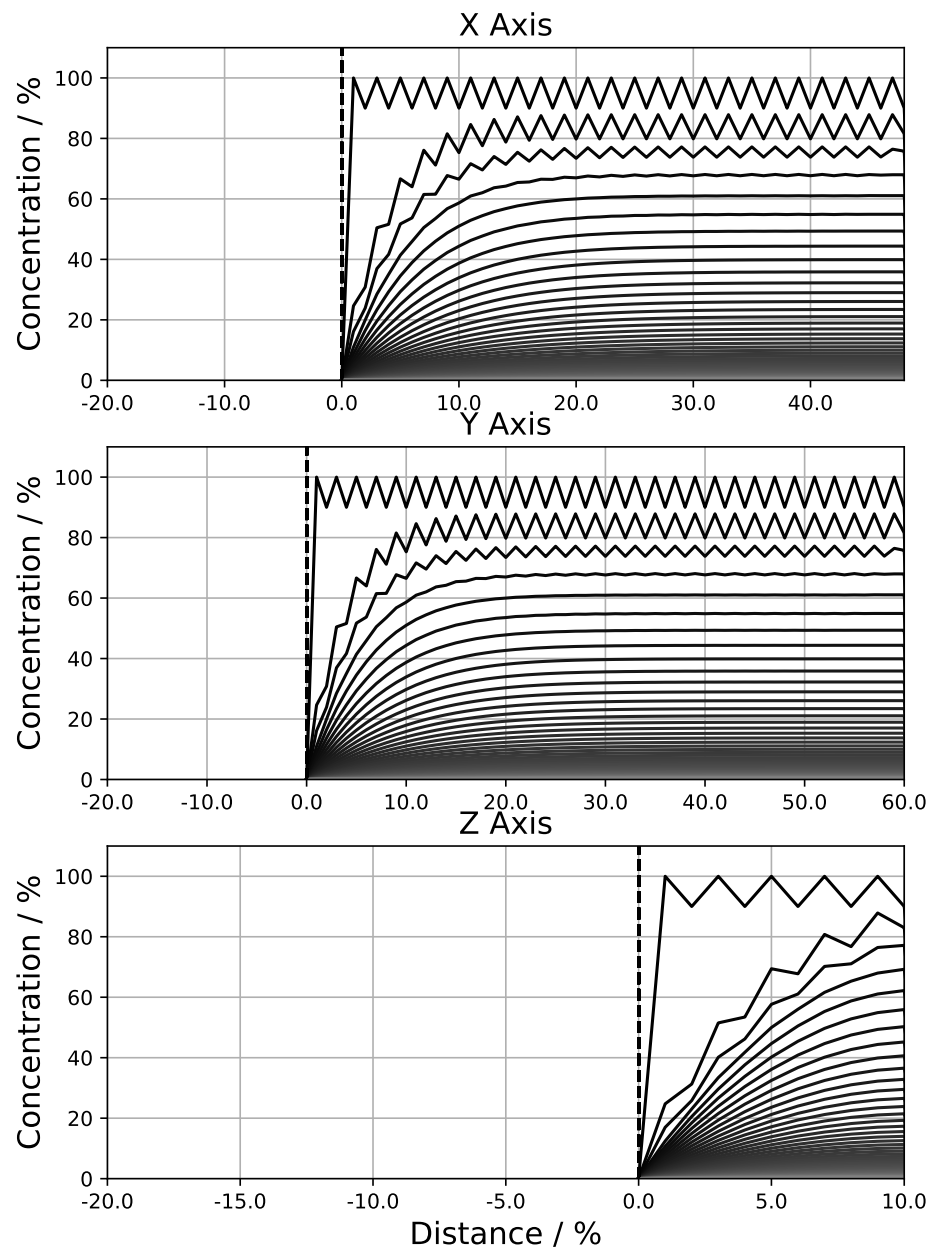


Figure 4.3: Simulation of the API release from an inhomogeneous sample into the water over time under constant stirring. The initial concentration varies between 90% and 100%. From top to bottom, the release profile is shown on the x, y, and z-axis over 100 iterations. The dashed line represents the interface between polymer and water.

4.2 Regression Analysis of Diffusion Data

In the following, the data of a drug release measurement are fitted by regression analysis using a Python curve fitting algorithm. Two variants of the Laplacian solution (Equations 3.23 and 3.24) and two of the Fourier series solution (Equations 3.33 and 3.30) are used comparatively. The free parameters are fitted by the Python curvefit function. The error estimation of the fitting parameters is performed by a Python bootstrap algorithm with three repetition cycles. Release measurement data from sample S_{194} is used here for the calculation. The collection of measurement data is described in more detail in Chapter 5. The following analyses are addressed below: Determination of the non-concentration-dependent and the concentration-dependent diffusion coefficient by curve fitting using the Laplacian solution; determination of the diffusion coefficient by curve fitting using one-dimensional and three-dimensional Fourier series solutions.

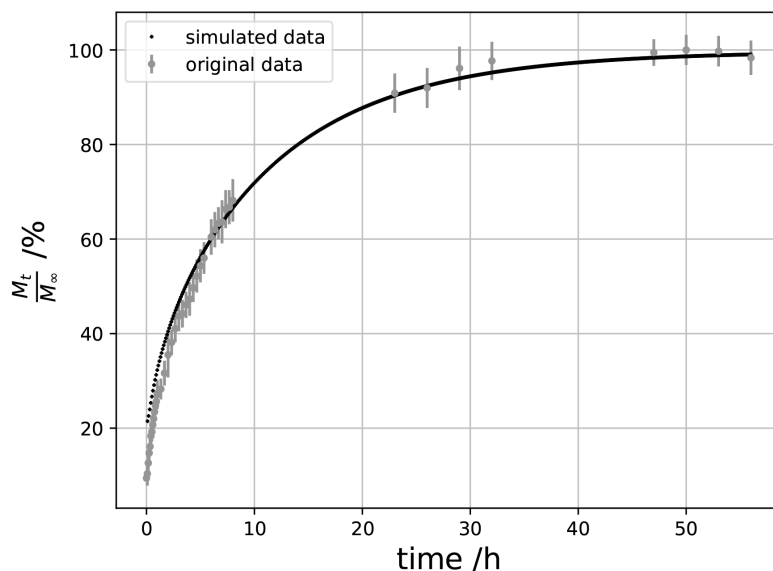


Figure 4.4: Graph depicting the original measurement of a diffusion measurement of sample S_{194} , and the corresponding interpolated error bars shown in gray. The modeled data curve (small black dot) was fitted with Equations 3.23 and 3.24. The fitting parameter is a non-concentration-dependent diffusion coefficient.

As can be seen in Figure 4.4, the Laplacian solution effectively models the measured data at long time scales, with the fitted curve remaining within the measurement error bars. However, the modeled curve deviates upwards for short measurement times. The non-concentration-dependent diffusion coefficient has been determined to be $5.05 \cdot 10^{-12} \text{ m}^2/\text{s} \pm 8.91 \cdot 10^{-15} \text{ m}^2/\text{s}$. In examining the concentration-dependent diffusion coefficient, shown in Figure 4.5, it appears that the simulated curve fits the measured data more accurately in the lower concentration range, specifically during the initial eight hours and around the 40-hour mark. In this case, the diffusion coefficient is treated as a linear function of concentration, with a negative gradient of $\epsilon = -3.12 \cdot 10^{-7} \text{ m}^2/\text{s} \pm 2.22 \cdot 10^{-8}$

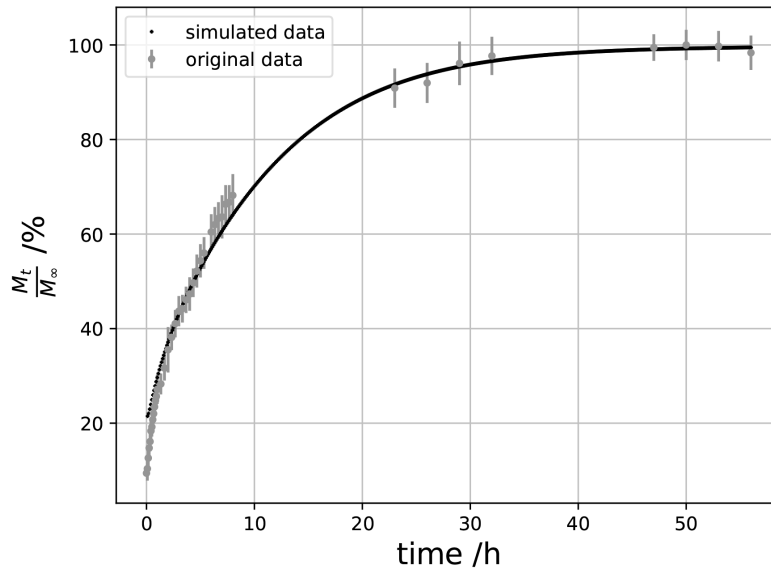


Figure 4.5: Graph depicting the original measurement of a diffusion measurement of sample S_{194} , and the corresponding interpolated error bars shown in gray. The modeled data curve (small black dot) was fitted with Equations 3.23 and 3.24. The fitting parameter is a concentration-dependent diffusion coefficient.

The fitted diffusion coefficient is $5.78 \cdot 10^{-12} \text{ m}^2/\text{s} \pm 1.01 \cdot 10^{-13} \text{ m}^2/\text{s}$, which is slightly higher than the non-concentration-dependent parameter. Since both simulated curves lie widely within the measurement errors, it remains unclear whether

a concentration-dependent calculation of the diffusion coefficient offers superior accuracy. The description of the API release by non-Fickian diffusion, for example by a complex model such as the Fokker-Planck equation, can therefore not be justified here. Figure 4.6 illustrates the curve simulated using Equation 3.30, which fits the data exceptionally well. The underlying function is derived from a solution of the three-dimensional Fourier series, as described in Equation 4.6. The diffusion coefficient, assumed to be uniform across all spatial directions, was determined through curve fitting to be $8.56 \cdot 10^{-12} \text{ m}^2/\text{s} \pm 4.23 \cdot 10^{-14} \text{ m}^2/\text{s}$. For comparison, Figure 4.7 presents the curve fitted with Equation 3.33. This fitting approach is based on the premise that a portion of the drug is released via pure Fickian diffusion, while another portion follows a so-called non-Fickian diffusion pattern. For this purpose, the fitting is done in two separate steps.

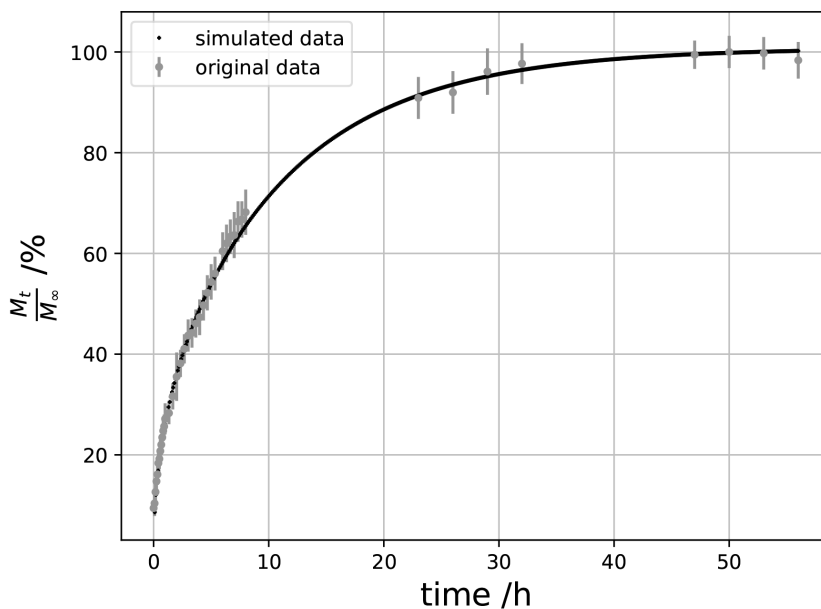


Figure 4.6: Graph depicting the original measurement of a diffusion measurement of sample S_{194} , and the corresponding interpolated error bars shown in gray. The simulated data curve (small black dot) was fitted with Equation 3.30.

First, the release range over eight hours is fitted with the non-linear part of the for-

mula. Non-Fickian diffusion is assumed to dominate in the first part of the release. The diffusion coefficient of the entire curve is then determined to be $5.61 \cdot 10^{-12} \text{ m}^2/\text{s} \pm 3.34 \cdot 10^{-13} \text{ m}^2/\text{s}$. Notably, this curve exhibits the most significant deviation compared to the other three simulations. In the eight-hour range, this model fits the measurement curve considerably better compared to the other models. Towards long times, however, it fits less accurately.

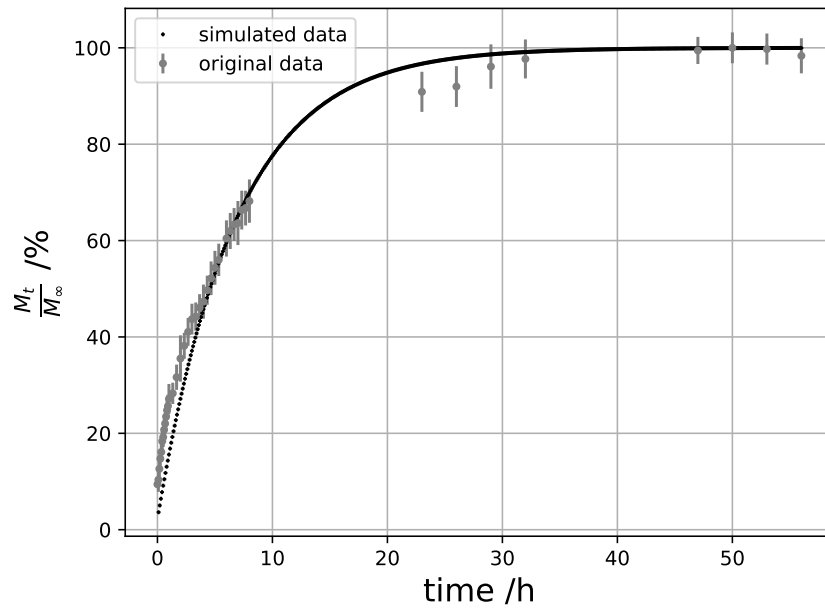


Figure 4.7: Graph depicting the original measurement of a diffusion measurement of sample S_{194} , and the corresponding interpolated error bars shown in gray. The simulated data curve (small black dot) was fitted with Equation 3.33.

4.3 Conclusion

According to the results of the simulation described in Section 4.1, it is clear that there is a major difference between stirred and unstirred systems. It is therefore not meaningful to compare the release of an undisturbed system with that of a disturbed system. The evaluation of diffusion coefficients determined by diffusion models must

therefore be carried out in relation to the measurement method. Furthermore, the influence of the geometry of the sample becomes apparent. The dominance of the release through the thinnest side of the sample can be decisive in the choice of the diffusion model. The homogeneity of the API distribution in the sample could also be verified as a possible source of error. To prevent the error, the polymer resin mixtures and the prepared samples were examined for homogeneity as described in the experimental section. In the second part of the chapter, the determination of the diffusion coefficient by curve fitting of diffusion models to measured data was compared. All models used provide an adequate description of the data, especially when considering long measurement times. The diffusion coefficients determined vary merely between $5.05 \cdot 10^{-12} \text{ m}^2/\text{s} \pm 8.91 \cdot 10^{-15} \text{ m}^2/\text{s}$ and $8.56 \cdot 10^{-12} \text{ m}^2/\text{s} \pm 4.23 \cdot 10^{-14} \text{ m}^2/\text{s}$. These deviations can be assumed to be negligible, taking into account possible experimental errors, as demonstrated above. Moreover, it can be seen that a differentiation of the processes into Fickian and non-Fickian diffusion is most likely not reasonable. However, this will be considered again in Chapter 5, with a particular focus on short measurement times. In conclusion, it can be noted that accuracy during the measurement and a precise consideration of the measurement environment have an immense influence on the interpretation of the results. It is also crucial to choose the diffusion model taking into account the measurement errors and the questions addressed in the study. Choosing a more complex model does not always lead to more accurate results, on the contrary, it makes it more difficult to validate and interpret the results.

CHAPTER 5

Development of a 3D Printable Polymer Resin

This chapter contributes to the description and analysis of a new ultraviolet (UV) printable polymer resin for stereolithographic 3D printing (3DP) for application in implants with controlled drug delivery. The cross-linkable oligomer Poly(ethylene glycol) dimethacrylate (PEGDMA) and the hydrogel Poly(2-hydroxyethyl methacrylate) (pHEMA) are combined with a radical photoinitiator (PI). A model drug is incorporated for drug release studies. Mathematical modeling of release profiles is proposed to enhance the prediction of drug release profiles for forthcoming formulations. The chapter is structured as follows. Section 5.1 introduces the overall contributions and reviews related work. Section 5.2 describes the materials used for the development of the resin and outlines the methodology of the experimental setup. Section 5.3 describes the release profile with the help of mathematical formulations as known in the existing literature. Finally, Section 5.5 concludes and puts the results into context. The contributions of this chapter were published in the *Journal of Drug Delivery Science and Technology* [23] and are quoted here verbatim.

5.1 Motivation

Therapeutic treatments are tailored considering the specific pharmacokinetic conditions of each patient in personalized medicines. Important aspects of personalized medical treatment are the choice of a suitable route of administration and an individual dose adjustment. The production of conventional single-dose medicines in large quantities, however, is not able to provide the adequate treatment for patients of all ages, weights, or gender. It is reported that gender differences significantly influence on drug delivery and bioavailability [71, 72]. Females, elderly people, or ill people have a higher risk of being affected by side effects caused by an overdose of standardized medications due to physical differences such as a lower lean body mass compared to men or debilitated hepatic metabolism compared to healthy patients [73, 74].

The drug release of solid unit dosage forms like tablets or capsules leads to a sudden increase in drug concentration in the circulatory system. After the dissolution of a tablet or capsule in a patient's stomach, the dosage flushes into the blood circuit almost at once. In some cases, release characteristics of solid dosage forms are modified to overcome this problem, such as in multi-unit pellet systems or enteric coatings [75–77]. Since oral administration often causes side effects such as complaints in the gastrointestinal tract and cardiovascular system of a patient, parenteral administrations are advisable for elderly patients. Treatments that are both personalized but independent of outpatient or inpatient treatment are still rare. Hence, inventions in the field of personalized medicine are urgently needed. Solutions for individualized medicines, like tablets or implants, are increasingly being sought in the field of 3DP technologies [78–81].

This chapter focuses on subcutaneous administration by personalized drug-loaded implants. Drug substances embedded in these implants are released into the patient's bloodstream by diffusion. In the best case, drug concentrations in the patient's circulatory system remain almost stable, thus leading to a better tolerance of the drug. To ensure the highest possible flexibility in shape and size, a 3D technology is intended for implant fabrication. Therefore, requirements on the photopolymer resin are matched to the use in the laser 3DP method Multi Laser Volume Stereolithography (MLVS) (cf. Section 2.4.3). Besides, polymer samples with uniform shapes and sizes are prepared by using a standardized mold to guarantee the

uniformity of samples for drug diffusion testing. Examined resins mainly consist of cross-linkable functional polymers. In general, functional polymers are of huge interest for drug release products due to their combinatorial and mechanical properties [82–84]. pHEMA, as well as Poly(ethylene glycol) (PEG), are widely used in pharmaceutical and medical applications due to their non-toxicity [6, 85]. pHEMA, for example, is commonly used in contact lenses or implants [86, 87], and its swelling capacity qualifies it for diffusion controlled release applications. The drug delivery qualities of pHEMA hydrogels were analyzed by Paradiso et al. in 2013 [88] demonstrating release over several days. Wang et al. showed in 2016 [82] that diffusion controlled drug release can be realized by 3D printed polymeric tablets. In contrast to conventional photopolymer resins, the formulation by Wang et al. exclusively uses polymers and oligomers without including monomers, which reduces the risk of reactive residues in the dosage form. Release characteristics have been modulated by varying the percentage of cross-linkable oligomers (PEG diacrylate) to non-linkable polymers (PEG).

In this chapter, photopolymer resins containing the cross-linkable oligomer PEGDMA, the hydrogelic polymer pHEMA, a PI for UV polymerization, and a model drug are prepared, polymerized, and compared by their drug release properties. To provide a better comprehension of the release mechanism, a mathematical description and a numerical approximation based on the experimental data are presented. The findings described in this chapter show the huge impact of the oligomer's chain length on the modulation of release profiles. Moreover, release profile modulation by a swelling polymer integrated into the polymer matrix is shown. The benefit of a resin formulation without monomers is its lower toxicological risk. The blend of cross-linkers and polymers provides reliable control over the emerging structure of the polymer matrix as well as great combinatorial flexibility for release modulation.

5.2 Materials and Methods

5.2.1 Materials

pHEMA (Cas No. 25249-16-5) with a molecular weight of $20.000 \text{ g mol}^{-1}$ was acquired from abcr GmbH Germany. PEGDMA (Cas No. 25852-47-5) with a molecular

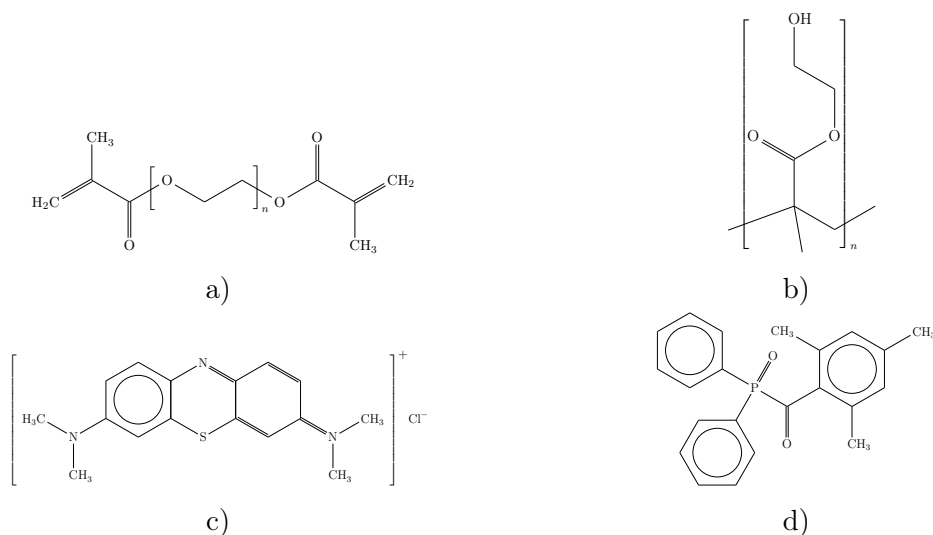


Figure 5.1: a) PEGDMA, b) pHEMA, c) methylene blue (MB) hydrate, and d) TPO

weight of 550 g mol^{-1} and 750 g mol^{-1} as well as the photoinitiator Diphenyl (2,4,6-trimethylbenzoyl) phosphine oxide (TPO) (Cas No. 75980-60-8) were ordered from Sigma Aldrich. TPO is a UV initiator with an absorption peak at 370 nm. TPO and pHEMA were used as received. Inhibitor (MEHQ) included in PEGDMA was removed with aluminum oxide (inhibitor removers) (MDL No. MFCD00081548) purchased from Sigma Aldrich before usage.

The MB (Cas NO. 122965-43-9) is a dark powder and was acquired from Sigma Aldrich. Its anhydrous basis has an average molecular weight of $319.85 \text{ g mol}^{-1}$ and a solubility in water of 40 g/l at 20°C . The molecular weight of the hydrated MB was determined by thermogravimetric analysis (TGA)¹ and is 350.1 g mol^{-1} . The spectral absorption of MB has a maximum at 668 nm. In this current study MB was used as a model drug.

5.2.2 Sample Preparation

Resin mixtures were prepared in amounts of about 2g each in order to achieve at least eight molded samples à 0.2g. Percentages of all components are listed in Ta-

¹TGA is a method for the analysis of a samples mass, mesured while the temperature is changed over time.

Table 5.1: List of weight portions of chemical components in resin mixtures

Resin Version	PEGDMA [wt%]	PHEMA [wt%]	WATER [wt%]	MB [wt%]	TPO [wt%]
S_0/L_0	79.05/83.8	-	19.76/15.05	0,21/0.15	1
$S_{1.51}/L_{1.51}$	82.35	1.51	15.08	0.15	1
$S_{1.94}/L_{1.94}$	77,67	1.94	19.42	0.19	1

ble 5.1. Resin versions are referred to as S_0/L_0 , $S_{1.51}/L_{1.51}$ and $S_{1.94}/L_{1.94}$. The letters S (short) and L (long) indicate the use of PEGDMA 550 or PEGDMA 750 respectively. The numbers 0 and 1.51 or 1.94 indicate the amount of pHEMA included in the resin version. pHEMA free resins (0 wt%) and resins with two different amounts of pHEMA (1.51 wt% and 1.94 wt%) were prepared. Pre-studies showed that a pHEMA proportion of more than 2 wt% leads to unstable and fragile samples.

Before the sample preparation, the inhibitor is removed from PEGDMA 550 and PEGDMA 750 by using inhibitor removers. Each mixture is processed under yellow light and at room temperature. Distilled water and pHEMA are weighed first and filled in a brown glass vile. PEGDMA, MB and TPO are added one after another. Mixtures were stirred for 24 hours.

Cell culture chambers from Sarstedt (8-well on glass detachable) with a volume of 0.5 mL per well were used as molds. The wells are rectangular of 12 mm in width and 9.5 mm in depth. The resulting cuboidal samples are slightly smaller due to polymer shrinkage and evaporation of water while drying. The height of the resulting samples was $2 \text{ mm} \pm 0.02 \text{ mm}$. Due to adhesion between the resin and the cell chamber walls, which are made from polystyrol, the outermost edges of the samples varied in thickness up to a maximum of $2.5 \text{ mm} \pm 0.02 \text{ mm}$. Each cell chamber was filled with resin up to a weight of 0.2 g, placed under a 405 nm laser light source, and was irradiated with an intensity of 0.5 mW mm^{-2} for 3 min. Subsequently, samples were dried for a minimum of 12 h at 40°C until the dry weight was reached.

5.2.3 Microscopy

An Axioskop 5 polarization microscope from ZEISS was used to observe the samples' surfaces as well as the interior. Therefore, the microscope was used in bright-field mode with a magnification of factor 10. In order to detect any possible crystallization, the samples' interior was randomly examined for isotropic structures with the help of a rotating polarization filter.

5.2.4 Fourier-Transform Infrared Spectroscopy

The photopolymerization process must proceed completely to minimize the final implant's possible toxicity. It was assumed that in case of a complete reaction, the characteristic bonds observed by fourier-transform infrared (FTIR) spectroscopy should have vanished entirely. The vibrations of the characteristic bonds of PEGDMA were examined by an INVENIO S FTIR spectrometer from Bruker. Liquid PEGDMA without further additions was measured as a reference first. Thereafter PEGDMA, water and PI were mixed in proportions of 84.5 wt%, 14.5 wt% and 1 wt%, respectively. Photopolymerization was performed as described in Section 5.2.2.

5.2.5 Drug Release Testing

Drug release testing was performed with an AT 7smart (SOTAX AG) dissolution tester. Vessels of the apparatus were equipped with paddles and filled with 500 mL of the dissolution medium. Since the samples are intended for parenteral administration, a buffered solution of pH 7.4 was prepared. Measurements were processed at 37 °C with 70 rpm. The analysis of spectral absorption was performed with an UV-Vis spectrometer (Spectrostar Nano from BMG LABTECH). The MB concentration was correlated to spectral absorption values beforehand by absorption measurements of a dilution series at 664 nm.

Samples for release testing were prepared the day before and dried overnight for at least 12 h. A series of five equal samples of each resin mixture was measured at once. The medium extraction from the vessels of 1 mL was followed by a refill of 1 mL of buffer solution. During the first hour of release testing, the medium was extracted and spectrally measured every 5 min. During the following seven hours, the sample

was taken every 20 min. In the next two days, the sample was taken four times a day.

5.3 Mathematical Modeling of Drug Release

Several mathematical descriptions of drug release from polymer samples have been reported in literature [7, 69, 89–92]. The release from a thin film whose surface is many times larger than its thickness is described frequently. However, several models can also be applied to other, more complex geometries. The same applies to the examination of the different release mechanisms. Some approaches are limited to Fickian diffusion [7] or include relaxation controlled (also referred to as Case-II) transport [93]. Two approaches, including diffusion and relaxation controlled release mechanisms, are pursued within this chapter, as explained in more detail below. The results of the mathematical analysis are reported in Section 5.4.4.

5.3.1 Empirical Approach

The drug diffusion from a polymer matrix can be described by the use of the following equation introduced by Korsmeyer and Peppas [94]:

$$\frac{\Delta M_r}{\Delta M_\infty} = k \cdot t^n \quad (5.1)$$

where ΔM_r and ΔM_∞ are related to the proportion of drug release and refer to the mass of drug released at a certain time t and the amount of drug released in total ($t = \infty$), respectively. The kinetic constant is k and n is the diffusion exponent. Equation 5.1 provides a description of the drug release during the first 60 % of release ($\frac{\Delta M_r}{\Delta M_\infty} < 0.6$) in low swelling polymers (equilibrium water content $\leq 25\%$) [69]. Depending on the shape of the sample and the predominating release mechanism, Ritger and Peppas provide a solution for the classification of the diffusion exponent n , which is well reported in [89] and [95]. Considering a thin film sample, n is 0.5 in case of pure Fickian diffusion, it ranges between 0.5 to 1 in case of non-Fickian transport, and for zero-order release, it is equal to 1. If the specific diffusion coefficient D and the half thickness l of the sample are known, the constant k can be calculated by the Equation 5.2:

$$k = 4\sqrt{\frac{D}{\pi \cdot (2 \cdot l)^2}} \quad (5.2)$$

k and n can be estimated from the experimental release data by the use of Equation 5.1. A modification of Equation 5.1 for the consideration of the burst-effect is proposed by Torres-Lugo and Peppas [96].

$$\frac{\Delta M_r}{\Delta M_\infty} = a + (k \cdot t^n) \quad (5.3)$$

The burst-effect refers to the varying offset a of the release curves, which is caused by the instantaneous dissolution of active pharmaceutical ingredient (API) adhering to the sample's surface. Experimental data are analyzed by Equation 5.3 and the findings are described in Section 5.4.4.

5.3.2 Theoretical Approach

A description of Fickian and non-Fickian diffusion is given in Equation (5.4),

$$\frac{\Delta M_r}{\Delta M_\infty} = 1 - \frac{8}{\pi} \sum_{m=0}^{\infty} \frac{1}{(2 \cdot m + 1)^2} \cdot e^{-\frac{D \cdot t \cdot \pi^2 \cdot (2 \cdot m + 1)^2}{L^2}} \quad (5.4)$$

where ΔM_r is the amount of drug that has been released from the sample at a certain time (t) and ΔM_∞ is the amount of drug that was released in total. The diffusion coefficient D and the thickness of the sheet L are declared to be constant. However, if the polymer systems include both a diffusion controlled and a relaxation controlled release mechanism, Equation 5.4 is deficient. By the additional term for long time release, Equation 5.5 provides a mathematical description for diffusion and relaxation controlled release from spheres [91, 92].

$$\frac{\Delta M_r}{\Delta M_\infty} = \phi_F \left[1 - \frac{6}{\pi^2} \sum_{m=1}^{\infty} \frac{1}{m^2} \cdot e^{-\frac{4 \cdot m^2 \cdot \pi^2 \cdot D \cdot t}{d^2}} \right] + \phi_R \left[1 - e^{-k_R \cdot t} \right] \quad (5.5)$$

The term on the right side in Equation (5.5) refers to the non-Fickian or relaxation controlled portion of the polymer matrix. ϕ_R and ϕ_F indicate the fractions of Fickian and non-Fickian release, respectively. k_R is defined as the relaxation constant and d as the sphere's diameter. Subsequently, Torres-Lugo and Peppas described a

variation of Equation 5.5 for flat polymer samples with a height of 0.8 mm [96] which is given as follows²:

$$\frac{\Delta M_r}{\Delta M_\infty} = \phi_F \left[1 - \sum_{m=1}^{\infty} \frac{8}{(2 \cdot m + 1) \cdot \pi^2} \cdot e^{\frac{-D \cdot (2 \cdot m + 1)^2 \cdot t}{4 \cdot l^2}} \right] + \phi_R \left[1 - e^{-k_R \cdot t} \right] \quad (5.6)$$

where l is the half thickness of the sample. Within this chapter, the approach of Torres and Peppas is followed for mathematical modeling.

Note Equation (5.6) exhibits critical errors: First, the term $(2m + 1)$ in the summand is not squared, although the correct form of the series solution includes $(2m + 1)^2$. Second, the exponent lacks of π^2 , which is required for an accurate representation of diffusion-related decay rates. Third, the summation starts at $m = 1$ rather than $m = 0$, thereby omitting the fundamental first mode term $(2m + 1) = 1$. Finally, the Fourier series coefficients must cancel correctly to ensure proper normalization.

To highlight the differences to Equation (5.6), the correct formula (3.33) is given here once again:

$$\frac{\Delta M_r}{\Delta M_\infty} = \phi_F \left[1 - \sum_{n=0}^{\infty} \frac{8}{(2 \cdot n + 1)^2 \cdot \pi^2} \cdot e^{\frac{-D \cdot (2 \cdot n + 1)^2 \cdot \pi^2 \cdot t}{4 \cdot l^2}} \right] + \phi_R \left[1 - e^{-k_R \cdot t} \right]$$

5.4 Results and Discussion

The samples' appearance was examined by microscopy and FTIR spectroscopy. The drug release testing of a total of 6 batches à five samples was performed, followed by the mathematical description of the results.

²Equation 5.6 was adopted, following earlier studies, to facilitate comparison across works. Future research should employ the correct formula, Equation 3.33.

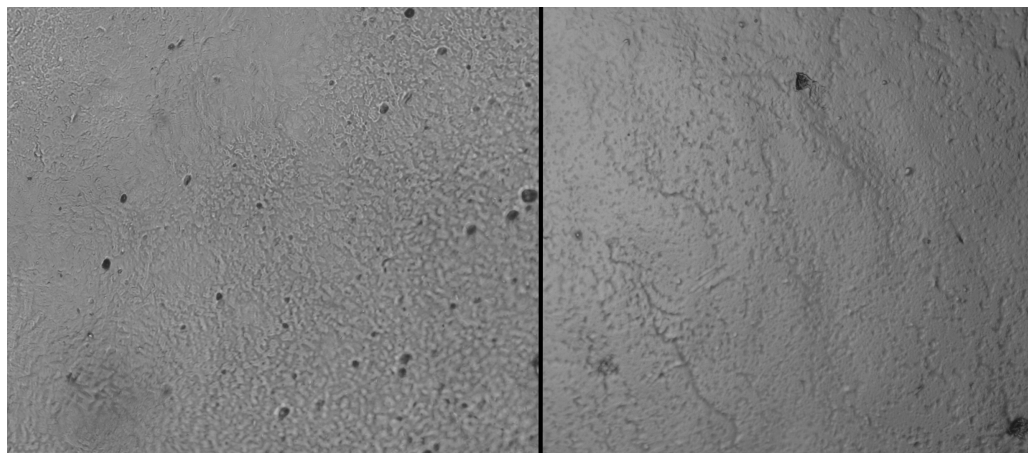


Figure 5.2: Microscopic pictures of a $L_{1.51}$ sample before (left side) and after (right side) release experiments with a magnification of factor 10.

5.4.1 Microscopy

By pre- and post-examination of visible damages, such as cracks, the comparability of the results could be ensured. As shown in Figure 5.2, the surface was still intact and showed only furrows of shallow depth. Additionally, the physical state of MB after polymerization and during release testing was verified by polarization microscopy to be not crystalline.

5.4.2 Fourier-Transform Infrared Spectroscopy

The absence of reactive groups of PEGDMA remaining after polymerization was certified by FTIR spectroscopy as described in section 5.2.4. Figure 5.3 shows the IR spectrum of liquid non-polymerized PEGDMA in comparison with photopolymerized PEGDMA. It can be seen that the absorption peaks at 815 cm^{-1} and 1636 cm^{-1} caused by the vibrations of the $\text{CH}=\text{CH}_2$ double bond are clearly visible for the uncured PEGDMA. These peaks disappeared accordingly after polymerization. Due to the saturation of the α, β -unsaturated carbonyl group during the polymerization reaction, the peak at 1715 cm^{-1} shifted to 1724 cm^{-1} . This shift to a higher wavelength indicates that the bond order after cross-linking has increased. Thus, a transformation of the reactive groups can be assumed [97–101].

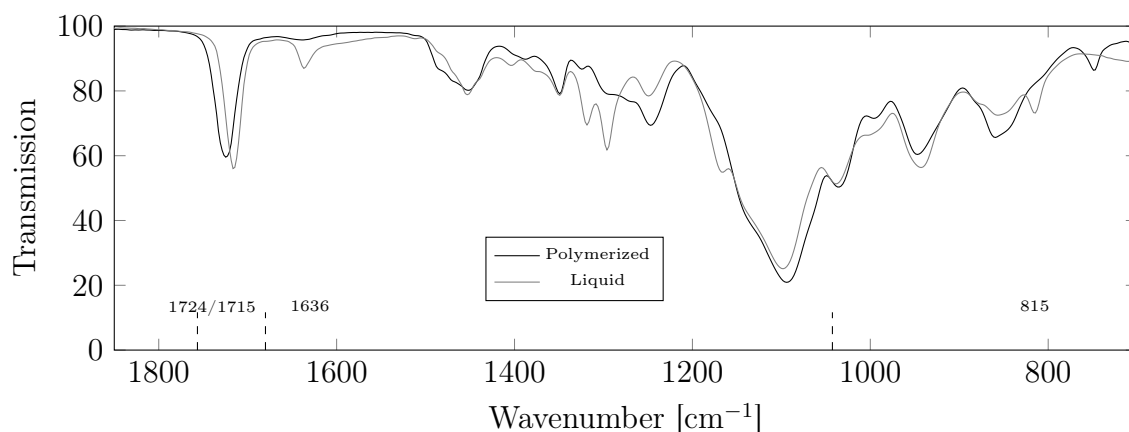


Figure 5.3: FT-IR spectra of PEGDMA in liquid condition (gray line) and PEGDMA photopolymerized with 1 wt% TPO (black line).

5.4.3 Drug Release

The release of MB from moulded samples S_0 , $S_{1.51}$, $S_{1.94}$ and L_0 , $L_{1.51}$, $L_{1.94}$ over a time period of 32 h is reported in Figure 5.5. MB concentration, plotted on the ordinate, is given by the amount of released MB in relation to the total amount of MB initially contained in the sample. Those samples consisting of PEGDMA 550 (S-samples) are plotted on the left side, and those of PEGDMA 750 (L-samples) on the right. During the first hours of release, MB concentration from S-samples increased slower compared to L-samples (Figure 5.5). Especially during the first hour of release, L-curves show a higher gradient. The percentage of MB released during a time interval of one hour and eight hours is illustrated in Figure 5.4. Comparing the drug release of S- and L-samples during the first hours clearly demonstrates that an increasing amount of pHEMA results in a contrary tendency. Whereas the MB release of S_0 is about 12%, L_0 releases almost 40% of its MB content during the first hour. The difference between S_0 and L_0 is even increasing after a time period of 8 h where the released amount is 44% and 86% respectively. Regarding the pHEMA containing samples, the difference between $S_{1.51}$ and $L_{1.51}$ after 1 h and 8 h remains virtually the same. This also applies to $S_{1.94}$ and $L_{1.94}$.

Figure 5.5 and Figure 5.4 show a distinct influence of the polymer chain length on the release profile. Apparently, MB diffusion is decelerated in S-samples com-

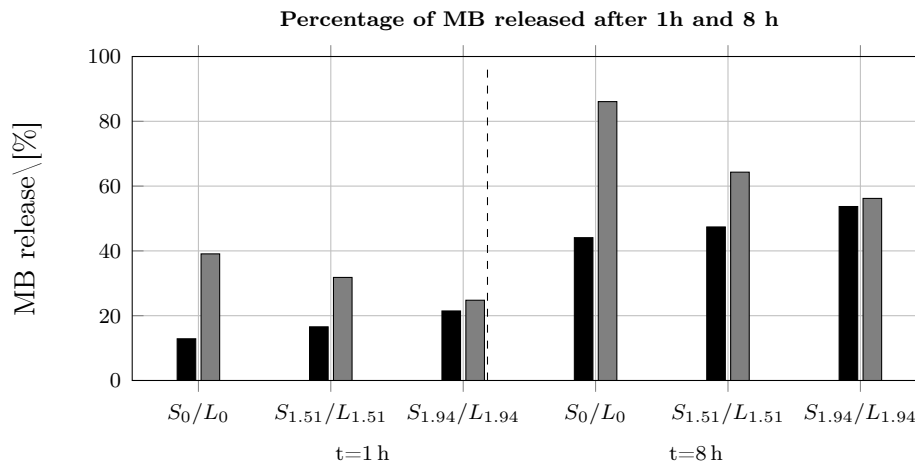


Figure 5.4: Comparison of the percentage of MB released from samples shown in Figure 5.5 at different time points (left side 1 h, right side 8 h). S-samples are indicated in black, L-samples in grey.

pared to L-samples. With regard to the chain length of 9 chain units on average in PEGDMA 550 and 13 units in PEGDMA 750 and assuming that MB molecules are homogeneously embedded into the samples polymer matrices, a faster diffusion from a bigger mesh size is reasonable. In the case of a mono-polymer sample, the mesh size of the resulting polymer matrix is decisively determined by the polymer chain length. Interestingly, by adding pHEMA into the resin mixture, S-samples show an accelerated release, whereas release is decelerated in L-samples. A higher gradient of $S_{1.94}$ in comparison with the $S_{1.51}$ and S_0 curve remains during the entire time period.

The total amount released increases with ascending pHEMA content. The expansion or even rupture of the polymer matrix by swelling pHEMA polymers could be a reason for this phenomenon. A contrary trend can be seen with regard to the L-curves. While S-samples show faster drug release, L-samples display a decelerated drug release with increasing pHEMA content. During the first eight hours of release, the gradients of the $L_{1.51}$ curve and $L_{1.94}$ curve show a reduction with regards to L_0 . However, regarding the MB concentration at $t=32$ h, this is accompanied by a decrease in the overall drug release values. While L_0 releases more than 95% of its MB content, $L_{1.51}$ releases 70% and $L_{1.94}$ only 60% of MB during the whole release

Table 5.2: Tabular of the kinetic constant k and the diffusional exponent n calculated by Equation 5.3 and the diffusion coefficient D and the kinetic relaxation constant k_R calculated by Equation 5.6. Additionally, the coefficient of determination R^2 is listed to indicate the accuracy of each curve fit.

Sample	Empiric model			Theoretical model		
	$k \text{ s}^{-0.5}$	n	R^2	$D \frac{\text{m}^2}{\text{s}} \cdot 10^{-10}$	$k_R \cdot 10^{-10} \text{ s}$	Φ_R
S_0	$1.33 \cdot 10^{-7}$	0.7015	0.9955	1.46 ± 0.03	5.5 ± 0.1	44 ± 2
$S_{1.51}$	$2.17 \cdot 10^{-7}$	0.6328	0.9945	1.59 ± 0.07	0.5 ± 0.2	5 ± 2
$S_{1.94}$	$1.84 \cdot 10^{-7}$	0.6638	0.9934	2.4 ± 0.2	0.7 ± 0.2	5 ± 4
L_0	$1.63 \cdot 10^{-7}$	0.7551	0.9825	6.8 ± 0.4	1.7 ± 0.3	11 ± 3
$L_{1.51}$	$1.96 \cdot 10^{-7}$	0.7149	0.9635	38 ± 32	5 ± 3	47 ± 22
$L_{1.94}$	$1.91 \cdot 10^{-7}$	0.7380	0.9780	5.7 ± 0.1	0.2 ± 0.4	1.8 ± 0.7

period.

The overall shape of the release curves is not significantly influenced by the addition of pHEMA. While S-samples maintain a constant growth, L-curves show a flattening in the curve progression starting between the 8th and 21st hour. Analyzing the total release of MB, Figure 5.5 reveals an earlier time point for release stagnation of L-samples than of S-samples.

5.4.4 Mathematical Data Analysis

Principles of drug release profile modeling were explained in Section 5.3. In the following, the parameters of these models are determined based on the measured data. In Equation 5.3, a straightforward approach for the description of the first hours of release was found. However, this is restricted as it only applies to release values below $\frac{\Delta M_r}{\Delta M_\infty} = 0.6$. In other words, the long-time release cannot be modeled with this approach.

Since the polymerized PEGDMA is very low swelling and the content of pHEMA does not exceed 2%, the overall degree of swelling is assumed to be below 25% [102, 103]. This makes Equation 5.3 only applicable for the comparison of API release during the first hours. The resulting values for the kinetic constant k and the diffusional exponent n are listed in Table 5.2 on the left side. The coefficient of determination

R^2 is also given to indicate the accuracy of each curve fit.

The determination of the variables can be expressed as a least squares curve fitting problem. A concrete solution to this minimization problem is given by the Levenberg-Marquardt algorithm. The numerical computations are implemented with the help of the SciPy package by the use of the `curve_fit` function [104]. This function implements the Levenberg-Marquardt algorithm to fit the parameters of a given formula based on measured data. The corresponding R^2 values are determined with the NumPy package [105].

The resulting diffusional exponents n range between 0.63 and 0.75, which, according to [89], indicates a predominating non-Fickian release mechanism in the first hours of release. The n values of L-samples are slightly higher than those of S-samples, indicating a higher fraction of relaxation controlled release. Moreover, both S- and L-samples show lower n values with increasing pHEMA content. Since the swelling of pHEMA is expected to increase over time and the calculation of n values does involve different amounts of time for each sample, a direct comparison is not advisable. When comparing the kinetic constants of S-samples, it can be seen that the highest k value is calculated for S_0 , followed by $S_{1.94}$ and then $S_{1.51}$. Likewise, this order appears for L-samples. These results underline the influence of pHEMA on the release characteristics.

As shown in Figure 5.4, 60 % of release is reached much earlier with L-samples than with S-samples. This is attributable to the difference in oligomer chain length.

A second approach is given in Section 5.3, which is referred to as the theoretical approach. It combines the terms of diffusion controlled release and relaxation controlled release mechanism. As described in [96], the relaxation constant k_R and the fraction of non-Fickian release ϕ_R are calculated in the first step and the diffusion coefficient D in the second step. Taking the results from Equation 5.3 and assuming a dominance of the non-Fickian part, this is assumed to apply to the release over long times. In this case, the first part of Equation 5.6 is set to zero for the calculation. The time threshold for long-time release was set at 8 h. This leads to a consideration of the last nine measurements per sample.

In contrast to [96] and [92] k_R and ϕ_R are determined by the use of a curve fitting function. It has been ascertained during this project that this procedure has a higher reproducibility due to a minimization of subjective criteria. The details of the pro-

cedure are already described earlier in this section with regard to Equation 5.3. The resulting k_R values for all samples are listed in Table 5.2 on the right side. ϕ_R is later used to calculate ϕ_F which is $1 - \phi_R$.

With the help of k_R und ϕ_R , it is possible to estimate the diffusion coefficient D from Equation 5.6. The diffusion coefficient, as well as the accuracy of the curve fit, R^2 , are listed in Table 5.2. R^2 indicated the accuracy of the entire curve fit from 0 h to 56 h. As it can be seen in Figure 5.6, Equation 5.6 allows adequate modeling of the entire release profile. Therefore, it can be assumed that in time intervals in which no measured data exists, the curve progression is still traced with high accuracy.

For detailed considerations on the use of different models, see Chapter 4. Conclusions on clear Fickian and non-Fickian diffusion should be interpreted with appropriate caution.

5.5 Conclusion

This chapter's focus is the investigations of 3D printable photopolymer resins, consisting of a homogeneous mixture of a swelling polymer, cross-linking oligomers, a PI, water, and a model drug. By photopolymerization, a solid drug-embedded polymer matrix is formed. With regard to new solutions for controlled drug release implants, two polymers, PEGDMA and pHEMA, are tested. Drug release properties of PEGDMA with a molecular weight of 550 g mol^{-1} and 750 g mol^{-1} showed that the polymer chain length has a decisive impact on the drug dissolution profile. The addition of the swelling polymer pHEMA into the polymer matrix is intended to approach a modulation of these release profiles toward a zero-order release. Results showed a contrary influence of pHEMA to PEGDMA 550 and PEGDMA 750. Whereas the swelling polymer influenced a faster drug delivery in PEGDMA 550, it caused a decelerated drug release in PEGDMA 750. Therefore, an influence on the release profile could be clearly proven.

In the next step, investigations on the release profiles by the application of mathematical models are presented. Diffusion exponents are calculated with the help of Equation 5.1. The resulting n values indicate a predominantly non-Fickian release mechanism. As this approach does not allow for a complete description of the drug

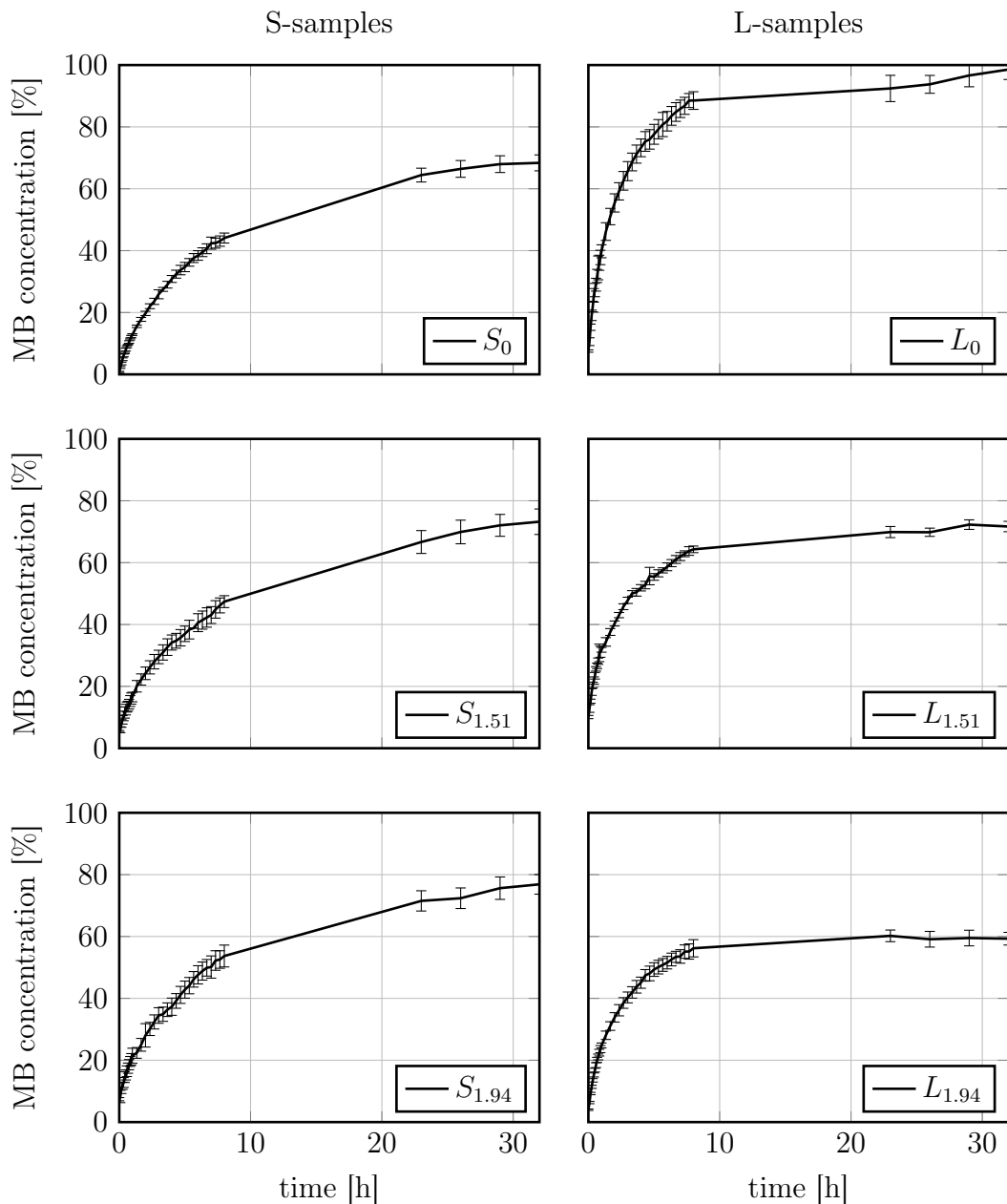


Figure 5.5: Release of methylene blue from S-samples and L-samples during 0 h to 8 h and 23 h to 32 h in percentage. The standard deviation is indicated by error bars at measurement position.

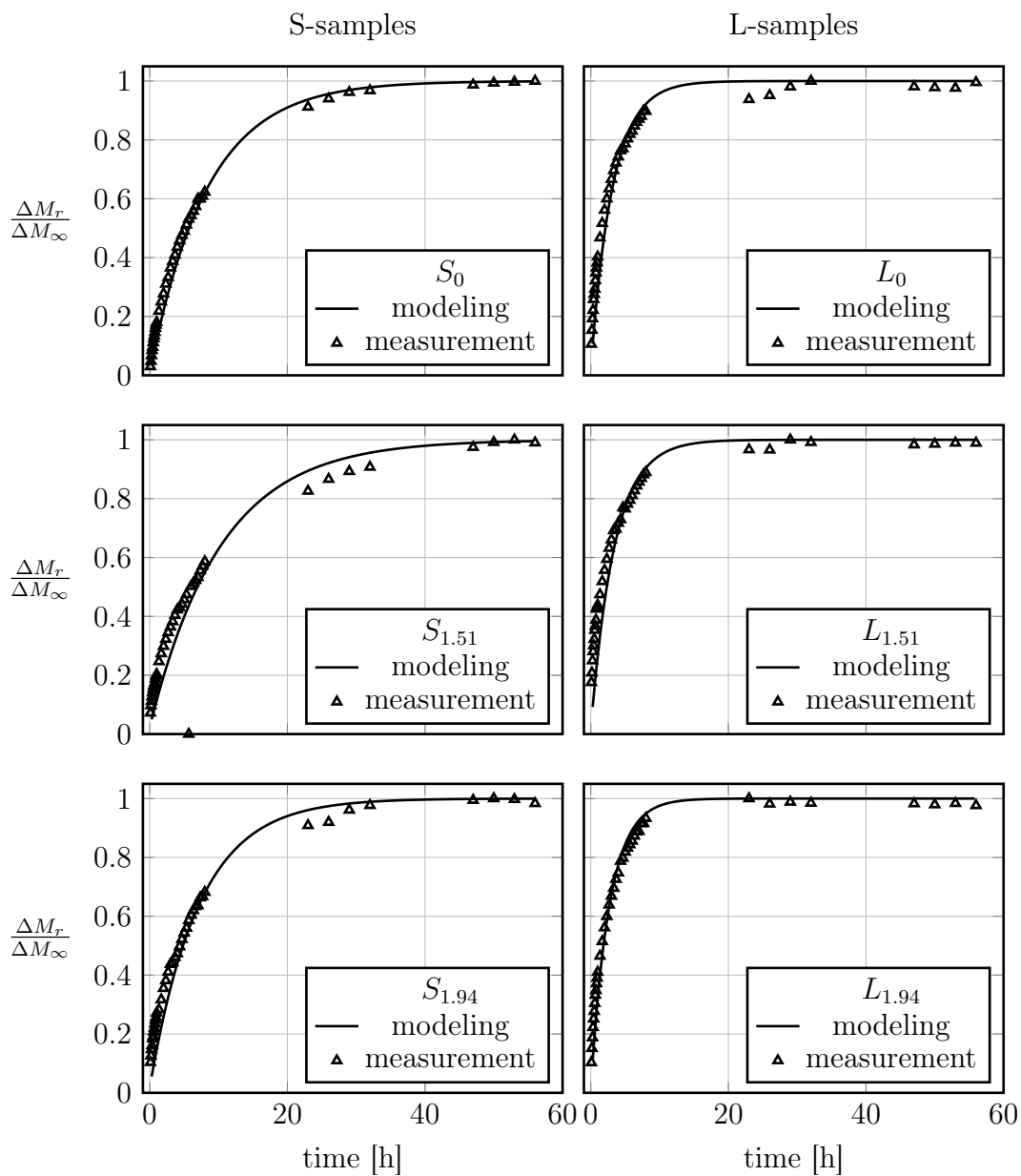


Figure 5.6: Comparison of $\frac{\Delta M_r}{\Delta M_\infty}$ values resulting from Equation 5.6 and measured values showing a proper modeling of release profiles. Calculated variables and R^2 values are listed in Table 5.2

release curves, a more complex approach was applied with 5.6. These efforts resulted in the modeling of dissolution profiles with high accuracy. The diffusion coefficient, as well as the relaxation constant, provide a baseline for the planning and benchmarking of prospective experiments. The results of the diffusion coefficients in this chapter are highly reasonable, although concluding on non-Fickian diffusion solely with the help of curve fitting is not tenable due to the data basis. For this reason, only Fickian diffusion is used in the following.

CHAPTER 6

Polymer Network Characterization

3D printed photopolymer resins are investigated concerning the influence of interfacial diffusion resistance on controlled drug release. Within this study, six PEGDMA based resin variants (cf. Chapter 5) differing in oligomer chain length and viscosity are investigated from fabrication to their swelling behavior in a pH-buffered swelling medium.

The differences in the composition of the liquid resins are clearly reflected in their differing viscosity, as the results show. However, the course of the polymerization process remains unaffected by this, whereas the intensity and duration of irradiation have a significant influence on the curing process.

The polymerization process is investigated using rheological measurement during UV irradiation with varying laser intensities. Furtheron, 3D printed polymer resins and resins prepared by molding are compared regarding their temporal mass uptake from water influx, revealing insight into the diffusion resistance of the materials. The results are analyzed using a diffusion model that accounts for directional differences from interfacial diffusion resistances.

The results show the considerably smaller resistance of the bulk material in comparison to the resistance of the interfaces between the layers. Furthermore, the polymer

mesh size in equilibrium swollen state of 3D printed and moulded resins reflects the structural change due to the layering process. This additional degree of freedom in design, offered by layered structures, decouples the release rate from the sample volume. These findings provide opportunities to personalized drug-containing polymers for customized drug release.

The author declares that the following chapter includes verbatim quotes from [106]

6.1 Motivation

For several decades, researchers have been examining the potentials of polymers for applications in pharmaceuticals, such as tablet coatings or swelling agents, but also for solid dosage forms or implants. Personalized medicine, and in particular dosage forms with diffusion controlled drug release, are increasingly attaining significance in the pharmaceutical industry. This offers opportunities, especially for older and high-risk patients. Additive manufacturing enables the production of small quantities of individualized dosage forms. However, in order to manufacture pharmaceutical products at a high personalizable level [20], a good knowledge of the influence of the manufacturing process on the polymer, including its network structure and release properties, is crucial. The stereolithography (SLA) is a widely used additive manufacturing technology based on a laser-induced polymerization process using liquid UV curable polymer resins, as described in Chapter 2. Similar to other 3D printing technologies, three-dimensional objects are created layer by layer, but SLA is completely free of heating or mechanical forces. This prevents the undesired decomposition of the active ingredients by high temperatures. The polymerization in SLA is mostly a photo induced free-radical reaction. The process is initiated by the cleavage of the photoinitiator (PI) substance when irradiated with light of a suitable wavelength, followed by the binding with a nearby reaction partner, a monomer or oligomer. This propagation step continues until no more reactants are available or the reaction terminates ¹. [16, 31, 107]. However, how exactly this rather simple process evolves depends on a variety of parameters related to the material composition, in addition to the fabrication process. It also depends on the ratio between PIs and

¹Termination may occur, for example when two chains join by decoupling, or when two radicals react.

reactive monomers or oligomer ends. The probability of a reaction partner becoming spatially accessible increases with the diffusion rate. When having high amounts of oligomers in the resin, the number of reactants is decreased compared to pure monomer resins, as there are chain-links that are already polymerized. The initial length of these oligomer chains plays a role in the speed at which the entire process takes place, but also whether they are only reactive on one or both sides. At the end of the reaction, loops, and meshes will have formed, and some oligomers will only have been incorporated into the network on one side and remain hanging around as loose ends. Shimojo et al. [108] demonstrated the impact of non-reacted reactants in cross-linked hyaluronic acid systems on the mechanical properties of the polymer. The diffusion of particles moving through a network is influenced by physical and chemical factors such as the particle size to polymer chains length and resulting mesh size or the interaction between particles, solvent, and polymer [109,110]. Suppose the drug substance is integrated directly into the liquid resin and incorporated into the polymer network during polymerization. In that case, the solubility and/or miscibility of all resin components should be taken into account, as unreactive additives may hinder the reaction of the polymer chains. In particular, the control of individual drug release is a topic of numerous studies [21,22,24,30,111–116].

In this present study, both the polymerization process and the resulting polymer network from molded and 3D printed resins are investigated and compared. Six variants of model drug-containing PEGDMA-based resins, which differ in oligomer length, pHEMA addition, and solvent content, are studied. The polymerization progress of the resins during UV irradiation is investigated. The shortest and longest exposure time that results in a fully cured specimen is determined by varying the radiation intensity (cf. Section 6.3.1). Polymerized in a transparent mold, fully cured polymer resins are compared to 3D printed resins regarding their swelling properties (cf. Section 6.3.2). Network characterization is done by determining the polymer mesh size in an equilibrium swollen state (cf. Section 6.3.4). Furthermore, the amount of water soaked up by the polymers, the time in which it was absorbed, and the water diffusion coefficient were determined (cf. Section 6.3.3). The mass uptake and water diffusion are further analyzed by an anisotropic diffusion model considering interfacial resistance in the polymer sample.

6.2 Materials and Methods

pHEMA (CAS No. 25249-16-5) with approximately $20\,000\text{ g mol}^{-1}$ was purchased from abcr GmbH Germany. The polymer PEGDMA (CAS No. 25852-47-5) with a molecular weight of around 550 g mol^{-1} and 750 g mol^{-1} , as well as the photoinitiator TPO (CAS No. 75980-60-8) and the model drug MB (CAS No. 61-73-4) were ordered from Tokyo Chemical Industry. MB has a comparable particle size to the most common drug particles and is easily detectable via spectroscopy.

Resin	PEGDMA 550	PEGDMA 750	pHEMA	WATER	MB	TPO	η
	/ wt%	/ wt%	/ wt%	/ wt%	/ wt%	/ Pa · s	
S_0	79.05	0	0	19.76	0.21	1	28
S_{15}	82.35	0	1.51	15.08	0.15	1	52
S_{194}	77.67	0	1.94	19.42	0.19	1	58
L_0	0	83.80	0	15.05	0.15	1	65
L_{15}	0	82.35	1.51	15.08	0.15	1	127
L_{194}	0	77.67	1.94	19.42	0.19	1	131

Table 6.1: Resin formulations in weight percent wt% and viscosities η in Pa · s; PEGDMA has Mw of approx. 550 g mol^{-1} in case of S-resins and Mw 750 g mol^{-1} in case of L-resins. Weights listed here correspond to those in Chapter 5, Table 5.1. [106]

All resin variants are prepared by the weights and portions listed in Table 6.1. The letters S or L indicate PEGDMA with a Mw of 550 g mol^{-1} and a Mw of 750 g mol^{-1} , respectively. The pHEMA contents of 0 wt%, 1.51 wt%, or 1.94 wt% are indicated by the subscripts.

The resin preparation is described in detail in Steinbach et al. [23]. In brief: oligomer and water are mixed first, then pHEMA and MB are added. The mixture is stirred for 24h before TPO is added. The prepared resins are handled under yellow light at room temperature conditions to prevent uncontrolled polymerization caused by ambient light. S_0 and L_0 differ in their weight portions, as an equimolar PEGDMA content is considered in order to investigate the influence of the different PEGDMA chain lengths. S-resins and L-resins with 1.51 wt% or 1.94 wt% pHEMA are mixed in equal weight proportions as the influence of the added pHEMA content is of interest here. For swelling experiments, resins are prepared as molded and 3D printed samples. In both cases, a similar cuboid shape is chosen. The actual dimensions are

measured after drying and are 2 mm · 12 mm · 9 mm in case of molded specimens and 1.5 mm · 11.5 mm · 10 mm in case of printed specimens, with an average uncertainty of 0.1 mm in any direction. For 3D printing, a Form 1+ 3D printer from Formlabs Inc. with a vertical resolution of 25 μm is used. A CAD of the sample being printed with equal dimensions as the mold was generated. In each case, six samples were distributed regularly across the printing platform and printed in a single printing process. Cuboid shaped cell culture chambers from Sarstedt AG & Co. KG are used as molds. An amount of 200 mg of resin is pipetted into each chamber and irradiated throughout by an intensity of 3.8 $\mu\text{W}/\text{mm}^2$ of UV radiation for 3 min. An equal laser wavelength of 405 nm is used for the 3D printing and molding process. After polymerization, the specimens are dried in an oven at 40 °C for at least 12 h, and their dry weight is determined using a mg-balance from Kern & Sohn GmbH.

6.2.1 Real-Time Polymerization Analysis

Rheological measurements are conducted using an Anton Paar's MCR 502 Modular Compact Rheometer enhanced with a PP25 plate-plate measurement system with a diameter of 25 mm. The MCR 502 is extended by a custom UV irradiation unit for real-time polymerization measurements. The PP25 ground plate is replaced by a vacuum chamber observation window which serves as a transparent ground plate. A semiconductor laser (wavelength 405 nm) with a condenser lens is directed perpendicular to the window from below. The laser wavelength corresponds to the laser used in 3DP as well as in the molding process. Laser intensities are controlled electronically, and the absolute irradiance at the sample position is measured by a PD300R-UV photodiode sensor purchased from Ophir Optronics Solutions Ltd. In addition, the complex viscosity is monitored versus exposure time. All measurements are carried out in oscillation mode at room temperature and under light enclosure at an angular frequency of 10 rad/s as around this frequency least variance in pre-measurements was detected.

Rheological measurements were performed repeatedly for all resins, covering the entire solidification process from liquid resins to fully solid polymers. Subsequently, the progress of the polymerization of each resin is measured at six intensities (0.6, 1.3, 2.5, 3.8, 12.7 and 44.6 $\mu\text{W}/\text{mm}^2$). The viscosity data are plotted versus the exposure time in a two-dimensional graph, as depicted in Figure 6.1. It exemplifies a typical

measurement of the polymerization process with laser intensities from $0.1 \mu\text{W}/\text{mm}^2$ to $44.6 \mu\text{W}/\text{mm}^2$ within an exposure time of 300 s.

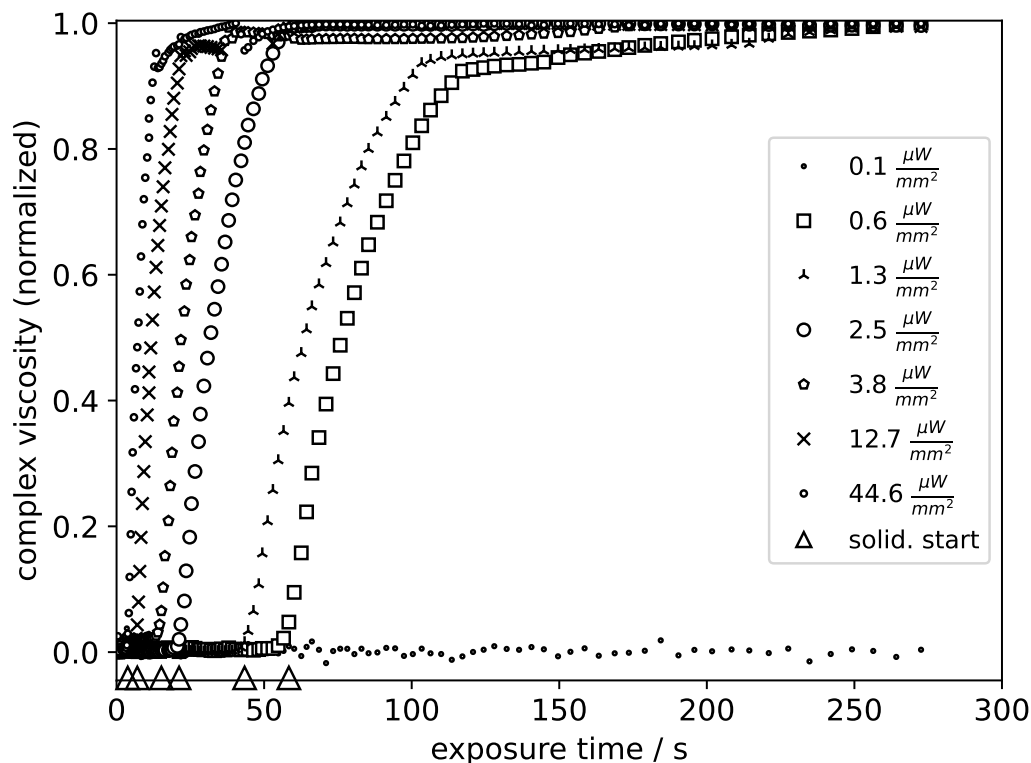


Figure 6.1: Complex viscosity measurements of resin S0 during UV irradiation with intensities between $0.1 \mu\text{W}/\text{mm}^2$ to $44.6 \mu\text{W}/\text{mm}^2$ (complex viscosities are normalized except of intensity $0.1 \mu\text{W}/\text{mm}^2$); solidification start time indicated by triangles on the horizontal axis. [106]

In order to determine the moment when the curves start to increase and the solidification begins, the derivative with respect to the time of each measurement curve is calculated. The solidification start time (SST) is defined by the moment when the derivative rises above a predefined threshold of 0.1 Pa and is indicated on the horizontal axis in Figure 6.1.

The solidification start energy (SSE) can be defined as the SST multiplied by the

laser intensity. Note that SSE is the energy per area that has been applied up to the moment when the viscosity curve starts to rise rather than the actual activation energy.

The time of complete solidification is defined by the moment when the curve turns into a plateau. It is determined by mathematical curve analysis using the temporal derivative of the viscosity data. The time period during which the solidification takes place – the solidification duration (SD) – is, therefore, the period between the SST and the beginning of the plateau.

Finally, the solidification energy (SE) per area is defined as the cumulated energy per area over the whole exposure time until the plateau is reached.

6.2.2 Water Diffusion During Mass Uptake

The mass uptake M is measured over a period of several hours in order to determine the water diffusion rate. Each sample is soaked separately in a 7.4 pH buffer medium at 37°C and is weighed every 10 min in order to monitor the mass uptake M over soak time.

$$M = \frac{m_a - m_{ad}}{m_{ad}} \quad (6.1)$$

The specimen's mass uptake at a given time is calculated as the difference between its current mass m_a and its initial dry mass m_{ad} , normalized by the dry mass, as shown in Equation (6.1).

Subsequently, the diffusion coefficients for water uptake are then determined from the measurement curves. A solution of Fick's second law of diffusion in a rectangular body with anisotropic diffusion coefficients in the cartesian coordinates was presented by Aktas et al. [117]. It is important to distinguish the effects of sample geometry from diffusion anisotropy. For molded samples, the diffusion coefficient can be determined using the isotropic solution given in Equation (6.2) with parameter α . In 3D printed samples, diffusion in the normal and lateral directions is described using Equation (6.2) with parameter β ,

$$M(t) = M_\infty \cdot \left[1 - \frac{512}{\pi^6} \cdot \sum_{p=0}^{\infty} \sum_{q=0}^{\infty} \sum_{r=0}^{\infty} \left(\frac{1}{(2p+1)^2(2q+1)^2(2r+1)^2} \cdot e^{-t \cdot \pi^2 \cdot \Gamma} \right) \right] \quad (6.2)$$

$$\Gamma = \begin{cases} \alpha & \text{for bulk or moulded sample (isotropic)} \\ \beta & \text{for layered sample (anisotropic)} \end{cases}$$

$$\alpha = D_{\text{bulk}} \cdot \left(\frac{(2p+1)^2}{h_x^2} + \frac{(2q+1)^2}{h_y^2} + \frac{(2r+1)^2}{h_z^2} \right) \quad (6.3)$$

$$\beta = D_{\text{normal}} \cdot \frac{(2p+1)^2}{h_x^2} + D_{\text{bulk}} \cdot \left(\frac{(2q+1)^2}{h_y^2} + \frac{(2r+1)^2}{h_z^2} \right) \quad (6.4)$$

where $M(t)$ idenotes the experimental mass uptake, and M_∞ represents the maximum (equilibrium) mass uptake. D_{bulk} and D_{normal} are the diffusion coefficient in the layer or bulk material and the diffusion coefficient in normal direction, respectively. h_x , h_y and h_z are denoted as the sample dimensions in x, y and z direction, as depicted in figure 6.2.

For molded polymers, the bulk material is assumed to be isotropic, implying no directional differences in the diffusion coefficients ($D_{\text{normal}} = D_{\text{bulk}}$). In contrast, for 3D-printed polymers, diffusion along the printing direction (through the layers) may differ from that in the lateral directions. To determine the diffusion coefficient in printing direction D_{normal} it is assumed that $D_{\text{normal}} \neq D_{\text{bulk}}$ and that D_{bulk} is equal to the diffusion coefficient of the moulded sample.

The curve-fitting algorithm is implemented with the python SciPy 1.0 [104] package using the least-squares optimization applying the Levenberg–Marquardt algorithm to solve the optimal parameter solution for a given function. In order to evaluate the accuracy of the resulting fit a bootstrapping algorithm is implemented returning the standard deviation of the fit.

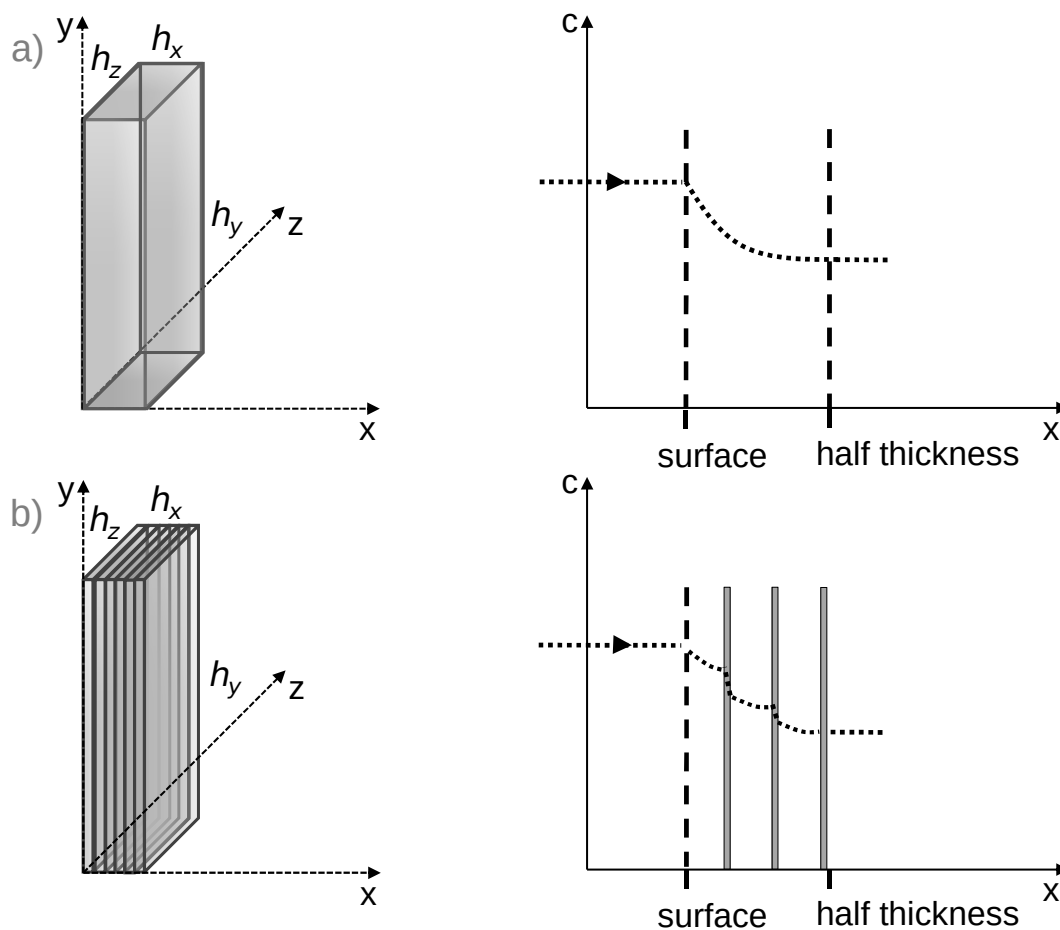


Figure 6.2: left side: schematic illustration of a) moulded and b) 3D printed polymer samples and right side: concentration C of water over distance x between the surface and the center of the sample ($h/2$) at a fix time point during mass uptake assuming a continuous water flux. [106]

Figure 6.2 shows on the left side the orientation of a) moulded and b) 3D printed specimens in a three-dimensional graph. On the right side, a schematic illustration of the diffusion profile is depicted. The outer surfaces (between polymer and water) are neglected. In the 3D printed specimen, a step concentration drop at the inner interfaces is anticipated, which is attributed to a significant change in the diffusion

resistance. Due to symmetry condition concerning the sample geometry the interface in the middle of the sample (at $h/2$) is not considered.

Assuming that the diffusion resistance of all the interfaces is identical, the effective diffusional resistance R_{eff}^D of the system is equal to the sum of each individual interfacial resistances $R_{\text{interface}}^D$ and layer resistances R_{layer}^D , as described by Equation 6.5.

$$R_{\text{eff}}^D = \sum_{n=0}^m R_{\text{layer}}^D + \sum_{n=0}^{m-1} R_{\text{interface}}^D \quad (6.5)$$

The number of interfaces within the half sample height is indicated as $m - 1$ whereas the number of layers is m .

In the following, the procedure for the calculation of the interfacial diffusion resistance is outlined:

1. The bulk diffusion coefficient D_{bulk} is determined from moulded samples by Equation (6.2) and (6.3) where $D_{\text{normal}} = D_{\text{bulk}}$.
2. The diffusion coefficient in normal direction D_{normal} is determined from printed samples by Equation (6.2) and (6.4) where $D_{\text{normal}} \neq D_{\text{bulk}}$ using D_{bulk} from 1.
3. R_{eff}^D is calculated from D_{normal} and R_{layer}^D is calculated from D_{bulk} by Equation (6.6) and (6.7).
4. Subsequently, $R_{\text{interface}}^D$ is calculated from Equation (6.8).

R_{eff}^D is the effective diffusion resistance of the whole printed sample, whereas R_{layer}^D is the hypothetical diffusion resistance of a layer assuming the layers to have the same diffusion resistivity as the moulded sample. The effective diffusion resistance R_{eff}^D , the resistance of the interface $R_{\text{interface}}^D$ as well as the resistance of layers R_{layer}^D can be estimated from Equations (6.5)–(6.7),

$$R_{\text{eff}}^D = \left[\frac{D_{\text{normal}}}{\frac{h_x}{2}} \right]^{-1} \quad (6.6)$$

$$R_{\text{layer}}^D = \left[\frac{D_{\text{bulk}}}{d_{\text{layer}}} \right]^{-1} \quad (6.7)$$

whereas $\frac{h_x}{2}$ denote the half height of the printed sample and d_{layer} the thickness of a single layer.

Consequently, the diffusion resistance of a single interface can be calculated by Equation (6.8).

$$R_{\text{interface}}^D = \frac{h_x \cdot d_{\text{layer}}}{h_x - 2 \cdot d_{\text{layer}}} \cdot \left(\frac{1}{D_{\text{normal}}} - \frac{1}{D_{\text{bulk}}} \right) \quad (6.8)$$

The layer thickness is considered to be constant and its variation during swelling is neglected. Since the thickness of the interface is small compared to the layer thickness, only the resistance of this interface is determined. The interfacial diffusion resistance is estimated using the experimental data obtained from mass uptake experiments in order to demonstrate the huge impact of additional interfaces in a laminate system.

6.2.3 Average Polymer Mesh Size

Equilibrium swelling experiments were used to determine the average polymer mesh size of both molded and 3D printed resins. Each sample is immersed in a pH-buffered medium at 37.4 °C and allowed to swell until reaching equilibrium weight.

Richbourg et al. [118] proposed an approach to calculate the mesh size of a highly cross-linked polymer network from the molecular weight between two cross-links. It is based on the Flory-Rehner swelling theory and considers the changed mobility of strongly cross-linked chains in contrast to pure monomer chains. According to Richbourg et al., the model also holds for highly cross-linked polymers, as investigated in our study.

Obviously, the calculation of the average mesh size is theoretical, and the calculations do not allow conclusions regarding the actual shape or size distribution of the meshes; however, it gives a good estimate for comparative studies. The approach of Richbourg et al. is therefore used as follows: The volume uptake and the effective polymer mesh size in a swollen equilibrium state are calculated using Equations 6.9 - 6.16.

First, the volume of the dry polymer V_{dry} , the volume of the polymer directly after polymerization V_{pol} , and the volume of the swollen polymer V_{sw} , are calculated as

$$V_{\text{dry}} = \frac{m_{\text{dry}}}{\rho} \quad (6.9)$$

$$V_{\text{pol}} = \frac{m_{\text{pol}} - m_{\text{pol_hep}}}{\rho_h} \quad (6.10)$$

$$V_{\text{sw}} = \frac{m_{\text{sw}} - m_{\text{sw_hep}}}{\rho_h} \quad (6.11)$$

where m_{dry} is the dry weight of the polymer in air. m_{pol} and $m_{\text{pol_hep}}$ are the weight directly after polymerization in air and heptane, respectively. m_{sw} and $m_{\text{sw_hep}}$ indicate the swollen weight in air and n-heptane. ρ denote the density of the polymer and ρ_h the density of n-heptane. The relaxed polymer volume fraction φ_{rel} in Equation 6.12 and fraction of the swollen polymer φ_{sw} in Equation 6.13 can then be calculated by

$$\varphi_{\text{rel}} = \frac{V_{\text{dry}}}{V_{\text{pol}}} \quad (6.12)$$

$$\varphi_{\text{sw}} = \frac{V_{\text{dry}}}{V_{\text{sw}}} \quad (6.13)$$

These volume fractions are subsequently used to access the degree of expansion of the polymer chains during swelling and their water intake capacity. The average molecular weight between cross-links \bar{M}_c can be calculated from derived quantities,

$$\frac{1}{\bar{M}_c} = \frac{\ln(1 - \varphi_{\text{sw}}) + \varphi_{\text{sw}} + \chi \cdot \varphi_{\text{sw}}^2}{-1 \cdot \left(1 - \frac{2}{f}\right) \cdot (1 - \gamma) \cdot V_1 \cdot \rho \cdot \varphi_{\text{rel}}^{\frac{2}{3}} \cdot \varphi_{\text{sw}}^{\frac{1}{3}}} \quad (6.14)$$

and

$$\gamma = \frac{f \cdot \bar{M}_c}{(f - 2) \cdot \bar{M}_n} \quad (6.15)$$

where $f = 1000$ [118] is the polymer's junction functionality of PEGDMA and \bar{M}_n indicates the average molecular weight of an oligomer chain, i.e. 550 g mol^{-1} and 750 g mol^{-1} , respectively. $\chi = 0.426$ [119] and $V_1 = 18 \text{ m}^3 \text{ mol}^{-1}$ [120] denote the

Flory-Huggins interaction parameter for PEG-water systems and the molar volume of the swelling medium which is water in this case.

The average polymer mesh size ξ can be calculated from \bar{M}_c by means of

$$\xi = \varphi_s^{-\frac{1}{3}} \sqrt{\left(1 - \frac{2}{f}\right) \bar{l}^2 \cdot C_\infty \cdot \frac{\lambda \cdot \bar{M}_c}{M_r}} \quad (6.16)$$

if the average bond length $\bar{l} = 0.15$ nm [121], the Flory characteristic ratio $C_\infty = 4$ for PEG [119], the number of backbone bonds of the repeating unit $\lambda = 3$ [118] and the molecular weight of the repeating unit $M_r = 44$ are known. The data refer to PEG, as this is present to the greatest extent in the polymer portion, and the methacrylate end groups are considered cross-linked.

6.3 Results and Discussion

In this chapter, the results are presented and discussed section by section, including the findings on the polymerization process, the temporal mass uptake, the diffusion resistance, and the polymer mesh size.

6.3.1 Analyzing the Polymerization Process

In both, the molding process and 3DP, the specimens are created from polymer resins by photopolymerization. This process is to be understood first in order to get a handle on it during production. Apparently, the state of the resin changes from liquid to solid. Before considering this solidification process, the viscosities of the liquid resins are measured in advance. In general, the viscosity of tested resins ranges between $28 \text{ Pa} \cdot \text{s}$ to $131 \text{ Pa} \cdot \text{s}$, as shown in Table 6.1. Distinct graduation from S-resins to L-resins can be seen, where viscosities of S-resins stay below $60 \text{ Pa} \cdot \text{s}$ and L-resins above $65 \text{ Pa} \cdot \text{s}$. The viscosities of mixtures without pHEMA (S_0 and L_0) are lower than viscosities of resins with 1.51 % or 1.94 % pHEMA content.

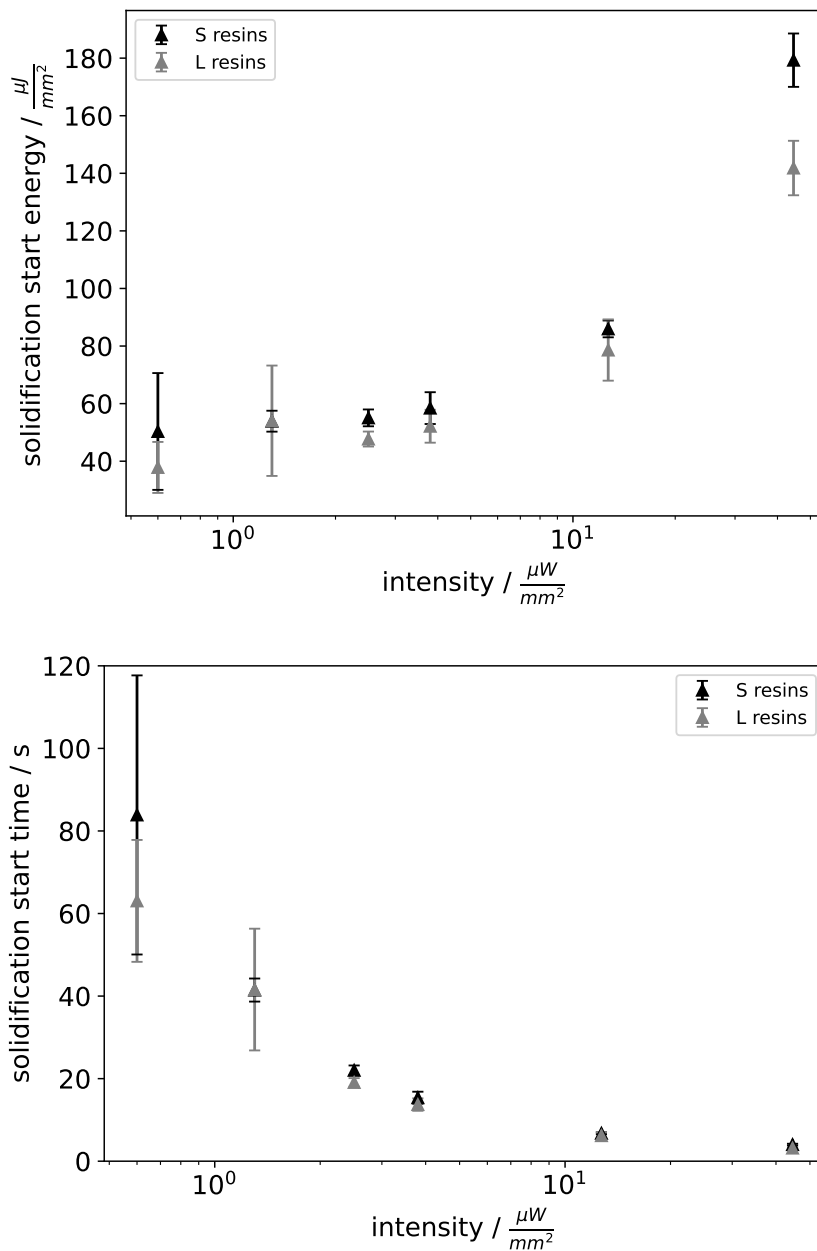


Figure 6.3: Solidification start energy per area SSE (top) and corresponding solidification start time SST (bottom) over intensity calculated from complex viscosity measurements during UV polymerization. [106]

Rheological measurements, from liquid resins to fully solid polymers, were performed repeatedly for all resins, as described in the experimental section. At first sight, the polymerization proceeds similarly in all resins. This is not surprising since the amount of PI in the resin mixtures is equal and is added in excess, related to the molar polymer fraction. However, variations based on the differing viscosity or composition are expected, which are to be assessed by further analysis of the data. As described in Section 6.2.1, the time at which the curves rise, and solidification begins is defined as the solidification start time (SST). The dotted line in Figure 6.1 shows that irradiation of $0.1 \mu\text{W}/\text{mm}^2$ is not sufficient to overcome the polymerization threshold in this experiment. The viscosity does not change during the observation period because the energy required to start polymerization is not reached. Whereas above irradiation of $0.5 \mu\text{W}/\text{mm}^2$ solidification proceeds entirely. A further approximation to the polymerization threshold was not investigated since a curing time of more than 2 min (120 s) is considered unfeasible for 3D printing.

Regarding measurements above the polymerization threshold, solidification curves follow a broadly similar course: after a certain duration, they ascend steeply before turning into a plateau, which is considered the end of the polymerization reaction. Low intensities lead to a slower increase, and high intensity curves increase steeper. Furthermore, by the SST indications at the horizontal axis in Figure 6.1, it can be easily recognized that curves measured at higher intensities increase earlier.

Summing up, there is a finite range in which radiation intensity and exposure time can be varied to adjust the time to complete solidification. In order to take a closer look at the energy per area to start the solidification, the so-called solidification start energy (SSE) is introduced, as already defined above. SSE can be defined as the SST multiplied by the laser intensity. Note that SSE is an energy per area that has been applied up to the moment when the viscosity curve starts to rise rather than the actual activation energy. The corresponding analysis across all resin versions is depicted in Figure 6.3. At the top, the SSE is plotted against the logarithmic laser intensity, whereas on the bottom, the SST is plotted against logarithmic intensity. Since there is only little variance between the resin versions, only S- and L-resins are distinguished by black and gray symbols, respectively. SST and SSE results are additionally listed in Table 6.2. The top graph of Figure 6.3 clearly reveals a separation between S- and L-resins at higher intensities. S-resins require a higher energy

per area to start the solidification. This tendency can already be observed at lower intensities, although less distinctly, through the uncertainties. It is reasonable to assume that the higher SSE of S-resins is caused by the lower viscosity and the shorter oligomer chains, which requires more reactions until the same degree of solidification has been established as in the case of L-resins.

At low intensities ($0.6 \mu\text{W}/\text{mm}^2$), depicted in the right graph in Figure 6.3, the SST ranges between 50s to 120s, due to the large error bars reflecting the poor reproducibility in this area. Towards higher intensities, a nonlinear relationship between the SST and the intensity becomes apparent. Moreover, it shows that the SST at high intensities is limited by a certain threshold, which can be seen from the last two measurements at the bottom right of Figure 6.3. Increasing of the intensity from $12.7 \mu\text{W}/\text{mm}^2$ to $44.6 \mu\text{W}/\text{mm}^2$, only causes a reduction of the SST of around 3s. The SSE of L-resins has already reached $180 \mu\text{J}/\text{mm}^2$ on average in this area. The SSE of S-resins has reached around $140 \mu\text{J}/\text{mm}^2$. The minimal average duration before the solidification starts can be estimated as 4s in the case of S-resins and 3.2s in the case of L-resins. Although the polymerization reaction is already in progress during this period, there is not yet a measurable change in viscosity. Further investigation on the actual activation energy of polymerization would reveal more insights here.

After the polymerization has started, the speed at which complete curing occurs is also strongly dependent on the laser intensity, as can be seen in Figure 6.1. A closer look at the time period until the curves reach their maximum and turn into a plateau also gives an estimation of the energy introduced until complete solidification is achieved under continuous irradiation. Therefore, the time of complete solidification is defined in the present study as the moment when the curve turns into a plateau. This moment is again determined by mathematical curve analysis using the temporal derivative of viscosity data. The time period during which the solidification takes place, the solidification duration (SD), is, therefore, the moment of complete solidification minus the SST. The solidification energy per area (SE), on the other hand, is defined as the energy per area accumulated over the whole time of exposure. An evaluation of the average duration until complete solidification and the energy per area applied until complete solidification as an average across all resins is provided in Table 6.2.

	intensity	0.6	1.3	2.5	3.8	12.7	44.6
solidification		$\mu\text{W}/\text{mm}^2$	$\mu\text{W}/\text{mm}^2$	$\mu\text{W}/\text{mm}^2$	$\mu\text{W}/\text{mm}^2$	$\mu\text{W}/\text{mm}^2$	$\mu\text{W}/\text{mm}^2$
start time SST / s							
S-resins		84 ± 34	41 ± 3	22 ± 1	15 ± 1	6.8 ± 0.2	4.0 ± 0.2
L-resins		63 ± 15	42 ± 15	19 ± 1	14 ± 2	6.2 ± 0.8	3.2 ± 0.2
duration SD / s							
S-resins		64 ± 12	52 ± 11	31 ± 4	20 ± 8	14 ± 5	11 ± 1
start energy SSE / $\mu\text{J}/\text{mm}^2$							
S-resins		50 ± 20	54 ± 4	55 ± 3	58 ± 6	86 ± 3	179 ± 9
L-resins		38 ± 9	54 ± 19	48 ± 3	52 ± 6	79 ± 11	142 ± 9
energy SE / $\mu\text{J}/\text{mm}^2$							
		82 ± 21	121 ± 25	130 ± 9	129 ± 36	258 ± 76	640 ± 52

Table 6.2: Listed solidification start times (SST), solidification durations (SD), solidification start energies per area (SSE) and solidification energies per area (SE). [106]

Over the investigated intensity range, solidification durations of more than 60 s, at $0.6 \mu\text{W}/\text{mm}^2$, to a minimum duration of 11 s, at $44.6 \mu\text{W}/\text{mm}^2$, are represented. As expected, the duration decreases with the increase in intensity. Nevertheless, the reduction of the duration, just like the reduction of the start time, is not linearly correlated with the intensity. At the highest intensity, a SD of about 11 s is still measurable in which the chain growth takes place. At this time, a maximum SE of $640 \mu\text{J}/\text{mm}^2$ on average is applied. The total exposure time (SST added to the corresponding SD) counts 15 s on average in this case until the resins are cured. Compared to the intensity of $12.7 \mu\text{W}/\text{mm}^2$, the SD is not significantly higher due to the error deviation, whereas the SE is significantly reduced, averaging just $258 \mu\text{J}/\text{mm}^2$.

In conclusion, the use of intensity above $12.7 \mu\text{W}/\text{mm}^2$ does not provide a reduction in the overall production time. As a commercial (closed) 3DP system was used in this study, the influence of varying laser intensity on the interfacial diffusion resistance requires further investigation and should be part of future work (cf. Section 6.5). From [122], it can be assumed that the laser intensity in a Formlabs 3D printer is $500 \mu\text{W}/\text{mm}^2$. Due to the high speed at which the laser traces each line, it can be concluded that the resins are not completely hardened in the first pass but only after repeated irradiation, which occurs anyway due to the layering structure. From the overall production time assuming a line width of around 0.15 mm [123] an exposure time of 0.4 s per line is conceivable, resulting in an SSE of $200 \mu\text{J}/\text{mm}^2$.

For the molding procedure used in this study, an intensity of $3.8 \mu\text{W}/\text{mm}^2$ and an (extra long) exposure time of 3 min was used in order to guarantee the complete solidification ($SE\ 684 \mu\text{J}/\text{mm}^2$). Based on these results, it is assumed that the 3D printed as well as the molded resins prepared in this study are equally fully polymerized. Nevertheless, it should be considered in further investigations that influences of the different irradiation procedures cannot be excluded.

However, the use of intensity above $44.6 \mu\text{W}/\text{mm}^2$ does most likely not provide any reduction in production time, as described above. On the other hand, in order to perform the 3DP process in a reasonable time, an SST of more than a few seconds cannot be considered acceptable. However, in order to ensure good bonding of two successive printed layers, a rather prolonged SD may be advantageous. The polymerization process could be prolonged by lowering the intensity and adjacent layers, therefore, building a stable bonding at the layer-layer interface. Since a commercial 3DP system was used in this study, an influence of varying laser intensity on the interfacial diffusion resistance can only be speculated, and further investigations are suggested as argued in Section 6.4.

6.3.2 Mass Uptake During Swelling

Polymer samples of six resin versions were prepared by both 3DP and the molding process (cf. Section 6.2) in order to analyze their behavior in a swelling medium and to investigate their diffusion properties. Once all samples were produced and dried to equilibrium, the mass uptake during swelling was measured and analyzed with the help of the curve fitting algorithm and error propagation, as described in Section 6.2. Figure 6.4 shows the mass uptake over soak time of molded resins (top) compared to printed resins (bottom). In both molded and printed resins, a distinct difference in mass uptake over time ΔM_r is visible between S- and L-resins. The faster diffusion in L-resins caused by the longer oligomer chain length of PEGDMA is dominant in both molded and printed resins.

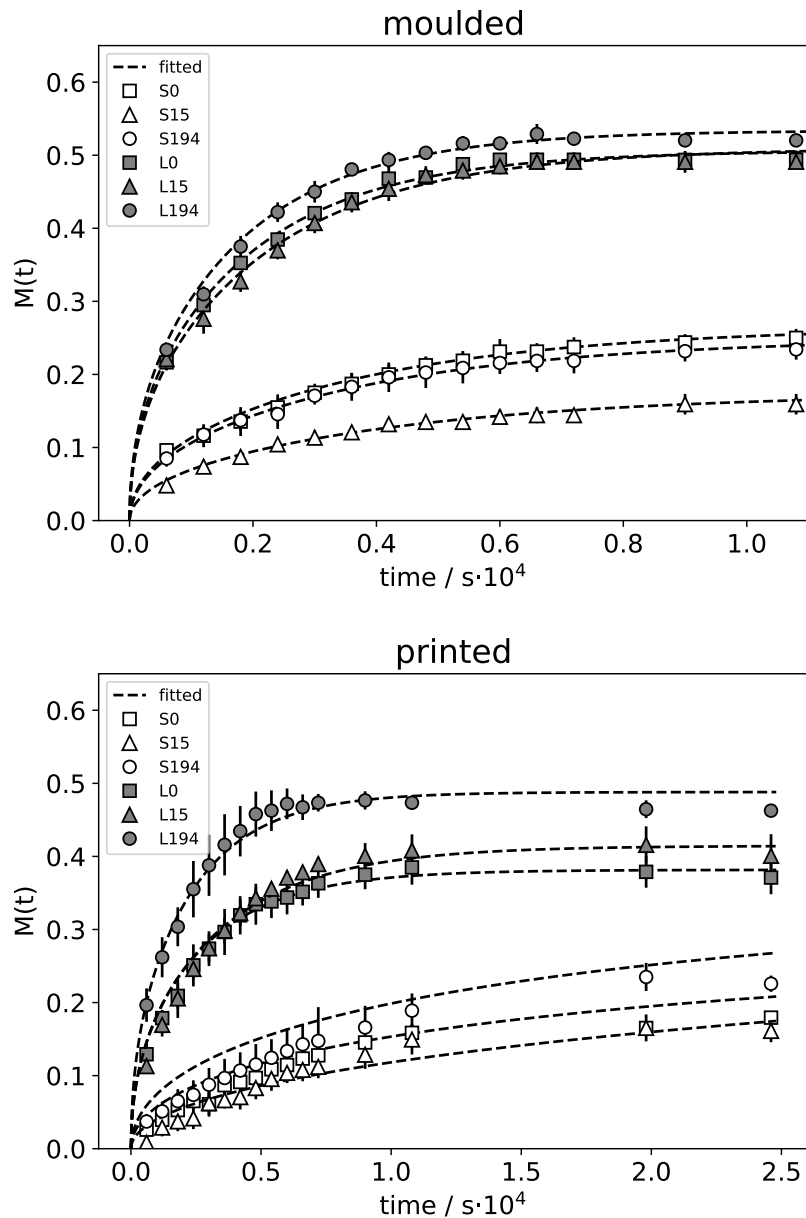


Figure 6.4: Mass uptake ΔM_r of moulded (top) and printed (bottom) polymer resins over a soak time of $1.1 \cdot 10^{-4}$ s (top) or $2.5 \cdot 10^{-4}$ s (bottom) in pH buffer. [106]

Comparing the manufacturing methods, it is noticeable that the mass uptake is slower for 3D printed specimens than for those prepared by the molding process. This deceleration of mass uptake can be seen in Figure 6.4; please note the different scaling at the x-axis. Moreover, the maximum mass uptake is found to be decreased in printed samples compared to the molded L-resins. A plateau indicating a saturation of the mass uptake curve of printed S-resins is reached after twice the time of molded S-resins. Regarding the L-resins, a deceleration by a factor of 1.25 is visible in the printed resins. Moreover, the maximum mass uptake is found to be decreased in printed samples compared to the molded L-resins. Further analysis of the curves is done by curve fitting with Equation 6.2 with p , q , r in the range from 0 to 500. The fitted curve maxima $M_{\infty \text{ printed}}$ and $M_{\infty \text{ molded}}$ of the printed and molded resins, as well as the corresponding diffusion coefficients, are listed in Table 6.3. As it can be seen in Figure 6.4 (bottom), the fitted curves do not match the plateau of printed S-resins. This misfitting is reflected in the $M_{\infty \text{ printed}}$ error deviation of S-resins compared to the rest of the M_{∞} values indicating an insufficient amount of measurement data at later times and are to be considered carefully. However, the reduction of the overall mass uptake is well reported in the case of L-resins and can be assigned to the layer structure. In Table 6.3 in the first two columns, the diffusion coefficient from molded samples (D_{bulk}) in any direction and from printed resins (D_{normal}) in normal direction are listed. Again, the values of printed S-resins are to be considered carefully. Nonetheless, the tremendous degree of reduction is evident, which is also illustrated in Figure 6.5.

Diffusion coefficients of S-resins are significantly reduced after 3DP compared to molded samples by 95 % on average. L-resins reveal reduced diffusion coefficients of around 60 % on average. The stronger impact of the layering process and, therefore, the increase in interfacial resistance in S-resins compared to L-resins can again be attributed to the shorter oligomer chain length, whose mobility is strongly constrained by the additional surfaces. This circumstance will be addressed again in the discussion section below.

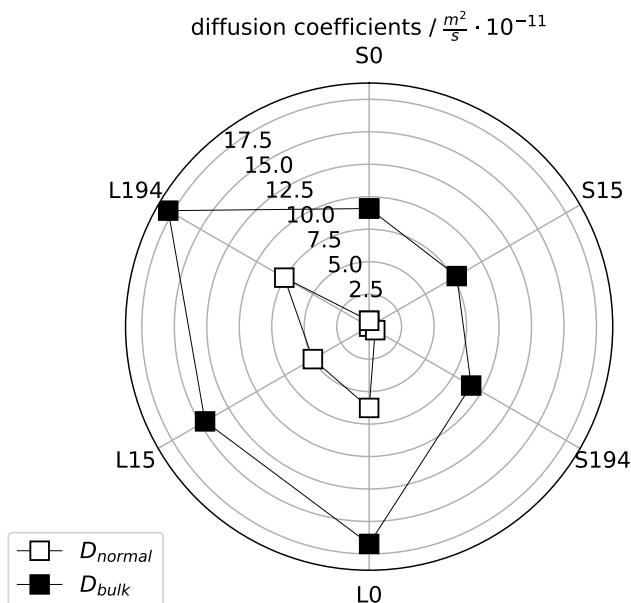


Figure 6.5: Diffusion coefficients determined by fitting mass uptake curves of 3D printed and molded resins S_0 , S_{15} , S_{194} , L_0 , L_{15} , L_{194} . [106]

6.3.3 Diffusion Resistance

Having evaluated the diffusion coefficients, it is worth considering the increase in diffusion resistance caused by the layerwise process. The diffusion resistance of every single interface $R_{\text{single}}^{\text{interface}}$ and each layer $R_{\text{single}}^{\text{layer}}$ was calculated from Equation 6.5 - 6.8, whereas the actual thickness of a layer d_{layer} was calculated by dividing the half thickness of the sample in dry condition by the half number of the layers (given by the 3D printer setup). $R_{\text{single}}^{\text{interface}}$ is evaluated for each resin using the diffusion coefficients from mass uptake data, and the results are listed in Table 6.3.

The average resistance values of the single layers $R_{\text{single}}^{\text{layer}}$ range between $2.4 \frac{s}{m} \cdot 10^5$ and $2.8 \frac{s}{m} \cdot 10^5$ for the S-resins and $1.24 \frac{s}{m} \cdot 10^5$ to $1.51 \frac{s}{m} \cdot 10^5$ for the L-resins, reflecting the diffusion coefficients of the bulk D_{bulk} . In order to evaluate the $R_{\text{single}}^{\text{interface}}$ of S-resins, the analyses should be repeated using an enhanced data basis. Interfacial resistance in L-resins is by $1.4 \frac{s}{m} \cdot 10^6$ to $0.9 \frac{s}{m} \cdot 10^6$ times higher than the resistance

Resin	D_{normal} $\frac{\text{m}^2}{\text{s}} \cdot 10^{-12}$	D_{bulk} $\frac{\text{m}^2}{\text{s}} \cdot 10^{-11}$	$M_{\infty \text{ printed}}$ $M \cdot 10^{-1}$	$M_{\infty \text{ molded}}$ $M \cdot 10^{-1}$	$R_{\text{single}}^{\text{layer}}$ $\frac{\text{s}}{\text{m}} \cdot 10^5$	$R_{\text{single}}^{\text{interface}}$ $\frac{\text{s}}{\text{m}} \cdot 10^6$	ξ_{printed} nm	ξ_{molded} nm
S0	5 ± 6	9.1 ± 0.7	2.7 ± 0.5	2.66 ± 0.06	2.4 ± 0.19	5 ± 6	1.4 ± 0.2	1.64 ± 0.07
S15	0.01 ± 0.02	7.8 ± 0.8	3.4 ± 0.1	1.76 ± 0.05	2.8 ± 0.3	$2 \cdot 10^3 \pm 8 \cdot 10^4$	1.3 ± 0.2	1.6 ± 0.2
S194	6 ± 6	9.1 ± 0.9	3.4 ± 0.7	2.51 ± 0.07	2.4 ± 0.25	4 ± 5	1.3 ± 0.4	1.60 ± 0.04
L0	63 ± 5	16.7 ± 0.4	3.80 ± 0.06	5.06 ± 0.02	1.32 ± 0.03	0.23 ± 0.03	2.4 ± 0.3	2.61 ± 0.02
L15	50 ± 4	14.6 ± 0.6	4.15 ± 0.06	5.10 ± 0.04	1.51 ± 0.06	0.29 ± 0.03	2.1 ± 0.2	2.43 ± 0.03
L194	76 ± 5	17.9 ± 0.4	4.88 ± 0.07	5.34 ± 0.02	1.24 ± 0.03	0.17 ± 0.02	2.1 ± 0.2	2.56 ± 0.09

Table 6.3: From left to right: diffusion coefficient of printed resins (in the normal direction) D_{normal} and of molded resins D_{bulk} , the maximum mass uptake $M_{\infty \text{ printed}}$ and $M_{\infty \text{ molded}}$, the diffusion resistance of the layer $R_{\text{single}}^{\text{layer}}$ and the interface $R_{\text{single}}^{\text{interface}}$ of printed resins and the average mesh size of printed ξ_{printed} and molded ξ_{molded} resins. [106]

of the bulk. Obviously, these results can only estimate the actual diffusion resistance of interfaces and layers, they nonetheless clearly demonstrate the highly divergent influence of the layering process on different resin compositions. These insights could be used in designing new polymer systems to predict and control drug release of individualized dosage forms.

6.3.4 Polymer Mesh Size

Besides the temporal change of the mass uptake process, the maximum volume increase is evaluated for further characterization of the polymer network. The maximum volume increase provides insight into how much the system changes during swelling and, therefore, on the average polymer mesh size in an equilibrium swollen state as described in Section 6.2. In the swollen equilibrium state, the mesh size of printed and molded resins was determined by Equation 6.16. The results are presented in Figure 6.6, and corresponding mean values with standard deviation are listed in Table 6.3.

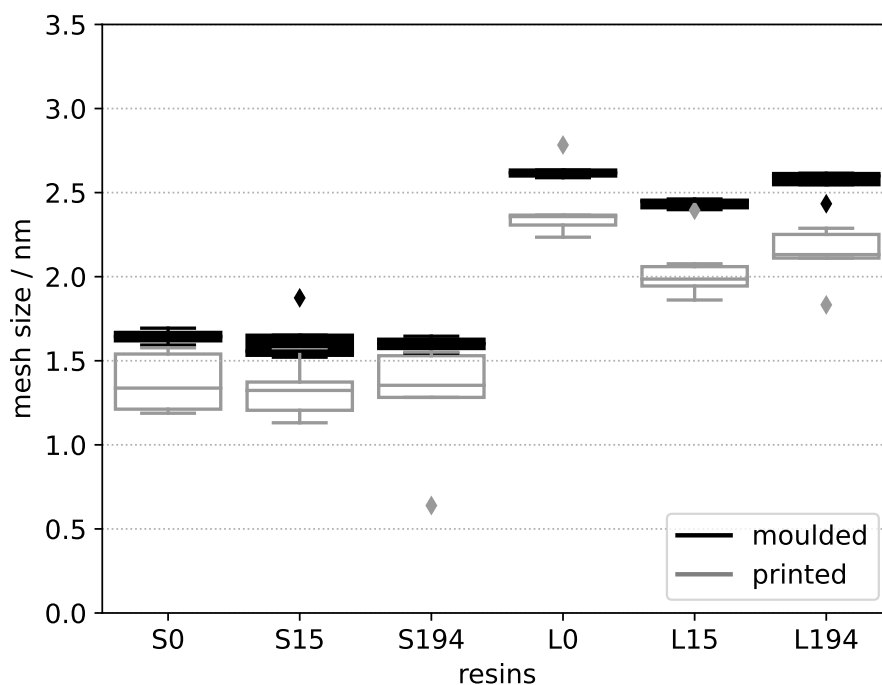


Figure 6.6: Box plot of polymer mesh sizes of 3D printed and molded resins calculated in equilibrium swollen state. [106]

From Figure 6.6 it can be seen that across all resin versions, molded resins have, on average, larger mesh sizes than printed resins. This observation coincides with previous results regarding water uptake. S-resins in general range between 1.3 nm to 1.64 nm, L-resins between 2.1 nm to 2.61 nm. There is no systematic trend obvious between the three variants of S- or L-resins. A general average mesh size for S-resins of approx. 1.6 nm in case of molded samples and approx. 1.3 nm on average in the case of printed samples could be estimated. In the case of L-resins, the general mesh size is on average 2.5 nm when molded and on average 2.2 nm when printed. Thus, the 3DP process leads to a reduction of the average mesh size of around 0.3 nm regardless of the oligomer chain length.

6.4 Contextual Discussion

Two polymer resin formulations, each in three variants, were investigated. The resin formulations differ mainly in the chain length of the oligomer PEGMDA, which is either represented with 9 PEG units (S-resins) or with 14 PEG units (L-resins). From each formulation, a version without additive polymer, a version with 1.51 % pHEMA, and a version with 1.94 % pHEMA was prepared. Previous studies indicated an influence of the pHEMA content on the diffusion properties [23]. Since pHEMA is not a reactant and is completely dissolved in the resin, an effect on the polymerization is unlikely. Although the individual variants differ in their initial viscosity, no influence of the pHEMA content on the course of polymerization was determined. Furthermore, when considering the diffusion properties of water entering the polymer network, no systematic influence of the pHEMA content could be confirmed either. Thus, it can be assumed that chemical interaction between pHEMA and the model drug caused the differences in the release.

In this study, an approach to determine the interfacial diffusion resistance in 3D printed polymers is presented. This is done under the assumption that diffusion in the normal direction, i.e. through the layers, is strongly disturbed by the interfaces between layers. In the lateral direction, i.e. in layer direction, diffusion behaves as in a molded polymer (without layers). The underlying measurement data of the temporal mass uptake of molded and printed polymer resins were fitted with Equation 6.2.

On a microscopic level, it is reasonable to consider the layers to have an inhomogeneous diffusion coefficient in cross-section due to the spatial proximity of their respective surfaces or interfaces. In the molded polymer, it is assumed that the bulk material is much more homogeneous.

There is ample evidence from experiments [124], theoretical considerations, and molecular dynamics simulations [125,126] that the polymer structure close to surfaces and interfaces is not isotropic, but the chains are elongated and oriented parallel to the interface- or surface layer. The strength of this effect depends on the molecular architecture (for instance, linear chains have, in general, larger flexibility to adapt their orientation), molecular weight, and the type of interface on the one hand. For molded resins, on the other hand, these interface effects are absent, and the usual bulk

isotropic behavior is observed. This implies that the printed resins will, in general, have a different average effective mesh size than the molded resins. This difference is expected to grow with decreasing layer thickness. Since, in this study, all resin compositions are based on the PEGDMA cross-linking molecule, and only internal interfaces between two polymer layers are considered, it becomes evident that the molecular weight is a decisive factor when it comes to the design of a 3D printable polymer resin for controlled drug release. It is, therefore, reasonable that the effects of 3DP are much stronger on the S-resins, which consist of PEGDMA oligomers with a 1.5 times lower molecular weight than the L-resins. From the results on the interfacial resistance, it becomes clear how much stronger the layer structure impacts on S-resins. These findings show that an individual design of the dosage forms, including the number of interfaces, is crucial for each individual resin formulation in order to enable the drug release mechanisms.

6.5 Conclusion

In the current study, the polymerization process of photopolymer resin containing PEGDMA with different molecular weights was analyzed. Furthermore, the resins were cured by both stereolithography and molding processes. The resulting polymer samples were compared regarding their mass uptake and swelling properties and revealing the impact of interfacial diffusion resistance in 3D printed polymers.

It was shown that S-resins containing oligomers with shorter chain lengths require more energy until a change in viscosity due to polymerization becomes apparent. Thanks to the precise analysis of the viscosity increase over time up to complete solidification, it will be possible in the future to adjust the 3D printing process (such as MLVS, Section 2.4.3) with regard to the resin used. In addition, the influence of interfaces can be utilized, minimized, or avoided. In order to access the influence of the layer structure resulting from the 3D printing process, layered and non-layered polymers were produced by SLA and molding process, respectively. Based on the insights into the polymerization process gained previously, it can be assumed that all samples were completely cured. The swelling experiments, however, show clear differences between molded and printed polymers. The significant increase in the overall diffusion resistance of layered specimens is attributable to the individual in-

terfacial diffusion resistances, which are far higher than those of the layer or bulk. The actual amount of interfacial resistance depends on the molecular weight of the initial oligomer. The bulk resistance does depend on the sample's volume or size, but the interfacial resistance does not. Therefore, a new degree of freedom in the design of controlled release on individualized dosage forms is obtained. The effective mesh size in the swollen equilibrium state was determined to be smaller for the printed specimens than for the molded ones. In both cases, however, a significantly larger mesh size can be measured for the L-samples compared to the S-samples.

In conclusion, a significant change in the polymer structure due to the printing process and, thus, a major influence on the diffusion properties could be shown. With knowledge of the interfacial diffusion resistance, it is essential to consider the layer thickness in the production of polymer dosage forms. At the same time, a modeling of the diffusion properties based on the precise knowledge of the influencing factors derived from this study is conceivable.

CHAPTER 7

Implants for Controlled Drug Release

This chapter presents a comparative analysis of polymer swelling and drug release experiments of testosterone (TE) containing resins (TE-resins) and methylene blue (MB) containing resins (MB-resins). It demonstrates the potential for active pharmaceutical ingredient (API) change in 3D printable polymer resins. In the experiments discussed in this chapter, castor oil is identified as the key co-solvent for the integration of TE into an aqueous polymer resin mixture. Furthermore, the results show an identical polymer mesh size in the equilibrium swollen state of TE- and MB-resins. Therefore, a general structural similarity between the two polymer networks can be assumed. However, in TE-resins, the diffusion coefficient of water during mass uptake is found to be larger compared to MB-resins. This also applies to the coefficient of TE diffusion during release testing. Further analysis of the TE and MB release curves shows that the API's molecular size seems to have a distinct influence on the diffusion rate. The results presented in this chapter can be used in the future to design diffusion properties of individualized polymer dosage forms. The remainder is structured as follows. Section 7.1 provides an introduction to the research problem, and Section 7.2 introduces the material used and methods applied in the experiments. The results and discussions of these experiments are presented in Section 7.3,

followed by a conclusion in Section 7.4.

The author declares that the following chapter includes verbatim quotes from [127].

7.1 Motivation

Due to new polymers used in pharmaceutical industries for the production of medical and pharmaceutical products, there is a growing interest in the individualization of medicines by 3D printing (3DP). In particular, the stereolithography (SLA) attracted attention only in the last few years. SLA was a little-noticed technology in pharmaceutical research for a long time. However, the advantages of SLA over other 3DP technologies are apparent. These include the free-from thermal and mechanical stress way of material processing and sterile contactless printing by laser. Thus, 3D printing of polymer-drug mixtures with this SLA reduces the risk of the enclosed API being decomposed. With an exception of APIs that are sensitive to light. The wide range of possible applications for SLA dosage forms includes, for example, loaded anti-agne implants for external applications [111], analgesic tablets [112], polypills with multi-drug loading [114], or bladder devices for local drug delivery [128].

Implants are of particular interest for the treatment of chronic diseases since patients are otherwise obliged to take medicines for months or years. Especially for elderly or mentally unstable persons, an implant loaded with APIs is advantageous, as a missed dose or an accidental overdose can be avoided. In the case of hypogonadism, which mostly affects aged men, the patient can no longer produce enough of the sex hormone testosterone. The decreasing or even disappearing testosterone level (below 3.2 ng/ml) [129] could lead to a number of severe disorders, such as erectile dysfunction [130], libido loss or depression [131]. When treating with TE, specific preferences and pharmacokinetics of the patient should be considered. In addition, the treatment with TE is repeatedly discussed regarding the provocation of prostate cancer [132]. An implant loaded with testosterone could ensure the individual regulation of the sexual hormone level. The continuous, controlled release of an appropriate amount of TE also avoids API level fluctuations in the patient's blood stream that are inevitable with oral application.

In Chapters 5 and 6, a formulation for drug-loaded implants was developed, and its suitability for controlled release was demonstrated. The corresponding experiments

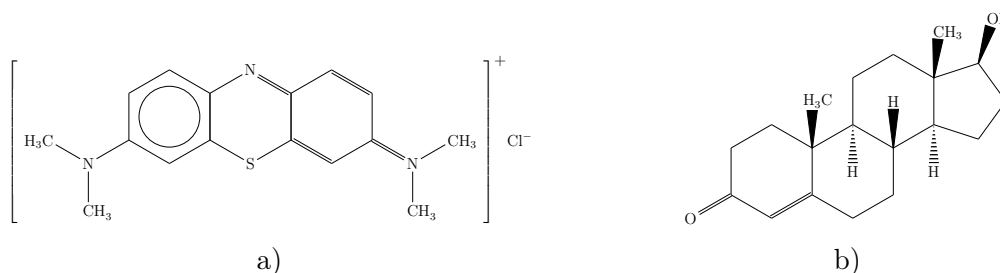


Figure 7.1: Chemical structures of a) the methylene blue molecule and b) the testosterone molecule. [127]

comprised six variants of a polymer resin mixture, in which methylene blue was integrated to test the release properties.

In this chapter, the aim of the experiments is to transfer the properties of the MB-loaded implants to the TE-loaded implants. A major challenge in pharmaceutical technology is the low solubility of active ingredients in the development of dosage forms. The MB molecule used in earlier studies has a solubility in water of 40 g/l, which is several orders of magnitude higher than the solubility of TE with only $2.41 \cdot 10^{-3}$ g/l. Therefore, an adaptation of the aqueous formulation is essential for the exchange of MB with TE. The results show that the TE formulation could be realized by adding castor oil as a co-solvent to achieve an oil-in-water emulsion. Release and swelling experiments demonstrate the diffusion properties of both the TE and the MB polymer resin. The diffusion of water influx, as well as the diffusion of the drug release, are analyzed. Furthermore, the polymer mesh size in the swollen equilibrium state is quantified.

7.2 Material and Methods

The oligomer Poly(ethylene glycol) dimethacrylate (PEGDMA) (CAS 25852-47-5) with a molecular weight of 550 g mol^{-1} and the photoinitiator Diphenyl (2,4,6-trimethylbenzoyl) phosphine oxide (TPO) (CAS 75980-60-8) were purchased from Tokyo Chemical Industry.

The Poly(2-hydroxyethyl methacrylate) (pHEMA) (CAS 25249-16-5) with a molecular weight of $2 \cdot 10^4 \text{ g mol}^{-1}$ was ordered from Abcr GmbH Germany. The refined

Table 7.1: Resin formulations of testosterone (TE) and methylene blue (MB) resins in wt%. The preparation of the resins is described in Section 7.2.1. [127]

Resin	PEGDMA	pHEMA	WATER	castor oil	Kolliphor	Testosterone	MB	TPO	
TE	66.2	1.5	8.9	16.6	4.8	2.1	0	1	/ wt%
MB	82.4	1.5	15.1	0	0	0	0.15	1	/ wt%

castor oil (CAS 08001-79-4) as well as macrogol-35-glycerol ricinoleate (Kolliphor EL)¹ were purchased from Caesar & Lorentz GmbH. The model drug MB (CAS 61-73-4), as well as the hormone TE (CAS 58-22-0) were purchased from Tokyo Chemical Industry. The chemical structure of MB and TE are depicted in Figure 7.1.

The molecular weight of MB is $319.85 \text{ g mol}^{-1}$, solubility in water at 20°C is 40 g/l [133] and the polar surface area (PSA) is 4.39 nm^2 [134]. TE has a molecular weight of $288.43 \text{ g mol}^{-1}$ [135], a solubility in water of $2.41 \cdot 10^{-3} \text{ g/l}$ (20°C) [133] and the PSA measures 3.73 nm^2 [136]. The swelling and dissolution medium is adjusted to a pH of 7.4 via a di-sodium hydrogen phosphate, sodium dihydrogen phosphate buffer.

7.2.1 Resin Preparation

In the following, resin mixtures that contain the API testosterone are referred to as TE-resins and mixtures that contain methylene blue are referred to as MB-resins. TE-resins are prepared in two separate partial preparations, which are later combined. In a first step, 8.9 wt% purified water, the half of the 66.2 wt% PEGDMA and 1.5 wt% pHEMA are mixed over night or until the pHEMA is dissolved entirely. In a second step, the rest of the PEGDMA, 16.6 wt% castor oil, 4.8 wt% Kolliphor EL and 2.1 wt% TE are stirred at 40°C to 45°C until a homogeneous emulsion has emerged. Both preparations are then combined, 1 wt% TPO is added and the mixture is again stirred for one hour.

The MB-resin mixture, named S_{15} in previous chapters, is prepared in a single step. 15.1 wt% purified water, 82.4 wt% PEGDMA, 1.5 wt% pHEMA, 0.15 wt% MB and 1 wt% TPO are added subsequently and left to stir for several hours until all com-

¹Kolliphor EL is an solubilizer and emulsifier from BASF added to the mixture to enhance the suspension of water and oil

ponents are dissolved. All weights and components are listed in Table 7.1 The resins are stored in brown glass at room temperature and processed under yellow light within a few days to prevent premature polymerization. A Zeiss Axioscope Vario microscope with polarization unit is used to verify the uniformity of the TE-resin and the absence of crystalline structures over a period of at least two weeks.

7.2.2 Sample Preparation

The specimens are prepared by ultraviolet (UV) radiation curing. For the best possible comparability, samples of the same shape and size are produced by molding. For this purpose, cell culture chambers (8-well on glass detachable) with a ground area of 12 mm by 9.5 mm from Sarstedt AG & Co. KG were used, as in previous molding processes. 2 mg liquid resin is pipetted into each chamber and irradiated with laser radiation with a wavelength of 405 nm and an irradiance of $3.8 \mu\text{W}/\text{mm}^2$ for 180 s.

7.2.3 Polymer Mesh Size Calculation

Mesh size estimation is based on the equilibrium swelling theory by Flory and Rehner [137], which was extended by Korsemeyer and Peppas [138]. In this study, a recent variant of the primary theory of Richbourg et al. considering highly cross-linked polymers is used for calculation of the mesh sizes [118]. Swelling experiments are conducted in a blood-like buffer medium of pH 7.4 at 37 °C. Cured samples of the TE-resin and the MB-resin are soaked separately for at least 4 h in order to achieve the maximum volume increase in the swollen equilibrium state. Therefore, the volume of specimens is ascertained by weighing in the initial state and at equilibrium.

The principle of buoyancy is utilized to estimate the volume, as described in Section 6.2.3. First, specimens are weighed immediately after polymerization in the air to determine the mass. The samples are then dried for 12 h in an oven. Subsequently, the volume of the dry polymer V_{dry} and the volume of the polymer directly after polymerization V_{pol} are calculated by Equations 6.9, 6.10 and 6.11.

After several hours of swelling, until a plateau level has been reached, samples are weighed again in air and n-heptane in order to estimate the polymer's volume in the swollen equilibrium state V_{sw} , cf. Equation 6.11. Furthermore, the relaxed and the

swollen polymer volume fraction φ_{rel} and φ_{sw} can be derived from the measured data using Equations 6.12 and 6.13. From Equation 6.14 and Equation 6.15 the average molecular weight between cross-links \bar{M}_c can be estimated [118].

The average polymer mesh size can subsequently be calculated from Equation 6.16 using the determined average molecular weight between cross-links. The parameters are consistent with those of the previous chapter and are taken from the literature as follows: $\chi = 0.426$ [119], $V_1 = 18 \text{ m}^3/\text{mol}$ [120], $f > 100$ [118], $\bar{l} = 0.15 \text{ nm}$ [121], $C_\infty = 4$ [119] and $\lambda = 3$ [118].

7.2.4 Mass Uptake

The mass uptake ΔM_r^{mass} of a polymer sample, as described before in Equation 6.1 is repeated in 7.1 for a better orientation. The indication $^{\text{mass}}$ serves to distinguish it from the relative release (cf. Section 7.2.5).

$$\Delta M_r^{\text{mass}} = \frac{m_a - m_{\text{dry}}}{m_{\text{dry}}} \quad (7.1)$$

ΔM_r^{mass} is determined by repeated weighing in the air m_a at intervals of 10 min over the entire period of the swelling progress, subtracted and divided by the initial dry weight in air m_{dry} . A two-dimensional plot of mass uptake over soak time results from measurement data and the curves are intended to quantify the diffusion coefficient of water entering the polymer network (cf. Figures 7.2).

7.2.5 Drug Release Measurements

A SOTAX AT7 smart dissolution tester is used for release testing. Testosterone and methylene blue releases are both measured in 750 mL of a di-sodium hydrogen phosphate, sodium dihydrogen phosphate buffer. The buffer is adjusted to a pH of 7.4 which corresponds to the pH of arterial blood. The temperature of the dissolution medium is regulated to 37°C. Uniform convection within the vessel is achieved via a paddle rotating with 100 rpm. Using an autosampler, 1 mL of medium is drawn at predetermined intervals (cf. Figure 7.3) and transferred to high-performance liquid

chromatography (HPLC)² vials. HPLC is used instead of spectroscopy due to the poor detectability of testosterone by light. Prior to each sampling, the system is rinsed with 100 mL of the release medium to wash out any TE remaining in the line. The volume of extracted buffer is not refilled, as a saturation concentration is never reached.

Due to the good detectability of MB via UV-Vis spectroscopy, MB release is measured using a BMG Labtech Spectrostar Nano. Note that the release measurements are taken from Chapter 5. For the measurement of TE release, an HPLC from Shimadzu with an Orbit 100 C18 column is used. After sampling, the buffer medium is replaced by 7 to 3 acetonitrile/water mixture and placed in an ultrasonic bath for 15 min, before starting the HPLC measurement routine. A mobile phase of water and methanol in a ratio of 2 to 8 and a flow rate of 1 mL min⁻¹ with isocratic elution³ is used to detect TE on an extinction maximum of 240 nm. In order to compare the release curves of MB and TE the temporal relative release ΔM_r^{drug} is determined as:

$$\Delta M_r^{drug} = \frac{n}{n_i} \quad (7.2)$$

The amount of API released at a certain time n is divided by the initial amount of API contained in the sample n_i before being placed into the dissolution medium. This initial amount is given by the exact amount of API added to the resin.

7.2.6 Diffusion Coefficients

In the following, two quite different processes, the diffusion of water into the polymer network and the diffusion of API out of the same polymer network, are described. Since both processes coincide in time and space, it is presumable that they also mutually influence each other. Nevertheless, the duration of mass uptake, which takes a few hours, strongly departs from the duration of release, which takes several days. Therefore, it is assumed that both processes can also be described independently of

²HPLC is an analytical method in which compounds dissolved in a liquid sample flow through a column at a constant flow rate and are thus separated. The analysis of the sample is done qualitatively (which components) and quantitatively (what amounts) by applying a reference calibration curve.

³The ratio of methanol and water is constant during the whole chromatographic process.

each other. As discussed in Chapter 4, it is strongly assumed that non-Fickian diffusion processes take place during water absorption due to the swelling of the polymer. However, the mathematical description of these non-Fickian processes requires a significantly better data basis and is therefore of no added value here. As in Chapter 6, the formula of Aktas et al. [117] is used to analyze the measurement curves. Since in this actual chapter only samples of the same size and shape are compared, the formula is reduced to a single diffusion coefficient. This is $D_{mass\ uptake}$ in the case of the mass absorption and $D_{drug\ release}$ in the case of the release curves. Thus, diffusion coefficients $D_{drug\ release}$ and $D_{mass\ uptake}$ are determined for the diffusion of API from the sample into the buffer medium and the diffusion of buffer medium into the polymer, respectively. The expression for the relative mass uptake $\Delta M_r^{mass}(t)$ is given in Equation 7.3

$$\Delta M_r^{mass}(t) = \Delta M_\infty \left(1 - \frac{512}{\pi^6}\right) \sum_{p=0}^{\infty} \sum_{q=0}^{\infty} \sum_{r=0}^{\infty} \frac{\exp(-\pi^2 \Gamma t)}{(2p+1)^2 \cdot (2q+1)^2 \cdot (2r+1)^2} \quad (7.3)$$

and

$$\Gamma = D_{mass\ uptake} \cdot \left(\frac{(2p+1)^2}{h_x^2} + \frac{(2q+1)^2}{h_y^2} + \frac{(2r+1)^2}{h_z^2} \right) \quad (7.4)$$

and the formula for the relative drug release $\Delta M_r^{drug}(t)$ over time is given in Equation 7.5 as follows:

$$\Delta M_r^{drug}(t) = \Delta M_\infty \left(1 - \frac{512}{\pi^6}\right) \sum_{p=0}^{\infty} \sum_{q=0}^{\infty} \sum_{r=0}^{\infty} \frac{\exp(-\pi^2 \Gamma t)}{(2p+1)^2 \cdot (2q+1)^2 \cdot (2r+1)^2} \quad (7.5)$$

and

$$\Gamma = D_{drug\ release} \cdot \left(\frac{(2p+1)^2}{h_x^2} + \frac{(2q+1)^2}{h_y^2} + \frac{(2r+1)^2}{h_z^2} \right) \quad (7.6)$$

with $h_x = 2$, $h_y = 12$ and $h_z = 9$ in both cases. The dimensions of the polymer samples being known, the curve specific M_∞ indicating the maximum of mass uptake or release and the individual diffusion coefficients are determined by means of SciPy 1.0 by least-square curve fitting of the measurement data implementing the Levenberg – Marquardt algorithm [104].

7.3 Results and Discussion

In this section, the findings resulting from the experiments are presented and discussed. This includes the polymer mesh size estimation, the temporal mass uptake, the drug release, and the corresponding diffusion coefficients.

7.3.1 Polymer Mesh Size

In the swollen equilibrium state, the volume increase was determined, and the polymer mesh size was estimated by the use of Equation 6.16. The results are listed in Table 7.2 on the left side. With $1.6 \text{ nm} \pm 0.1 \text{ nm}$ (standard deviation) for TE-resins, and $1.6 \text{ nm} \pm 0.2 \text{ nm}$ (standard deviation) for MB-resins, there is no difference in the mesh sizes of the two polymer resins after they are fully swollen. A similar mesh structure of both resins can therefore be assumed independent of the additional castor oil in TE-resins. This indicates that the choice of the oligomer chain length is largely responsible for the resulting mesh size. It is to be expected, and has been demonstrated in previous studies [23], that the polymer mesh size has a distinct influence on the release and swelling profile. Through the identical mesh size for both resins in an equilibrium swollen state in the present study, the influence of the swelling process on the release mechanism could be widely disregarded.

The molecular PSA, or more precisely the surface area associated with polar atoms, is a common indicator of passive molecular transport through a membrane [139]. The PSA can therefore also be used to predict the diffusion of drugs in polymer networks. In the following, the PSAs of MB and TE as given in Section 7.2 are used in the following to estimate the probability of an unhindered transport through the network. By the simplified assumption of a spherical free space within each mesh we can compare its surface area with the PSA of each API. The surface area of this space could be estimated to be around 8 nm^2 using the average mesh size of 1.6 nm as the diameter of the sphere. The PSA of MB and TE are 4.39 nm^2 and 3.73 nm^2 , respectively. The simple calculation shows that the surface of the mesh considered as sphere is approx. 1.8 times the size of the MB molecule's PSA and approx. 2.1 times the size of the TE PSA. A mutual hindrance of the API molecules moving through the polymer network is therefore well conceivable and could contribute to differences in the diffusion behavior.

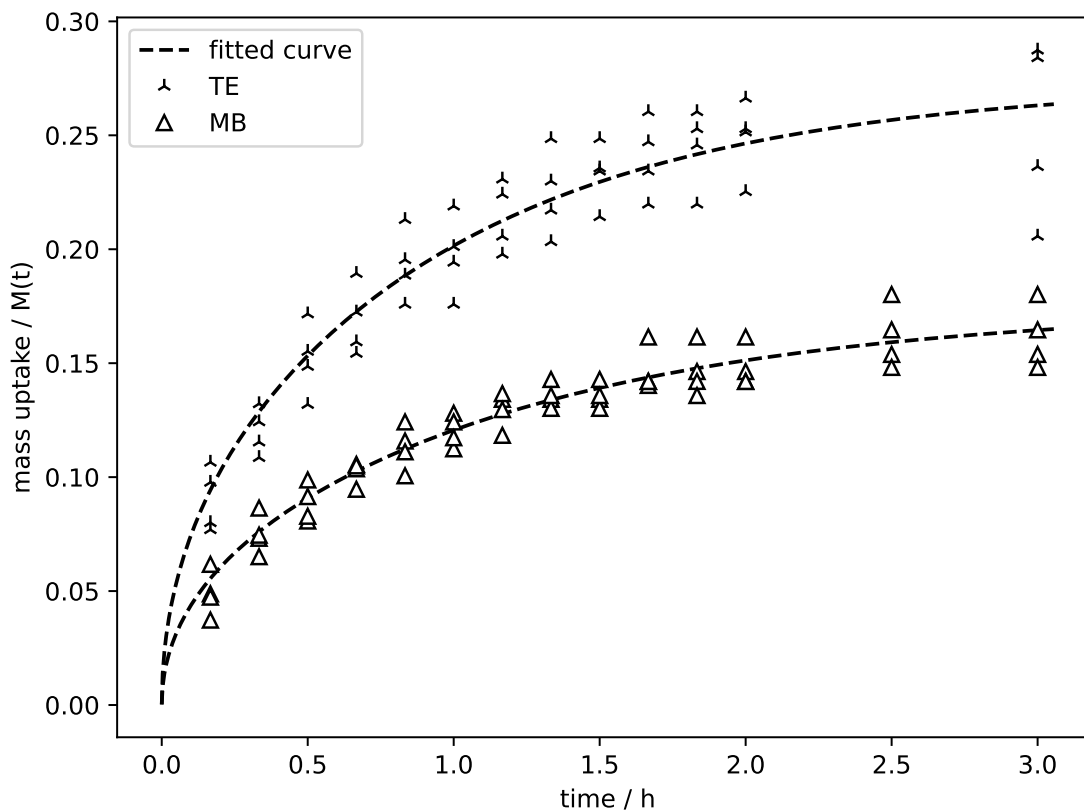


Figure 7.2: Mass uptake ΔM_r^{mass} of testosterone (TE) and methylene blue (MB) resins over a soak time of 3 h in pH 7.4 buffer at 37 °C; curves are fitted by the use of Equation 7.3. [127]

7.3.2 Mass Uptake

Samples of similar size and shape prepared from both TE- and MB-resins are soaked in a tempered buffer medium and weighed at regular intervals. The resulting curves of temporal mass uptake and the corresponding fitted curves are presented in Figure 7.2. Within the depicted period of 3 h, the TE measurement curve reaches a maximum relative mass uptake ΔM_r^{mass} of 0.26 ± 0.02 (fitted maximum value M_∞ is 0.27), while the MB curve reaches a maximum mass uptake of 0.16 ± 0.01 (M_∞ is 0.18). It is noteworthy that the maximum mass uptake of TE- and MB-resins differ, whereas

Table 7.2: The polymer mesh size ξ , the diffusion coefficients of the mass uptake $D_{mass\ uptake}$ and the diffusion coefficients of drug release $D_{drug\ release}$ of testosterone (TE) and methylene blue (MB) resins with corresponding standard deviation. [127]

Resin	ξ / nm	$D_{mass\ uptake} / \frac{m^2}{s} \cdot 10^{-11}$	$D_{drug\ release} / \frac{m^2}{s} \cdot 10^{-12}$
TE	1.6 ± 0.1	9.7 ± 1.0	11.5 ± 0.2
MB	1.6 ± 0.2	7.7 ± 0.8	5.7 ± 1.5

the maximum volume increase is equal (c.f. Section 7.3.1). It can be seen from Figure 7.2 and Table 7.2 that the water diffusion into MB-resins is slower than into TE-resins. $D_{mass\ uptake}$ from TE-resins is higher by a factor of 1.25 which shows that despite the identical mesh size in equilibrium swollen state, the velocity with which water enters the system varies considerably. It is conceivable that the different compositions of the resins, mainly the absence of oil in the MB-resin, lead to these detectable differences in density and surface tension in the molded polymer. When comparing the temporal mass uptake of both TE- and MB-resins, it is evident that the TE curve increases faster. It should be considered that in the case of MB-resins, the solvent, which is water, is vaporized during the drying process. In the case of TE-resins, the castor oil and the emulgator remain in the polymer. It is, therefore, reasonable to assume that the TE samples are already partly relaxed at the beginning of the swelling process. Moreover, it can be assumed that the oil which is not incorporated in the network leaks from the sample and that this circumstance contributes to the faster water uptake. Besides, it has been widely reported that both the concentration and the size of additives in polymer mixtures have an influence on the diffusion processes [140].

7.3.3 Drug Release

Characterizing the drug release is one of the most important criteria for drug development and is of particular interest for poorly soluble APIs like testosterone (TE). The temporal increasing concentration of TE and MB in the release medium divided by the total amount of API included in the sample is shown in Figure 7.3. The two measurement curves are distinctly separated. It can be seen that from both the

TE-resin and the MB-resin, not all of the API is released during the experiment. As the TE curve has reached an apparent plateau, it can be assumed that no or hardly any TE will be released in the further course. The second, the MB curve, on the other hand, has just reached its plateau value. Therefore, it cannot be excluded that some MB is still released. Regarding the TE-resins, the fraction released during the 40 h of observation is around $85\% \pm 5\%$. MB, on the other hand, was released to a maximum of $78\% \pm 7.5\%$ within 60 h. 50% of TE release occurred in the first 8 h whereas the 50% of MB was released within 10 h.

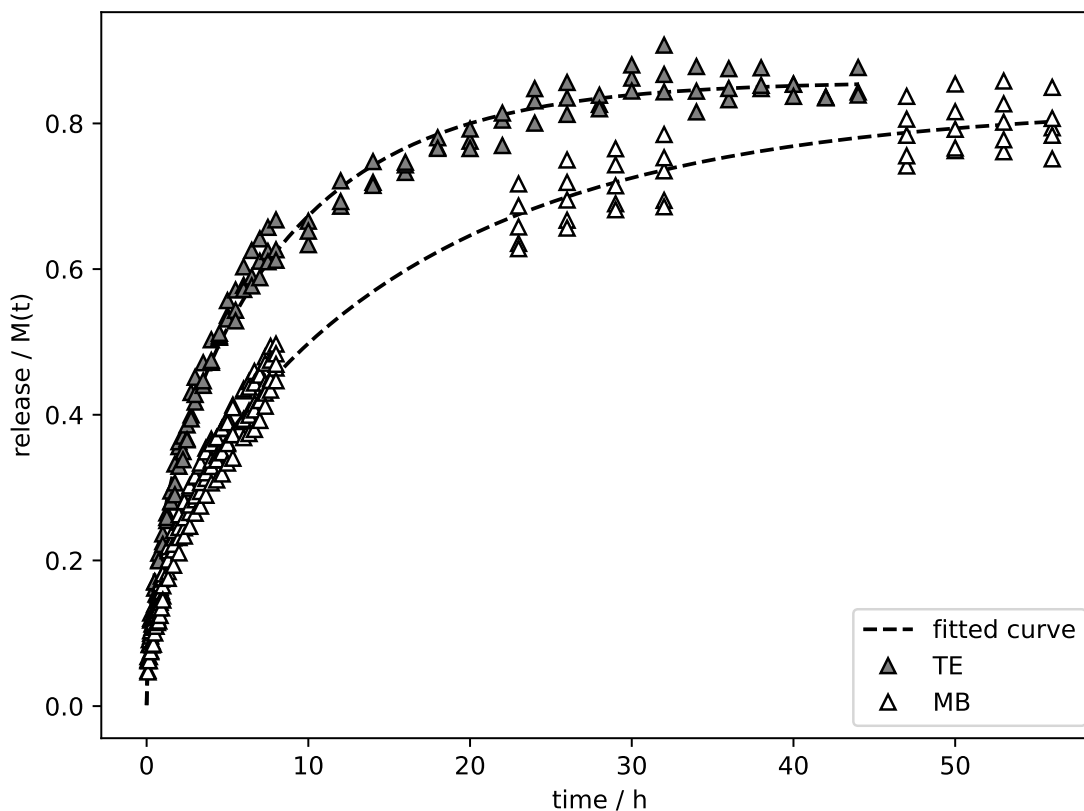


Figure 7.3: Testosterone (TE) and methylene blue (MB) release from polymer samples; curves are fitted by the use of Equation 7.5. [127]

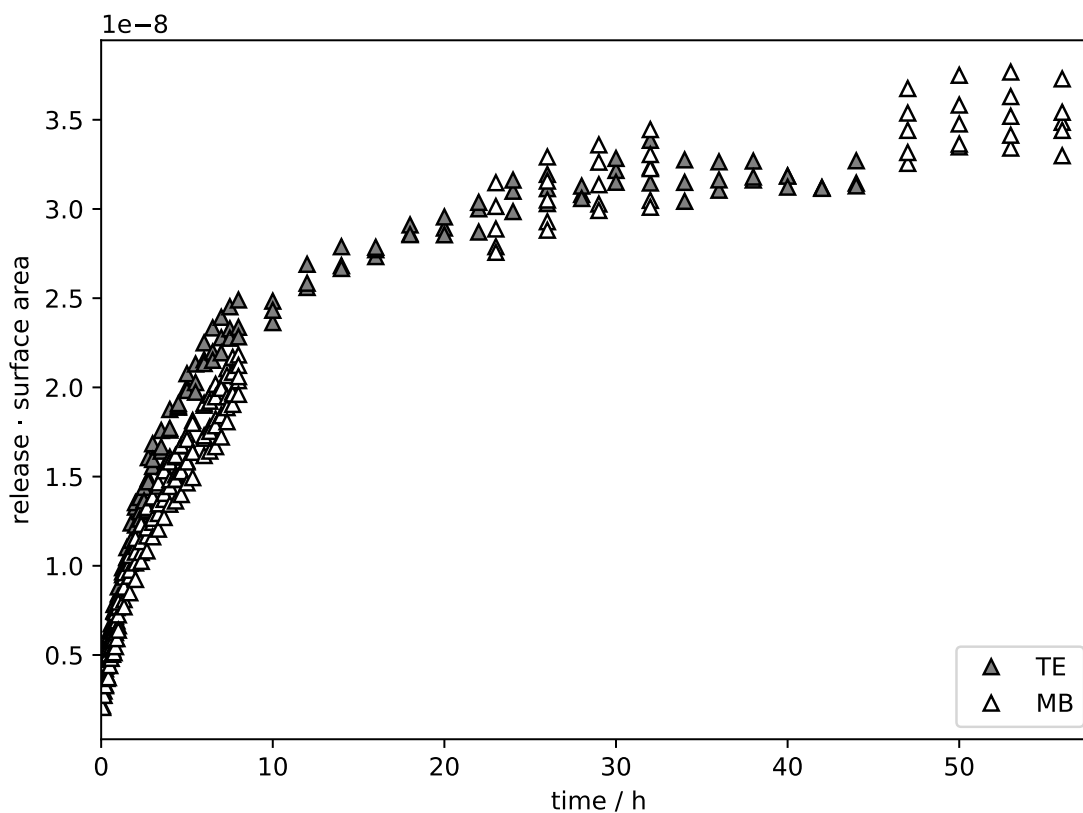


Figure 7.4: Drug release measurements multiplied by the surface area of testosterone (TE) and methylene blue (MB), respectively. [127]

Going further, the temporal release is analyzed by determining the diffusion coefficient of TE and MB by curve fitting. In Figure 7.3 the fitted curve is plotted as a black dashed line. Resulting diffusion coefficients of drug release $D_{drug\ release}$ are listed in Table 7.2 on the right side. A diffusion coefficient of $11.5 \cdot 10^{-12} \text{ m}^2/\text{s}$ is derived from the TE release curve and $5.7 \cdot 10^{-12} \text{ m}^2/\text{s}$ from MB release. Hence, the two diffusion coefficients diverge by a factor of 2. The curve maximum M_∞ of TE and MB release is determined to be 0.86 and 0.82, respectively, indicating that a similar overall release is likely.

Since the saturation concentration was not reached in both cases, solubility is not the

determining process of the release rate. The drug release process is largely controlled by pure Fickian diffusion, which is discussed in Section 7.3.1 and Chapter 4. It is, therefore, reasonable to assume an influence of the molecule's size on the release, as discussed before. Taking the molecule's polar surface area of TE and MB into account, the drug release curves are described by the release data multiplied by the specific surface area, which is shown in Figure 7.4. It can be observed that both release curves nearly fall together on a common curve. The proposed scaling can be used to design future diffusion properties by systematic manipulation of the ratio of molecule size to mesh size. Further research is suggested to investigate these findings. Finally, to assess the potential toxicity of the TE-resins, the photoinitiator (PI) was identified as the substance with the highest hazard. Besides, TPO is not included in the polymer network, so that unused residues might be released. This potential release of TPO from the TE-resins was investigated, and a maximum quantity of around 0.05 % of the total amount of TPO could be estimated from the release data.

7.4 Conclusion

In this chapter, it was demonstrated how an aqueous polymer resin formulation could be adapted for integrating TE by adding castor oil as a co-solvent. In the experiments, the original aqueous polymer resin formulation with MB (cf. Chapters 5 and 6) was compared to the alternative formulation with TE and the castor oil. The TE-resin contains 2.1 wt% API, which corresponds to 42 mg in our experiment. For long-term treatment, this amount should be increased; however, it clearly shows the feasibility for the use of 3D printed TE implants.

The corresponding release and swelling experiments were performed to verify whether the general properties of the original polymer system remained unchanged. As the results show, the average mesh size of the polymer network stays the same when replacing the solvent and the active ingredient, which is a sound basis for further analysis of the mass uptake and drug release experiment. It was shown that the major portion of the TE (approx. 85 %) was released from the polymer matrix into a blood-like buffer medium. Considering the low solubility of TE in water, this is a convincing result; however, it is unclear why the residual 15 % has not been released. Since neither the MB, which has excellent water solubility, is completely released, it

can be concluded that parts of the API cannot be released due to steric hindrance or have been decomposed. This is to be investigated in future experiments.

When compared with the MB release characteristics, TE had a higher diffusion coefficient despite an equal mesh size of both polymer systems. The influence of the polar surface area and, therefore, the size of the molecule on the diffusion processes is analyzed based on the measurements. It was reconfirmed that the smaller size of the TE molecule indeed affects its faster release from the polymer matrix. Similarly, the corresponding diffusion coefficient of water is higher during the mass uptake of the TE-resin than that of the MB-resin. The faster mass uptake of TE-resins indicates an initial relaxation of the TE-resin polymer system.

CHAPTER 8

Discussion and Conclusion

In the following, the contributions of this dissertation are discussed by outlining the results and contributions of the previous chapters. Afterward, possible future directions and ideas for follow-up studies are provided. Finally, this chapter concludes by referring to the motivation and research problem mentioned in the beginning.

8.1 Discussion

In Chapter 2, the current state of the art about pharmaceutical polymers was provided, followed by a section on particle movement and one on diffusion and mesh size measurement. Moreover, a review of the related work on 3D printing (3DP) with a particular focus on stereolithography and in addition, preliminary studies based on Multi Laser Volume Stereolithography (MLVS) — an stereolithography (SLA) variant — provide examples of how polymer dosage forms could be produced from a practical point of view.

In general, 3DP bears the potential of personalized medicine as it makes the individualized production of medications possible, leading to customized dosage forms with adapted shapes and sizes. However, most 3DP techniques are not qualified for phar-

maceutical applications as they require heat and mechanical stress during material processing. In this regard, SLA is a feasible solution, being based on contact-free laser processing. The required photopolymer resin is a key component for the successful fabrication of polymer dosage forms.

The release of the active substance in the patient's body is decisive for the effect of the polymer implants. Chapter 3 provides the fundamental theories for describing diffusion processes as well as concrete solutions to these theories in relation to experimental measurement data. Numerous studies in the past have dealt with the practical application of diffusion theories, such as those of Crank [7]. In Chapter 4, the simulation of diffusion processes is proposed as a forecast and as a validation of the results. Here, this thesis provides a novel contribution to the interpretation of experimental results from drug release studies.

Accuracy in the collection of measurement data and the preparation of samples is the most important factor in determining a valid diffusion coefficient. In addition, the choice of the diffusion model must be made within the scope of the measurement errors and taking into account the geometry of the sample. A model that describes a non-Fickian diffusion is only meaningful if the accuracy of the data makes such a differentiation possible at all. Finally, it can be seen that taking into account the question to be investigated in the study can lead to a significant improvement in the results. For follow-up studies, attention should be given to longer measurement times. This applies to the measurement of the samples as well as the selection of the diffusion model.

In the experimental part of this thesis, Chapter 5 contributes the design of a drug-loaded photopolymer resin formulation that satisfies the requirements for SLA 3DP. On the one hand, fast and complete photopolymerization is required in order to enable the curing of a stable 3D object by a focused movable laser beam within a reasonable printing time. On the other hand, polymers and solvents must allow the integration of active pharmaceutical ingredients (APIs) and need to be approved for pharmaceutical products.

Altogether, six variants of the methylene blue (MB) containing formulation that is mainly based on the cross-linker Poly(ethylene glycol) dimethacrylate (PEGDMA) were analyzed throughout Chapter 5. An additional polymer Poly(2-hydroxyethyl methacrylate) (pHEMA) is integrated into the resin to quantify its influence on the

drug release. To avoid the influence of 3DP, i.e. effects like layer artifacts, the resins were cured in standardized molds. Once the complete conversion of the resin was verified by spectroscopy, the release profile was analyzed.

The results indicate the considerable influence of the polymer chain length on the diffusion coefficient of the API. In comparison, the influence of the amount of pHEMA is substantially lower. Nevertheless, the analysis indicates an influence of pHEMA that, in combination with the chain length, can be exploited to control the release behavior.

In the next step, Chapter 6 evaluates how the diffusion properties of the polymers are influenced by the fabrication method. Since both methods are based on photopolymerization, the polymerization process is analyzed via the change in viscosity during irradiation. After evaluating the relationship between the laser irradiation and the solidification process using rheological measurements, samples of the same size and shape were prepared using 3DP and molding.

The SLA 3DP process results in layered structures within the printed object that affects the diffusion perpendicular to the layer direction. Consequently, 3DP is compared to the molding process in terms of the water diffusion into the polymer matrix. Therefore, the samples are soaked in a temperature-controlled pH-buffer solution for mass uptake. The results show a tremendous decrease in the diffusion coefficients of water intake due to the layering process. The three-dimensional Fourier series solution (refer to Section 3.3, Equation 3.31) has been modified to evaluate two distinct diffusion coefficients: one along the layer direction and another perpendicular to the layers. Specifically, the diffusion coefficient within the layers is assumed to be equivalent to that of the homogeneous material. In contrast, the diffusion coefficient in the direction orthogonal to the layers is primarily influenced by the interfaces created between two layers. It was shown that describing the layer system as a series circuit allows the determination of the diffusion resistance of the individual layers.

After the development and extensive analysis of the photopolymer resin, Chapter 7 deals with the adaptation of the polymer resin for the integration of a genuine API, namely testosterone (TE). Due to the very good water solubility of MB, which was used in previous experiments, water was used as the sole solvent in resin formulations. TE, on the other hand, is effectively insoluble in water, which necessitates the use of an additional solvent. A castor oil-water emulsification was used in this work and

was found to be an excellent link for embedding TE into the resin mixture.

The substitution of parts of the solvent and the API involves a modification of the resin formulation and has been discussed extensively in Chapter 7. The results show that the diffusion properties are changed in TE-resins compared to MB-resins. While there is an equal polymer mesh size in both polymers, the mass uptake, as well as the drug release, is faster in TE-resins. The initial relaxation of the polymer matrix due to the integrated oil, as well as the smaller particle size of TE compared to MB, is a reliable indication of these findings. Further analysis concerning the main source of the changes in diffusion properties is required.

8.2 Future Work

In the following, ideas for future work and possible next steps will be outlined. In general, there are four topics, including 1) the photopolymer resin, 2) the manufacturing process, 3) the active pharmaceutical ingredient and 4) the preliminary design of experiments that require further analysis.

Regarding 1) the photopolymer resin, the photoinitiator bears a potential toxicity risk. During irradiation, the photoinitiator is cleaved and falls into two parts, with only one of them being consumed during polymerization. Considering the consequences of the remaining unconsumed part for the human body in more detail should be included in future studies.

On the one hand, natural non-toxic photoinitiators reduce the risk of toxicity considerably. On the other hand, there is a risk of reduced performance due to lower conversion rates (cf. Section 2.1), and a clearer picture of the trade-offs is needed. Similarly, different variants of the polymer resin based on varying chain lengths of PEGDMA and pHEMA should be analyzed for the sake of better insights into the relationship between chain length and diffusion properties. In the future, cured polymers could be examined more precisely at the microscopic level with regard to the distribution of the individual components in the final sample and the formation of the polymer network.

Regarding 2) the 3DP, it is necessary to compare other and more diverse shapes of samples to gain more insights into the relationship between the surface-area-to-volume ratio and the drug release. Besides, the resins should be processed by means

of the MLVS prototype (cf. Section 2.4.3), and a side-by-side comparison with the molded and layer-printed samples should be pursued.

Regarding 3) the active pharmaceutical ingredient, the introduced formulation containing testosterone requires further investigation. For instance, the possible uncontrolled release of the oil, the resin's viscosity, and the course of the polymerization process as well as the mechanical properties, could be investigated further in the future. Finally, new insights into the investigated processes could result from the development and comprehensive characterization of further variants with additional APIs.

Regarding 4) the design of experiments, the expected results, including all possible sources of error, should be thought through in advance. It is advisable to tailor the collection of measurement data to the problem to be solved. This aspect benefits all of the above-mentioned topics and should be considered first.

8.3 Conclusion

This thesis contributes to the existing body of research on diffusion-controlled polymer resin-based dosage forms. This contribution involves the development of seven photopolymer resin formulations containing the model drug methylene blue (MB) and testosterone (TE) and its comprehensive characterization. The resins are analyzed regarding their viscosity and their photopolymerization process. Moreover, the polymer mesh size, the temporal swelling and mass uptake properties, and the drug release profiles of molded as well as 3D printed resins are discussed.

The successful development of individualized pharmaceutical dosage forms from polymer resin with controlled release can be realized by applying the results developed in this work. 3D printable photopolymer resin formulations containing MB or TE with reduced toxic risk by the avoidance of monomers could be realized. Resins are cured via molding and 3DP, allowing the comparison of both manufacturing processes in order to quantify the potential of additive manufacturing for the development of dosage forms.

The thesis presented here shows the importance of an interdisciplinary approach to address the complex issue of personalized drug delivery. The evaluation of the results using statistical methods provides a superior insight to the experimental findings with

regard to diffusion analysis. Investigating this question from the pharmaceutical as well as from the physical side and analyzing and discussing the data obtained in the respective context leads to a comprehensive assessment that contributes to a new generation of personalized dosage forms.

Bibliography

- [1] Ewa Rudnicka, Paulina Napierała, Agnieszka Podfigurna, Błażej Męczekalski, Roman Smolarczyk, and Monika Grymowicz. The world health organization (WHO) approach to healthy ageing. *Maturitas*, 139:6–11, September 2020.
- [2] Armin Geraili, Malcolm Xing, and Kibret Mequanint. Design and fabrication of drug-delivery systems toward adjustable release profiles for personalized treatment. *VIEW*, 2(5):20200126, May 2021.
- [3] Kewal K. Jain. *Textbook of Personalized Medicine*. Springer New York, 2009.
- [4] Y. Yang, Y. Zhao, A. Yu, D. Sun, and L.X. Yu. Oral drug absorption. In *Developing Solid Oral Dosage Forms*, pages 331–354. Elsevier, 2017.
- [5] Europäische Union. Verordnung (eu) 2017/745 des europäischen parlaments und des rates vom 5. april 2017 über medizinprodukte, zur änderung der richtlinie 2001/83/eg, der verordnung (eg) nr. 178/2002 und der verordnung (eg) nr. 1223/2009 und zur aufhebung der richtlinien 90/385/ewg und 93/42/ewg des rates. *Amtsblatt der Europäischen Union*, 60:1–175, 2017.
- [6] Christopher Stephen Andrew Musgrave and Fengzhou Fang. Contact lens materials: A materials science perspective. *Materials*, 12(2):261, 2019.

- [7] John Crank. *The mathematics of diffusion*. Clarendon Press, Oxford, [Eng], 2d ed edition, 1975.
- [8] Mi Steinbach and Michael Gartz. Multi Laser Volume Stereolithography, a new Freeform Fabrication Method. *RTejournal*, Vol. 2018, 2018.
- [9] Sijun Liu, Xuelong Chen, and Yilei Zhang. Hydrogels and hydrogel composites for 3D and 4D printing applications. In *3D and 4D Printing of Polymer Nanocomposite Materials*, pages 427–465. Elsevier, 2020.
- [10] Giulia Morello, Alessandro Polini, Francesca Scalera, Riccardo Rizzo, Giuseppe Gigli, and Francesca Gervaso. Preparation and characterization of salt-mediated injectable thermosensitive chitosan/pectin hydrogels for cell embedding and culturing. *Polymers*, 13(16), 2021.
- [11] Tarek A Ahmed and Bader M Aljaeid. Preparation, characterization, and potential application of chitosan, chitosan derivatives, and chitosan metal nanoparticles in pharmaceutical drug delivery. *Drug Design, Development and Therapy*, 10:483–507, January 2016.
- [12] Keren Delmar and Havazelet Bianco-Peled. Composite chitosan hydrogels for extended release of hydrophobic drugs. *Carbohydrate Polymers*, 136:570–580, January 2016.
- [13] Szymon Sip, Magdalena Paczkowska-Walendowska, Natalia Rosiak, Andrej Miklaszewski, Katarzyna Grabańska-Martyńska, Karolina Samarzewska, and Judyta Cielecka-Piontek. Chitosan as valuable excipient for oral and topical carvedilol delivery systems. *Pharmaceuticals*, 14(8), 2021.
- [14] Kseniia N. Bardakova, Tatiana A. Akopova, Alexander V. Kurkov, Galina P. Goncharuk, Denis V. Butnaru, Vitaliy F. Burdukovskii, Artem A. Antoshin, Ivan A. Farion, Tatiana M. Zharikova, Anatoliy B. Shekhter, Vladimir I. Yusupov, Peter S. Timashev, and Yury A. Rochev. From Aggregates to Porous Three-Dimensional Scaffolds through a Mechanochemical Approach to Design Photosensitive Chitosan Derivatives. *Marine Drugs*, 17(1):48, January 2019. Number: 1 Publisher: Multidisciplinary Digital Publishing Institute.

-
- [15] Tomasz Jungst, Willi Smolan, Kristin Schacht, Thomas Scheibel, and Jürgen Groll. Strategies and Molecular Design Criteria for 3D Printable Hydrogels. *Chem. Rev.*, 116(3):1496–1539, February 2016. Publisher: American Chemical Society.
- [16] Ali Bagheri and Jianyong Jin. Photopolymerization in 3D Printing. *ACS Applied Polymer Materials*, 1(4):593–611, April 2019.
- [17] Eliana B. Souto, Joana C. Campos, S. C. Filho, Maria C. Teixeira, Carlos Martins-Gomes, A. Zielinska, Claudia Carbone, and Amelia M. Silva. 3D printing in the design of pharmaceutical dosage forms. *Pharmaceutical Development and Technology*, 24(8):1044–1053, September 2019.
- [18] Sedigheh Borandeh, Bas van Bochove, Arun Teotia, and Jukka Seppälä. Polymeric drug delivery systems by additive manufacturing. *Advanced Drug Delivery Reviews*, 173:349–373, June 2021.
- [19] Ana Sara Cordeiro, Ismaiel A. Tekko, Mohamed H. Jomaa, Lalitkumar Vora, Emma McAlister, Fabiana Volpe-Zanutto, Matthew Nethery, Paul T. Baine, Neil Mitchell, David W. McNeill, and Ryan F. Donnelly. Two-Photon Polymerisation 3D Printing of Microneedle Array Templates with Versatile Designs: Application in the Development of Polymeric Drug Delivery Systems. *Pharm Res*, 37(9):174, August 2020.
- [20] Carlo Curti, Daniel J. Kirby, and Craig A. Russell. Stereolithography Apparatus Evolution: Enhancing Throughput and Efficiency of Pharmaceutical Formulation Development. *Pharmaceutics*, 13(5):616, May 2021. Number: 5.
- [21] Jen-Hung Fang, Che-Hau Liu, Ru-Siou Hsu, Yin-Yu Chen, Wen-Hsuan Chiang, Hui-Min David Wang, and Shang-Hsiu Hu. Transdermal Composite Microneedle Composed of Mesoporous Iron Oxide Nanoraspberry and PVA for Androgenetic Alopecia Treatment. *Polymers*, 12(6):1392, June 2020. Number: 6.
- [22] Andrew V. Healy, Evert Fuenmayor, Patrick Doran, Luke M. Geever, Clement L. Higginbotham, and John G. Lyons. Additive Manufacturing of

- Personalized Pharmaceutical Dosage Forms via Stereolithography. *Pharmaceutics*, 11(12):645, December 2019. Number: 12.
- [23] Mi Steinbach, Michael Gartz, and Richard Hirsch. Design and characterization of 3D printable photopolymer resin containing poly(2-hydroxyethyl methacrylate) for controlled drug release. *Journal of Drug Delivery Science and Technology*, 59:101850, October 2020.
- [24] Abdullah Mohammed, Amr Elshaer, Pooya Sareh, Mahmoud Elsayed, and Hany Hassanin. Additive Manufacturing Technologies for Drug Delivery Applications. *International Journal of Pharmaceutics*, 580:119245, April 2020.
- [25] Thomas Billiet, Mieke Vandenhaute, Jorg Schelfhout, Sandra Van Vlierberghe, and Peter Dubruel. A review of trends and limitations in hydrogel-rapid prototyping for tissue engineering. *Biomaterials*, 33(26):6020–6041, September 2012.
- [26] Robert Bail, Anand Patel, Hongyi Yang, Catherine M. Rogers, Felicity R. A. J. Rose, Joel I. Segal, and Svetan M. Ratchev. The Effect of a Type I Photoinitiator on Cure Kinetics and Cell Toxicity in Projection-Microstereolithography. *Procedia CIRP*, 5:222–225, January 2013.
- [27] Boning Zeng, Zhenlong Cai, Jacques Lalevée, Qizhi Yang, Haiwang Lai, Pu Xiao, Jing Liu, and Feiyue Xing. Cytotoxic and cytocompatible comparison among seven photoinitiators-triggered polymers in different tissue cells. *Toxicology in Vitro*, 72:105103, April 2021.
- [28] Paola Occhetta, Roberta Visone, Laura Russo, Laura Cipolla, Matteo Moretti, and Marco Rasponi. VA-086 methacrylate gelatine photopolymerizable hydrogels: A parametric study for highly biocompatible 3D cell embedding. *Journal of Biomedical Materials Research Part A*, 103(6):2109–2117, 2015. _eprint: <https://onlinelibrary.wiley.com/doi/pdf/10.1002/jbm.a.35346>.
- [29] Alexander K Nguyen, Shaun D Gittard, Anastasia Koroleva, Sabrina Schlie, Arune Gaidukeviciute, Boris N Chichkov, and Roger J Narayan. Two-photon polymerization of polyethylene glycol diacrylate scaffolds with riboflavin and

-
- triethanolamine used as a water-soluble photoinitiator. *Regenerative Medicine*, 8(6):725–738, November 2013.
- [30] Pamela Robles Martinez, Alvaro Goyanes, Abdul W. Basit, and Simon Gaisford. Fabrication of drug-loaded hydrogels with stereolithographic 3D printing. *International Journal of Pharmaceutics*, 532(1):313–317, October 2017.
- [31] Jing Zhang and Pu Xiao. 3D printing of photopolymers. *Polymer Chemistry*, 9(13):1530–1540, 2018.
- [32] Aleksa Milovanović, Miloš Milošević, Goran Mladenović, Blaž Likozar, Katarina Čolić, and Nenad Mitrović. Experimental dimensional accuracy analysis of reformer prototype model produced by fdm and sla 3d printing technology. In *Experimental and numerical investigations in materials science and engineering*, pages 84–95. Springer, 2018.
- [33] Judah Balli, Subha Kumpaty, and Vince Anewenter. Continuous liquid interface production of 3d objects: An unconventional technology and its challenges and opportunities. In *ASME International Mechanical Engineering Congress and Exposition*, volume 58400, page V005T06A038. American Society of Mechanical Engineers, 2017.
- [34] Witold Jamróz, Joanna Szafraniec, Mateusz Kurek, and Renata Jachowicz. 3D Printing in Pharmaceutical and Medical Applications – Recent Achievements and Challenges. *Pharmaceutical Research*, 35(9):176, September 2018.
- [35] Lech Gmachowski. Fractal model of anomalous diffusion. *European Biophysics Journal*, 44:613–621, 2015.
- [36] Raffaella Burioni, Giacomo Gradenigo, Alessandro Sarracino, A Vezzani, and Angelo Vulpiani. Scaling properties of field-induced superdiffusion in continuous time random walks. *Communications in Theoretical Physics*, 62(4):514, 2014.
- [37] Jae-Hyung Jeon and Ralf Metzler. Fractional brownian motion and motion governed by the fractional langevin equation in confined geometries. *Physical Review E—Statistical, Nonlinear, and Soft Matter Physics*, 81(2):021103, 2010.

- [38] G Zumofen, J Klafter, and MF Shlesinger. Lévy flights and lévy walks revisited. In *Anomalous Diffusion From Basics to Applications: Proceedings of the XIth Max Born Symposium Held at Łądek Zdrój, Poland, 20–27 May 1998*, pages 15–34. Springer, 1999.
- [39] Gandhimohan M Viswanathan, EP Raposo, and MGE Da Luz. Lévy flights and superdiffusion in the context of biological encounters and random searches. *Physics of Life Reviews*, 5(3):133–150, 2008.
- [40] Chilou Zhou, Yanlei Huang, Yiran Zheng, and Zhengli Hua. Hydrogen permeation behavior of rubber sealing materials for hydrogen infrastructure: Recent advances and perspectives. *International Journal of Hydrogen Energy*, 59:742–754, 2024.
- [41] Mi Steinbach and Michael Gartz. Multi laser volume stereolithography, a new freeform fabrication method. *RTEjournal - Fachforum für Rapid Technologien*, 2018(1), 2018.
- [42] Hideo Kodama. Automatic method for fabricating a three-dimensional plastic model with photo-hardening polymer. *Review of Scientific Instruments*, 52(11):1770–1773, 1981.
- [43] Charles W. Hull. Apparatus for production of three-dimensional objects by stereolithography, December 1989.
- [44] Kalim Deshmukh, Aqib Muzaffar, Tomáš Kovářík, Tomáš Křenek, M. Basheer Ahamed, and S. K. Khadheer Pasha. Fundamentals and applications of 3D and 4D printing of polymers: Challenges in polymer processing and prospects of future research. In *3D and 4D Printing of Polymer Nanocomposite Materials*, pages 527–560. Elsevier, 2020.
- [45] Xiaoyan Xu, Atheer Awad, Pamela Robles-Martinez, Simon Gaisford, Alvaro Goyanes, and Abdul W. Basit. Vat photopolymerization 3D printing for advanced drug delivery and medical device applications. *Journal of Controlled Release*, 329:743–757, January 2021.

-
- [46] Linjie Li and John T. Fourkas. Multiphoton polymerization. *Materials Today*, 10(6):30–37, June 2007.
- [47] John R. Tumbleston, David Shirvanyants, Nikita Ermoshkin, Rima Janusziewicz, Ashley R. Johnson, David Kelly, Kai Chen, Robert Pinschmidt, Jason P. Rolland, Alexander Ermoshkin, Edward T. Samulski, and Joseph M. DeSimone. Continuous liquid interface production of 3D objects. *Science*, 347(6228):1349–1352, March 2015.
- [48] Guangbin Shao, Rihan Hai, and Cheng Sun. 3D Printing Customized Optical Lens in Minutes. *Advanced Optical Materials*, 8(4):1901646, 2020. _eprint: <https://onlinelibrary.wiley.com/doi/pdf/10.1002/adom.201901646>.
- [49] Zhihan Hong, Piaoran Ye, Douglas A. Loy, and Rongguang Liang. Three-dimensional printing of glass micro-optics. *Optica*, 8(6):904–910, Jun 2021.
- [50] A. Gebhardt. *Generative Fertigungsverfahren: Additive Manufacturing und 3D Drucken für Prototyping - Tooling - Produktion*. Carl Hanser Verlag GmbH & Company KG, 2013.
- [51] Jim H Lee, Robert K Prud’Homme, and Ilhan A Aksay. Cure depth in photopolymerization: Experiments and theory. *Journal of Materials Research*, 16(12):3536–3544, 2001.
- [52] Paul F Jacobs. Fundamentals of stereolithography. In *1992 International Solid Freeform Fabrication Symposium*, 1992.
- [53] Charles W Hull. Apparatus for production of three-dimensional objects by stereolithography, March 11 1986. US Patent 4,575,330.
- [54] Evanthia Anadioti, Brittany Kane, and Elizabeth Soulas. Current and emerging applications of 3d printing in restorative dentistry. *Current Oral Health Reports*, 5:133–139, 2018.
- [55] S Witkowski and R Lange. Stereolithographie als generatives verfahren in der zahntechnik. *Schweiz Monatsschr Zahnmed*, 113(8):869, 2003.

- [56] Byoung Soo Kim, Jung-Seob Lee, Ge Gao, and Dong-Woo Cho. Direct 3d cell-printing of human skin with functional transwell system. *Biofabrication*, 9(025034), 2017.
- [57] A Maroni, A Melocchi, F Parietti, A Foppoli, L Zema, and A Gazzaniga. 3d printed multi-compartment capsular devices for two-pulse oral drug delivery. *Journal of Controlled Release*, 268:10–18, 2017.
- [58] SH Sun, HW Chiang, and MI Lee. Adaptive direct slicing of a commercial cad model for use in rapid prototyping. *The International Journal of Advanced Manufacturing Technology*, 34:689–701, 2006.
- [59] Bu Rongxia, Luo Shiyong, Xu Wencai, Meng Ruiqiang, and et.al. Characterization of thee uv–visible absorption spectra of commonly used photoinitiators. *Topics in Intelligent Computing and Industry Design*, 1 (2):18–20, 2017.
- [60] Subrahmanyam Chandrasekhar. Stochastic problems in physics and astronomy. *Reviews of modern physics*, 15(1):1, 1943.
- [61] Michael Bengfort, Horst Malchow, and Frank M Hilker. The fokker–planck law of diffusion and pattern formation in heterogeneous environments. *Journal of mathematical biology*, 73:683–704, 2016.
- [62] Daniele Andreucci, Emilio NM Cirillo, Matteo Colangeli, and Davide Gabrielli. Fick and fokker–planck diffusion law in inhomogeneous media. *Journal of Statistical Physics*, 174:469–493, 2019.
- [63] Beomjun Choi and Yong-Jung Kim. Diffusion of biological organisms: Fickian and fokker–planck type diffusions. *SIAM Journal on Applied Mathematics*, 79(4):1501–1527, 2019.
- [64] IG Abel, M Barnes, SC Cowley, W Dorland, and AA Schekochihin. Linearized model fokker–planck collision operators for gyrokinetic simulations. i. theory. *Physics of Plasmas*, 15(12), 2008.
- [65] Ludwig M Böss, Ulrich P Steinwandel, Klaus Dolag, and Harald Lesch. crescendo: an on-the-fly fokker–planck solver for spectral cosmic rays in cos-

-
- mological simulations. *Monthly Notices of the Royal Astronomical Society*, 519(1):548–572, 2023.
- [66] B Wolle. Stochastic modelling of air passenger volume during the covid-19 pandemic and the financial impact on german airports. *Fortune Journal of Health Sciences*, DOI:10.26502/fjhs.204, 7, 2024.
- [67] Jagdev Singh, Ved Prakash Dubey, Devendra Kumar, Sarvesh Dubey, and Dumitru Baleanu. Fractal-view analysis of local fractional fokker–planck equation occurring in modelling of particle’s brownian motion. *Optical and Quantum Electronics*, 56(7):1109, 2024.
- [68] E Bringuier. Particle diffusion in an inhomogeneous medium. *European journal of physics*, 32(4):975, 2011.
- [69] Diego Caccavo. An overview on the mathematical modeling of hydrogels’ behavior for drug delivery systems. *International Journal of Pharmaceutics*, 560:175 – 190, 2019.
- [70] *European Pharmacopoeia 11th Edition*. EDQM Council of Europe, 2022.
- [71] Ana C Freire, Abdul W Basit, Rahul Choudhary, Chee W Piong, and Hamid A Merchant. Does sex matter? the influence of gender on gastrointestinal physiology and drug delivery. *International journal of pharmaceutics*, 415(1–2):15–28, 2011.
- [72] Jean-Marie Nicolas, Pascal Espie, and Mathieu Molimard. Gender and interindividual variability in pharmacokinetics. *Drug metabolism reviews*, 41(3):408–421, 2009.
- [73] Marius Rademaker. Do women have more adverse drug reactions? *American journal of clinical dermatology*, 2(6):349–351, 2001.
- [74] Richard M Martin, Pipasha N Biswas, Shayne N Freemantle, Gillian L Pearce, and Ronald D Mann. Age and sex distribution of suspected adverse drug reactions to newly marketed drugs in general practice in england: analysis of 48 cohort studies. *British journal of clinical pharmacology*, 46(5):505–511, 1998.

- [75] Shajahan Abdul, Anil V Chandewar, and Sunil B Jaiswal. A flexible technology for modified-release drugs: multiple-unit pellet system (mups). *Journal of controlled release*, 147(1):2–16, 2010.
- [76] Mangesh E Bhad, Shajahan Abdul, Sunil B Jaiswal, Anil V Chandewar, Jayesh M Jain, and Dinesh M Sakarkar. Mups tablets—a brief review. *International journal of pharmtech research*, 2(1):847–855, 2010.
- [77] Sebastian Koltzenburg, Michael Maskos, and Oskar Nuyken. *Polymere: Synthese, Eigenschaften und Anwendungen*. Springer-Verlag, 2013.
- [78] Kapilkumar Vithani, Alvaro Goyanes, Vincent Jannin, Abdul W. Basit, Simon Gaisford, and Ben J. Boyd. An overview of 3d printing technologies for soft materials and potential opportunities for lipid-based drug delivery systems. *Pharmaceutical Research*, 36(1):4, Nov 2018.
- [79] Witold Jamróz, Joanna Szafranec, Mateusz Kurek, and Renata Jachowicz. 3d printing in pharmaceutical and medical applications—recent achievements and challenges. *Pharmaceutical research*, 35(9):176, 2018.
- [80] Ferry PW Melchels, Jan Feijen, and Dirk W Grijpma. A review on stereolithography and its applications in biomedical engineering. *Biomaterials*, 31(24):6121–6130, 2010.
- [81] Alvaro Goyanes, Usanee Det-Amornrat, Jie Wang, Abdul W Basit, and Simon Gaisford. 3d scanning and 3d printing as innovative technologies for fabricating personalized topical drug delivery systems. *Journal of controlled release*, 234:41–48, 2016.
- [82] Jie Wang, Alvaro Goyanes, Simon Gaisford, and Abdul W Basit. Stereolithographic (sla) 3d printing of oral modified-release dosage forms. *International journal of pharmaceuticals*, 503(1-2):207–212, 2016.
- [83] Pamela Robles Martinez, Alvaro Goyanes, Abdul W Basit, and Simon Gaisford. Fabrication of drug-loaded hydrogels with stereolithographic 3d printing. *International journal of pharmaceuticals*, 532(1):313–317, 2017.

-
- [84] Pamela Robles Martinez, Alvaro Goyanes, Abdul W Basit, and Simon Gaisford. Influence of geometry on the drug release profiles of stereolithographic (sla) 3d-printed tablets. *AAPS PharmSciTech*, 19(8):3355–3361, 2018.
- [85] Paula Andrade-Vivero, Elena Fernandez-Gabriel, Carmen Alvarez-Lorenzo, and Angel Concheiro. Improving the loading and release of nsoids from phema hydrogels by copolymerization with functionalized monomers. *Journal of pharmaceutical sciences*, 96(4):802–813, 2007.
- [86] Jonghwan Mun, Jee won Mok, Sanghoon Jeong, Seonghwi Cho, Choun-Ki Joo, and Sei Kwang Hahn. Drug-eluting contact lens containing cyclosporine-loaded cholesterol-hyaluronate micelles for dry eye syndrome. *RSC advances*, 9(29):16578–16585, 2019.
- [87] Zeynep Mutlu, Siamak Shams Es-haghi, and Mukerrem Cakmak. Recent trends in advanced contact lenses. *Advanced healthcare materials*, page 1801390, 2019.
- [88] P Paradiso, R Galante, L Santos, AP Alves de Matos, R Colaço, AP Serro, and B Saramago. Comparison of two hydrogel formulations for drug release in ophthalmic lenses. *Journal of biomedical materials research part B: Applied biomaterials*, 102(6):1170–1180, 2014.
- [89] Philip L Ritger and Nikolaos A Peppas. A simple equation for description of solute release i. fickian and non-fickian release from non-swellable devices in the form of slabs, spheres, cylinders or discs. *Journal of controlled release*, 5(1):23–36, 1987.
- [90] Juergen Siepmann and Nicholas A Peppas. Higuchi equation: derivation, applications, use and misuse. *International journal of pharmaceutics*, 418(1):6–12, 2011.
- [91] AR Berens and HB Hopfenberg. Diffusion and relaxation in glassy polymer powders: 2. separation of diffusion and relaxation parameters. *Polymer*, 19(5):489–496, 1978.

- [92] DJ Enscoe, HB Hopfenberg, and VT Stannett. Effect of particle size on the mechanism controlling n-hexane sorption in glassy polystyrene microspheres. *Polymer*, 18(8):793–800, 1977.
- [93] Gavin W Sinclair and Nikolaos A Peppas. Analysis of non-fickian transport in polymers using simplified exponential expressions. *Journal of Membrane Science*, 17(3):329–331, 1984.
- [94] Richard W Korsmeyer and Nikolaos A Peppas. Effect of the morphology of hydrophilic polymeric matrices on the diffusion and release of water soluble drugs. *Journal of Membrane Science*, 9(3):211–227, 1981.
- [95] Nikolaos A Peppas and Jennifer J Sahlin. A simple equation for the description of solute release. iii. coupling of diffusion and relaxation. *International journal of pharmaceutics*, 57(2):169–172, 1989.
- [96] Madeline Torres-Lugo and Nikolaos A Peppas. Molecular design and in vitro studies of novel ph-sensitive hydrogels for the oral delivery of calcitonin. *Macromolecules*, 32(20):6646–6651, 1999.
- [97] Sumod Kalakkunnath, Douglass S. Kalika, Haiqing Lin, Roy D. Raharjo, and Benny D. Freeman. Molecular relaxation in cross-linked poly(ethylene glycol) and poly(propylene glycol) diacrylate networks by dielectric spectroscopy. *Polymer*, 48(2):579–589, January 2007.
- [98] Haiqing Lin, Elizabeth Van Wagner, John S. Swinnea, Benny D. Freeman, Steven J. Pas, Anita J. Hill, Sumod Kalakkunnath, and Douglass S. Kalika. Transport and structural characteristics of crosslinked poly(ethylene oxide) rubbers. *Journal of Membrane Science*, 276(1):145–161, May 2006.
- [99] Gavin Burke, Zhi Cao, Declan M. Devine, and Ian Major. Preparation of Biodegradable Polyethylene Glycol Dimethacrylate Hydrogels via Thiol-ene Chemistry. *Polymers*, 11(8):1339, August 2019.
- [100] Valerie Barron, John A. Killion, Laura Pilkington, Gavin Burke, Luke M. Geever, John G. Lyons, Edwin McCullagh, and Clement L. Higginbotham. Development of chemically cross-linked hydrophilic–hydrophobic hydrogels for

-
- drug delivery applications. *European Polymer Journal*, 75:25–35, February 2016.
- [101] Paula Yurkanis Bruice. *Organische Chemie: Studieren kompakt*. Pearson Deutschland GmbH, 2011.
- [102] Ji Won Hwang, Seung Man Noh, Bumsang Kim, and Hyun Wook Jung. Gelation and crosslinking characteristics of photopolymerized poly (ethylene glycol) hydrogels. *Journal of Applied Polymer Science*, 132(22), 2015.
- [103] G Mabillean, IC Stancu, T Honore, G Legeay, C Cincu, MF Basle, and D Chappard. Effects of the length of crosslink chain on poly (2-hydroxyethyl methacrylate)(phema) swelling and biomechanical properties. *Journal of Biomedical Materials Research Part A*, 77(1):35–42, 2006.
- [104] Pauli Virtanen, Ralf Gommers, Travis E. Oliphant, Matt Haberland, Tyler Reddy, David Cournapeau, Evgeni Burovski, Pearu Peterson, Warren Weckesser, and SciPy 1.0 Contributors. SciPy 1.0: Fundamental Algorithms for Scientific Computing in Python. *Nature Methods*, 17:261–272, 2020.
- [105] S. van der Walt, S. C. Colbert, and G. Varoquaux. The numpy array: A structure for efficient numerical computation. *Computing in Science Engineering*, 13(2):22–30, 2011.
- [106] Mi Steinbach, Richard Hirsch, Michael Gartz, and Silke Rathgeber. Polymer network characterization of 3d printable pegdma based polymer resins. *unpublished*.
- [107] Adilet Zhakeyev, Li Zhang, and Jin Xuan. Photoactive resin formulations and composites for optical 3D and 4D printing of functional materials and devices. In *3D and 4D Printing of Polymer Nanocomposite Materials*, pages 387–425. Elsevier, 2020.
- [108] Andréa Arruda Martins Shimojo, Aline Mara Barbosa Pires, Rafael Lichy, Ana Amélia Rodrigues, and Maria Helena Andrade Santana. The crosslinking degree controls the mechanical, rheological, and swelling properties of

- hyaluronic acid microparticles. *Journal of Biomedical Materials Research Part A*, 103(2):730–737, May 2014.
- [109] L.R. Grace and M.C. Altan. Non-fickian three-dimensional hindered moisture absorption in polymeric composites: Model development and validation. *Polymer Composites*, 34(7):1144–1157, June 2013.
- [110] Jiahui Shao and Ruth E. Baltus. Effect of solute concentration on hindered diffusion in porous membranes. *AIChE Journal*, 46(7):1307–1316, July 2000.
- [111] Alvaro Goyanes, Usanee Det-Amornrat, Jie Wang, Abdul W. Basit, and Simon Gaisford. 3D scanning and 3D printing as innovative technologies for fabricating personalized topical drug delivery systems. *Journal of Controlled Release*, 234:41–48, July 2016.
- [112] Jie Wang, Alvaro Goyanes, Simon Gaisford, and Abdul W. Basit. Stereolithographic (SLA) 3D printing of oral modified-release dosage forms. *International Journal of Pharmaceutics*, 503(1-2):207–212, April 2016.
- [113] Liraz Larush, Inon Kaner, Arnon Fluksman, Aviad Tamsut, Amol Ashok Pawar, Polina Lesnovski, Ofra Benny, and Shlomo Magdassi. 3D printing of responsive hydrogels for drug-delivery systems. *Journal of 3D Printing in Medicine*, 1(4):219–229, October 2017.
- [114] Pamela Robles-Martinez, Xiaoyan Xu, Sarah J. Trenfield, Atheer Awad, Alvaro Goyanes, Richard Telford, Abdul W. Basit, and Simon Gaisford. 3D Printing of a Multi-Layered Polypill Containing Six Drugs Using a Novel Stereolithographic Method. *Pharmaceutics*, 11(6):274, June 2019. Number: 6.
- [115] Xiaoyan Xu, Pamela Robles-Martinez, Christine M. Madla, Fanny Joubert, Alvaro Goyanes, Abdul W. Basit, and Simon Gaisford. Stereolithography (SLA) 3D printing of an antihypertensive polyprintlet: Case study of an unexpected photopolymer-drug reaction. *Additive Manufacturing*, 33:101071, may 2020.
- [116] Samuel Clark Ligon, Robert Liska, Jürgen Stampfl, Matthias Gurr, and Rolf Mülhaupt. *Polymers for 3D Printing and Customized Additive Manufacturing*.

-
- Chemical Reviews*, 117(15):10212–10290, August 2017. Publisher: American Chemical Society.
- [117] Levent Aktas, Youssef K. Hamidi, and M. Cengiz Altan. Combined Edge and Anisotropy Effects on Fickian Mass Diffusion in Polymer Composites. *Journal of Engineering Materials and Technology*, 126(4):427–435, November 2004.
- [118] N. R. Richbourg, M. Wancura, A. E. Gilchrist, S. Toubbeh, B. a. C. Harley, E. Cosgriff-Hernandez, and N. A. Peppas. Precise control of synthetic hydrogel network structure via linear, independent synthesis-swelling relationships. *Science Advances*, 7(7):eabe3245, February 2021. Publisher: American Association for the Advancement of Science Section: Research Article.
- [119] Andrea C. Jimenez-Vergara, John Lewis, Mariah S. Hahn, and Dany J. Munoz-Pinto. An improved correlation to predict molecular weight between crosslinks based on equilibrium degree of swelling of hydrogel networks. *Journal of Biomedical Materials Research Part B: Applied Biomaterials*, 106(3):1339–1348, 2018. _eprint: <https://onlinelibrary.wiley.com/doi/pdf/10.1002/jbm.b.33942>.
- [120] Tiziana Canal and Nikolaos A. Peppas. Correlation between mesh size and equilibrium degree of swelling of polymeric networks. *Journal of Biomedical Materials Research*, 23(10):1183–1193, 1989. _eprint: <https://onlinelibrary.wiley.com/doi/pdf/10.1002/jbm.820231007>.
- [121] G. S. Offeddu, E. Axpe, B. A. Harley, and M. L. Oyen. Relationship between permeability and diffusivity in polyethylene glycol hydrogels. *AIP Advances*, 8(10):105006, October 2018. Publisher: American Institute of Physics.
- [122] Sungmin Park, Anna M. Smallwood, and Chang Y. Ryu. Mechanical and Thermal Properties of 3D-Printed Thermosets by Stereolithography. *Journal of Photopolymer Science and Technology*, 32(2):227–232, June 2019.
- [123] Formlabs Inc. What does resolution mean in 3d printing? <https://www.formlabs.com/blog/3d-printer-resolution-meaning/>.

- [124] Gerard Fleer, MA Cohen Stuart, Jan MHM Scheutjens, T Cosgrove, and B Vincent. *Polymers at interfaces*. Springer Science & Business Media, 1993.
- [125] J Baschnagel and F Varnik. Computer simulations of supercooled polymer melts in the bulk and in confined geometry. *Journal of Physics: Condensed Matter*, 17(32):R851, 2005.
- [126] Roland R Netz and David Andelman. Neutral and charged polymers at interfaces. *Physics reports*, 380(1-2):1–95, 2003.
- [127] Mi Steinbach, Richard Hirsch, Michael Gartz, and Silke Rathgeber. Testosterone-embedded 3d printable implants for controlled drug release. *unpublished*.
- [128] Xiaoyan Xu, Alvaro Goyanes, Sarah J. Trenfield, Luis Diaz-Gomez, Carmen Alvarez-Lorenzo, Simon Gaisford, and Abdul W. Basit. Stereolithography (SLA) 3D printing of a bladder device for intravesical drug delivery. *Materials Science and Engineering: C*, 120:111773, January 2021.
- [129] Frederick C.W. Wu, Abdelouahid Tajar, Jennifer M. Beynon, Stephen R. Pye, Alan J. Silman, Joseph D. Finn, Terence W. O'Neill, Gyorgy Bartfai, Felipe F. Casanueva, Gianni Forti, Aleksander Giwercman, Thang S. Han, Krzysztof Kula, Michael E.J. Lean, Neil Pendleton, Margus Punab, Steven Boonen, Dirk Vanderschueren, Fernand Labrie, and Ilpo T. Huhtaniemi. Identification of Late-Onset Hypogonadism in Middle-Aged and Elderly Men. *New England Journal of Medicine*, 363(2):123–135, July 2010. Publisher: Massachusetts Medical Society _eprint: <https://doi.org/10.1056/NEJMoa0911101>.
- [130] Giovanni Corona, Giulia Rastrelli, Abraham Morgentaler, Alessandra Sforza, Edoardo Mannucci, and Mario Maggi. Meta-analysis of Results of Testosterone Therapy on Sexual Function Based on International Index of Erectile Function Scores. *European Urology*, 72(6):1000–1011, December 2017.
- [131] Abraham Morgentaler, Michael Zitzmann, Abdulmaged M. Traish, Anthony W. Fox, T. Hugh Jones, Mario Maggi, Stefan Arver, Antonio Aversa, Juliana C. N. Chan, Adrian S. Dobs, Geoffrey I. Hackett, Wayne J. Hellstrom,

-
- Peter Lim, Bruno Lunenfeld, George Mskhalaya, Claude C. Schulman, and Luiz O. Torres. Fundamental Concepts Regarding Testosterone Deficiency and Treatment: International Expert Consensus Resolutions. *Mayo Clinic Proceedings*, 91(7):881–896, July 2016.
- [132] Shalender Bhasin, Juan P Brito, Glenn R Cunningham, Frances J Hayes, Howard N Hodis, Alvin M Matsumoto, Peter J Snyder, Ronald S Swerdloff, Frederick C Wu, and Maria A Yialamas. Testosterone Therapy in Men With Hypogonadism: An Endocrine Society* Clinical Practice Guideline. *The Journal of Clinical Endocrinology & Metabolism*, 103(5):1715–1744, May 2018.
- [133] Deutsche Gesetzliche Unfallversicherung e.V. (DGUV) GESTIS-Stoffdatenbank. methylene blue (cas registry number 61-73-4). <https://gestis.dguv.de/>. Accessed: 2022-01-12.
- [134] National Center for Biotechnology Information (2022). Pubchem compound summary for cid 6099, methylene blue. Retrieved May 4, 2022 from <https://pubchem.ncbi.nlm.nih.gov/compound/Methylene-blue>.
- [135] American Chemical Society (2022) scifinder. methylene blue (cas registry number 61-73-4). <https://scifinder-n.cas.org/>. Accessed: 2022-01-12.
- [136] National Center for Biotechnology Information (2022). Pubchem compound summary for cid 6013, testosterone. Retrieved May 4, 2022 from <https://pubchem.ncbi.nlm.nih.gov/compound/Testosterone>.
- [137] Paul J. Flory and John Rehner. Statistical Mechanics of Cross-Linked Polymer Networks II. Swelling. *The Journal of Chemical Physics*, 11(11):521–526, November 1943. Publisher: American Institute of Physics.
- [138] Richard W. Kormeyer and Nikolaos A. Peppas. Effect of the morphology of hydrophilic polymeric matrices on the diffusion and release of water soluble drugs. *Journal of Membrane Science*, 9(3):211–227, January 1981.
- [139] Peter Ertl, Bernhard Rohde, and Paul Selzer. Fast calculation of molecular polar surface area as a sum of fragment-based contributions and its application

to the prediction of drug transport properties. *Journal of medicinal chemistry*, 43(20):3714–3717, 2000.

- [140] Elias M. Zirdehi, Thomas Voigtmann, and Fathollah Varnik. Multiple character of non-monotonic size-dependence for relaxation dynamics in polymer-particle and binary mixtures. *Journal of Physics: Condensed Matter*, 32(27):275104, April 2020. Publisher: IOP Publishing.
- [141] NISO CRediT Working Group et al. Ansi/niso z39. 104-2022, credit, contributor roles taxonomy. *Baltimore, MD: National Information Standards Organization*, 2022.

List of Figures

1.1	Schematic illustration of API embedded into a polymer matrix and its diffusion from the polymeric compound when placed into a blood-like buffered pH solution.	3
1.2	Overview of the 3D printable photopolymer resin development.	6
1.3	Overview of the main steps in the polymer network characterization.	8
1.4	Overview of the formulation and characterization of a testosterone containing polymer resin.	10
2.1	Schematic drawing of a hole i) in growth direction; ii) perpendicular to growth direction to illustrate the staircase effect. The effect is explained more in detail in [50]. Figure reproduced from [41].	22
2.2	Overview of the main features of the Multi Laser Volume Stereolithography process.	24
2.3	Schematic illustration of the MLVS prototype.	25
2.4	Schematic illustration of two laser beams focused into a photopolymer reservoir to one target point; Figure reproduced from [41].	26
2.5	Spectral absorbance of Formlabs CLEAR resin diluted with Tetrahydrofuran. Measured with a Spectrostar Nano (sensitivity: OD range 0 to 4 OD); Figure reproduced from [41].	27

2.6	The graphs show the spectral measurements at exposure time intervals from 1 to 10 seconds. Uncured resin was used as reference; Figure modified from [41].	28
2.7	Graph showing exemplarily the deviation of the transmission at 425 nm to the reference value for the exposure intervals from 1 to 10 seconds; Figure reproduced from [41].	29
4.1	Simulation of the API release from the sample into the water over time without stirring. From top to bottom, the release profile is shown on the x, y, and z-axis over 500 iterations. The dashed line represents the interface between polymer (right side) and water (left side).	46
4.2	Simulation of the API release from the sample into the water over time while constant stirring. From top to bottom, the release profile is shown on the x, y, and z-axis over 500 iterations. The dashed line represents the interface between polymer (right side) and water (left side).	46
4.3	Simulation of the API release from an inhomogeneous sample into the water over time under constant stirring. The initial concentration varies between 90 % and 100 %. From top to bottom, the release profile is shown on the x, y, and z-axis over 100 iterations. The dashed line represents the interface between polymer and water.	48
4.4	Graph depicting the original measurement of a diffusion measurement of sample S_{194} , and the corresponding interpolated error bars shown in gray. The modeled data curve (small black dot) was fitted with Equations 3.23 and 3.24. The fitting parameter is a non-concentration-dependent diffusion coefficient.	49
4.5	Graph depicting the original measurement of a diffusion measurement of sample S_{194} , and the corresponding interpolated error bars shown in gray. The modeled data curve (small black dot) was fitted with Equations 3.23 and 3.24. The fitting parameter is a concentration-dependent diffusion coefficient.	50

4.6	Graph depicting the original measurement of a diffusion measurement of sample S_{194} , and the corresponding interpolated error bars shown in gray. The simulated data curve (small black dot) was fitted with Equation 3.30.	51
4.7	Graph depicting the original measurement of a diffusion measurement of sample S_{194} , and the corresponding interpolated error bars shown in gray. The simulated data curve (small black dot) was fitted with Equation 3.33.	52
5.1	a) PEGDMA, b) pHEMA, c) MB hydrate, and d) Diphenyl (2,4,6-trimethylbenzoyl) phosphine oxide (TPO)	58
5.2	Microscopic pictures of a $L_{1.51}$ sample before (left side) and after (right side) release experiments with a magnification of factor 10.	64
5.3	FT-IR spectra of PEGDMA in liquid condition (gray line) and PEGDMA photopolymerized with 1 wt% TPO (black line).	65
5.4	Comparison of the percentage of MB released from samples shown in Figure 5.5 at different time points (left side 1 h, right side 8 h). S-samples are indicated in black, L-samples in grey.	66
5.5	Release of methylene blue from S-samples and L-samples during 0 h to 8 h and 23 h to 32 h in percentage. The standard deviation is indicated by error bars at measurement position.	70
5.6	Comparison of $\frac{\Delta M_r}{\Delta M_\infty}$ values resulting from Equation 5.6 and measured values showing a proper modeling of release profiles. Calculated variables and R^2 values are listed in Table 5.2	71
6.1	Complex viscosity measurements of resin S0 during UV irradiation with intensities between $0.1 \mu\text{W}/\text{mm}^2$ to $44.6 \mu\text{W}/\text{mm}^2$ (complex viscosities are normalized except of intensity $0.1 \mu\text{W}/\text{mm}^2$); solidification start time indicated by triangles on the horizontal axis. [106]	78
6.2	left side: schematic illustration of a) moulded and b) 3D printed polymer samples and right side: concentration C of water over distance x between the surface and the center of the sample ($h/2$) at a fix time point during mass uptake assuming a continuous water flux. [106]	81

6.3	Solidification start energy per area solidification start energy (SSE) (top) and corresponding solidification start time solidification start time (SST) (bottom) over intensity calculated from complex viscosity measurements during ultraviolet (UV) polymerization. [106]	86
6.4	Mass uptake ΔM_r of molded (top) and printed (bottom) polymer resins over a soak time of $1.1 \cdot 10^{-4}$ s (top) or $2.5 \cdot 10^{-4}$ s (bottom) in pH buffer. [106]	91
6.5	Diffusion coefficients determined by fitting mass uptake curves of 3D printed and molded resins $S_0, S_{15}, S_{194}, L_0, L_{15}, L_{194}$. [106]	93
6.6	Box plot of polymer mesh sizes of 3D printed and molded resins calculated in equilibrium swollen state. [106]	95
7.1	Chemical structures of a) the methylene blue molecule and b) the testosterone molecule. [127]	101
7.2	Mass uptake ΔM_r^{mass} of testosterone (TE) and methylene blue (MB) resins over a soak time of 3 h in pH 7.4 buffer at 37 °C; curves are fitted by the use of Equation 7.3. [127]	108
7.3	Testosterone (TE) and methylene blue (MB) release from polymer samples; curves are fitted by the use of Equation 7.5. [127]	110
7.4	Drug release measurements multiplied by the surface area of testosterone (TE) and methylene blue (MB), respectively. [127]	111

List of Acronyms

3DP 3D printing

API active pharmaceutical ingredient

CAD computer-aided design

FTIR fourier-transform infrared

HPLC high-performance liquid chromatography

LSLA laser stereolithography

MB methylene blue

MLVS Multi Laser Volume Stereolithography

PEGDMA Poly(ethylene glycol) dimethacrylate

pHEMA Poly(2-hydroxyethyl methacrylate)

PEG Poly(ethylene glycol)

PI photoinitiator

SD solidification duration

SE solidification energy

SLA stereolithography

SSE solidification start energy

SST solidification start time

TE testosterone

TPO Diphenyl (2,4,6- trimethylbenzoyl) phosphine oxide

UV ultraviolet

HPLC high-performance liquid chromatography

PSA polar surface area

TGA thermogravimetric analysis

Declaration

I certify that I have written this dissertation - including any attached drawings, sketch maps and illustrations - independently and have not used any sources or aids other than those indicated. All passages in the thesis that are taken from other works, either in wording or in meaning, have been clearly indicated as borrowed from other sources.

The authors' contributions¹ to the unpublished articles cited in [127] and [106] are as follows:

Mi Steinbach Conceptualization, Data curation, Formal analysis, Investigation, Methodology, Software, Validation, Visualization, Writing – original draft;

Richard Hirsch Funding acquisition, Resources, Writing – review & editing;

Michael Gartz Funding acquisition, Resources, Writing – review & editing;

Silke Rathgeber Writing – review & editing

¹In accordance with the CRediT Taxonomy [141]